TOPICAL REVIEW

Thermal confinement and transport in spherical tokamaks: a review

To cite this article: S M Kaye *et al* 2021 *Plasma Phys. Control. Fusion* **63** 123001

View the article online for updates and enhancements.

IOP ebooks™

Bringing together innovative digital publishing with leading authors from the global scientific community.

Start exploring the collection−download the first chapter of every title for free.

Topical Review

Thermal confinement and transport in spherical tokamaks: a review

S M Kaye[1,*] , J W Connor[2,3] and C M Roach[2]

[1] Princeton Plasma Physics Laboratory, Princeton University, Princeton, NJ 08543,
United States of America
[2] CCFE, Culham Science Centre, Abingdon, Oxfordshire OX 14 3DB, United Kingdom
[3] Department of Physics, Imperial College of Science, Technology and Medicine, London SW7 2BZ,
United Kingdom

E-mail: kaye@pppl.gov

CrossMark

Abstract

In this paper, we review the thermal plasma confinement and transport properties observed and predicted in low aspect ratio tokamaks, or spherical tokamaks (STs), which can depart significantly from those observed at higher aspect ratio. In particular, thermal energy confinement scalings show a strong, near linear dependence of energy confinement time on toroidal magnetic field, while the dependence on plasma current is more modest, the opposite of what is seen at higher aspect ratio. STs have revealed a very strong improvement in normalized confinement with decreasing collisionality, much stronger than at higher aspect ratio, which bodes well for an ST-based fusion pilot plant should this trend continue at an even lower collisionality than has already been accessed. These differences arise because of fundamental differences in transport in STs due to the more extreme toroidicity (i.e. reduced region of bad curvature), and to the relatively larger $E_r \times B$ shearing rates, both of which can suppress electrostatic drift wave instabilities at both ion and electron gyroradius scales. In addition, electromagnetic effects are much stronger in STs because they operate at high β_T. Gyrokinetic (GK) studies, coupled with low- and high-k turbulence measurements, have shed light on the underlying physics controlling transport. At lower β_T, both ion- and electron-scale electrostatic drift turbulence may be responsible for transport. At higher β_T, microtearing, kinetic ballooning, and hybrid trapped electron/kinetic ballooning modes increasingly play a role, and they have a much stronger impact in the core of ST plasmas than at higher aspect ratio. Flow shear affects the balance between ion- and electron-scale modes. Non-linear GK simulations find regimes where the electron heat flux decreases with decreasing collisionality, consistent with the experimental global normalized confinement scaling. The ST is unique in that the relatively low toroidal magnetic field allows for localized measurements of electron-scale turbulence, and this coupled with turbulence measurements at ion-scales has facilitated detailed comparisons with GK simulations. These data have provided compelling evidence for the presence of ion temperature gradient and electron temperature gradient turbulence in some plasmas, and direct experimental support for the impact of experimental actuators like rotation shear, density gradient and magnetic shear on turbulence and transport.

* Author to whom any correspondence should be addressed.

1. Introduction

A spherical torus or tokamak (ST) is a tokamak with an aspect ratio ($A = R/a$) less than approximately two [1, 2]. Here, R and a are the major and minor radii of the plasma. The ST provides a potentially transformative route to a more compact and possibly lower cost component test facility [3]/fusion nuclear science facility [4–6] or fusion pilot plant (FPP) [7–15] because of its compactness and because of its fundamental properties of enhanced confinement and stability at low aspect ratio, which have been established quantitatively in the first generation of high-powered STs: the National Spherical Torus Experiment (NSTX) [16, 17] and the Mega Amp Spherical Tokamak (MAST) [18]. The ST configuration also has other physics advantages, as can be seen from results of early studies as well as from 0D considerations. For instance, work has predicted that STs can operate in regimes of high β_T (β_T=plasma pressure/toroidal magnetic field pressure), as was demonstrated in the Small Tight Aspect Ratio Tokamak (START) [19] and NSTX [20], an economic metric that maximizes the plasma energy with respect to the energy in the toroidal field that has to be provided by external power. The ST is an inherently high plasma current machine due to its low aspect ratio geometry and strong natural shaping (e.g. elongation κ) [21], with the plasma current, I_P, given by [1]

$$I_p \simeq \frac{(1+\kappa^2)}{2} \frac{RB_T}{q_a} \frac{Af(A)}{A^2-1}, \text{ where } f(A) = 1.22A - 0.68. \quad (1)$$

Here, B_T is toroidal magnetic field at the major radius R, and q_a is edge safety factor. The high current allows access to high β_T, as given crudely by the magnetohydrodynamic (MHD) stability criterion $\beta_T = \beta_N I_p/(aB_T)$ where β_N is a constant, and which is approximately 4 at conventional aspect ratio, but can be up to 8 at low aspect ratio [20, 22]. A high self-driven bootstrap current [23, 24] is also deemed necessary for advanced tokamak Pilot Plants. The bootstrap fraction is given by $f_{bs} \sim (1+\kappa^2)\frac{\beta_N}{l_i}$ for fixed aspect ratio and I_p/aB_T, where l_i is the plasma self-inductance. Thus, the ability to optimize β_N and κ is critical. The ST configuration affords a large accessible range in these parameters and thus flexibility in this optimization and the ability to achieve stable operation at high κ (up to 2.9) and high-β_N/l_i (in excess of 14) was shown in NSTX [25, 26].

These characteristics help maximize the $nT\tau_E$ metric (n is plasma density, T is plasma temperature, and τ_E is energy confinement time), which, when the Greenwald density scaling $n_{GW} \propto \frac{I_p}{a^2}$ [27] is considered along with the definition of $q \propto \frac{a^2 B_T \kappa}{RI_p}$, can be rewritten as [15]

$$nT\tau_E \propto \frac{H^2}{q^3} R^2 B_T^3 \left(\frac{\kappa^{\frac{7}{2}}}{A^3} \right) \quad (2)$$

where H is the confinement enhancement factor defined as $\tau_E/\tau_{E,98y,2}$, with $\tau_{E,98y,2}$ being the parametric scaling of energy confinement time based on a multi-machine database [28]. In addition, operation at low aspect ratio and high elongation can help maximize the ratio of fusion power to the resistive dissipation in the toroidal magnetic field (TF) center leg, which can be expressed as [16]

$$\frac{P_{fusion}}{P_{TF}} \propto \beta_N^2 (1+\kappa^2)^2 \left(\frac{RB_{max}}{q_a} \right)^2 \frac{f(A)^2}{(A+1)^4 A^2}. \quad (3)$$

Here, B_{max} is the maximum magnetic field strength, which usually occurs at the outer region of the inner leg of the TF coil.

Recent studies [12, 13] have, in fact, demonstrated the possibility of designing small, compact steady-state ST FPPs. These studies use system codes that recognize standard operating limits (e.g. the Greenwald density limit [27], the Sykes–Troyon β limit [29, 30] with and without additional wall stabilization), current drive efficiencies, basic engineering constraints, and the utilization of high temperature superconducting magnets. They calculate the fusion power output, or the fusion gain factor, Q (ratio of fusion power to input power) as a function of size, TF winding pack density, and other variables. Critical to all these pilot plant studies, as can be seen by the above relations, at both small and higher aspect ratio, is the scaling of energy confinement time, τ_E, particularly with respect to dimensionless parameters such as collisionality ν_* and β_T. The conventional scaling, $\tau_{E,98y,2}$ effectively scales almost inversely with β_T, and it has no dependence on ν_*. STs are at the extreme limits of the multi-machine database as regards aspect ratio, and beyond the limits as regards β_T. There is evidence, which will be discussed in this paper, that ST energy confinement has a weak dependence on β_T but a strong inverse dependence on ν_*, both of which would be favorable for a small, compact ST power plant. The case for this path to fusion power would be strengthened if the empirical scalings could be augmented by first principles calculations of turbulent transport, as has been initiated in early studies [31, 32] particularly as this would allow confident extrapolation to parameter values typical of an ST power plant.

The ST configuration also presents physics challenges in several areas. STs with neutral beam auxiliary heating can operate in a regime where the ratio of fast particle velocity to Alfvén velocity exceeds one, and this could lead to destabilization of multiple Alfvén Eigenmodes, which can couple to one another and impact severely the heating and current drive efficiency of the fast ions [33]. Furthermore, the compact nature of the ST can lead to high divertor and wall power and particle fluxes, and the enhanced flux expansion properties of divertor configurations such as the X, Super-X [34, 35], and snowflake

Table 1. Comparison of key operating parameters for STs that have performed, or will be performing, confinement studies. Heating power is through neutral beams, unless otherwise indicated. Values in parenthesis represent potential upgrades. The various heating mechanisms, also given in parentheses, include neutral beam (NB), radio-frequency (RF), and HHFW.

	Pegasus	START	Globus-M	Globus-M2	ST40	MAST	NSTX	MAST-U	NSTX-U
Aspect ratio	1.2	1.3	1.5	1.5	1.7	1.3	1.5	1.56	1.7
Major radius R (m)	0.35	0.3	0.34	0.36	0.40	0.85	0.89	0.82	0.94
Minor radius a (m)	0.29	0.23	0.23	0.24	0.24	0.65	0.61	0.53	0.55
Plasma elongation κ	2.6	1.8	2.0	2.0	2.5	2.1	2.5	2.5	2.75
Plasma triangularity δ	0.50	0.50	0.50	0.30	0.35	0.50	0.70	0.50	0.50
Plasma current (MA)	0.15	0.30	0.25	0.5	2.00	1.2	1.5	2.00	2.00
Toroidal field at R(T)	0.17	0.23	0.5	1.0	3.00	0.52	0.55	0.78	1.00
Max. pulse length (s)	0.05	0.05	0.2	0.7	2.0	0.7	1.85	5.0	5.0
Auxiliary heating power (MW)	0.0	0.8	1.0	2.0 (NB), 1.0 (RF)	2.0	3.0	6.0 (NB), 6.0 (HHFW)	5.0 (7.5)	12.0 (NB) 6.0 (HHFW)

[36] have been, and will be further tested as a means to ameliorate divertor heat loads.

It is important to note that additional (i.e. non-confinement and transport related) ST-relevant physics has been carried out in other STs around the world. The helicity injection tokamak (HIT) [37] in the USA employed co-axial helicity injection to initiate the plasma non-inductively. HIT-II [38] has also studied non-inductive startup along with Pegasus (USA) [39], as well as QUEST [40], TS3/4 [41], UTST [42] and HIST [43] (the latter four in Japan), VEST [44] (Korea) and SUNIST [45] (China). TST-2 [46] and LATE [47] (both in Japan) will investigate high harmonic fast wave (HHFW) and electron cyclotron heating (ECH) heating respectively. CDX-U/LTX/LTX-beta [48, 49] (USA), is investigating liquid lithium (Li) as a plasma facing component. An excellent review of the international ST program progress and ST research results can be found in the review article by Ono and Kaita [50] . The purpose of this paper is to review the thermal plasma confinement and transport physics, crucial to the development of an ST pilot plant, that has been studied in STs over the past three decades or more. We note the importance of the study of Energetic Particle transport in STs, especially in the super-Alfvénic ST regime, as well as pedestal transport. Detailed discussions of these areas are beyond the scope of this review, and they warrant reviews in their own right. While there are a multitude of STs internationally, the review will focus on results from START [51] (UK), NSTX [16, 17] (USA), MAST [18] (UK), Pegasus [52, 53] (USA) and Globus-M [54] and -M2 [55] (Russia). A comparison of the basic operating parameters of these STs is given in table 1. Also included in this table are the operating parameters of newer ST experiments that follow on to those whose results are discussed: ST40 (a high-field ST built and operated by the private company Tokamak Energy Ltd (UK)), MAST-Upgrade or MAST-U (CCFE, UK) and NSTX-Upgrade or NSTX-U (PPPL, USA). These will be discussed more in the concluding section of this review.

This review of the confinement and transport properties of thermal plasmas in STs will be organized as follows. In section 2, we will review L-H threshold experiments, in section 3, we will review dimensional and dimensionless global scaling studies, in sections 4–6 we will review momentum confinement, particle confinement and Internal Transport Barrier (ITB) results respectively. In section 7, we will summarize what gyrokinetic (GK) analysis of experiments has revealed about the plasma turbulence underlying anomalous transport in STs, and we discuss the present state of reduced model development and testing in a short section 8. We will then summarize and discuss future work in section 9.

2. L-H threshold studies

H-mode operation in STs was found to be similar to that at conventional aspect ratio, often leading to improved confinement, and with the main L- to H-mode transition signatures of a sudden drop in the D_α signal, an accelerated rise in plasma density, development of edge pedestals in the temperature and/or density profiles, and often decreases of edge turbulence and increase in edge rotation after the transition. H-mode operation in STs was initially identified in START, specifically in Double Null Divertor discharges [56]. Improvements in particle confinement were inferred from the rise of plasma density and the development of density pedestals [57], and L-H transitions were often observed in Ohmic discharges. L-H threshold powers exceeded published scaling-derived values [58] by up to a factor of 30. It was suggested that the high edge neutral density in START, and the associated high convective heat loss, could impede the L-H transition.

H-modes were obtained successfully during the first years of operation on NSTX [59–61] and MAST [62–64] (figure 1). More recently, H-modes were also obtained on Pegasus [65, 66], and during the first operational periods of NSTX-U [67, 68] and MAST-U [69]. In both MAST and NSTX, transitions into ELMy H-modes were clear and reproducible, even in Ohmic plasmas, and the transitions were facilitated and most reproducible using center stack gas fueling [70, 71]. Inboard fueling led to increased toroidal flow velocities in the outboard midplane in MAST and in the core in Pegasus, possibly leading to a suppression of turbulence. Inferred from this increased toroidal flow velocity was an increase in the magnitude of the negative radial electric field [72]. In NSTX, the measured edge carbon rotation was largest with high field side (HFS) fueling just prior to the transition, and subsequently reversed direction [70].
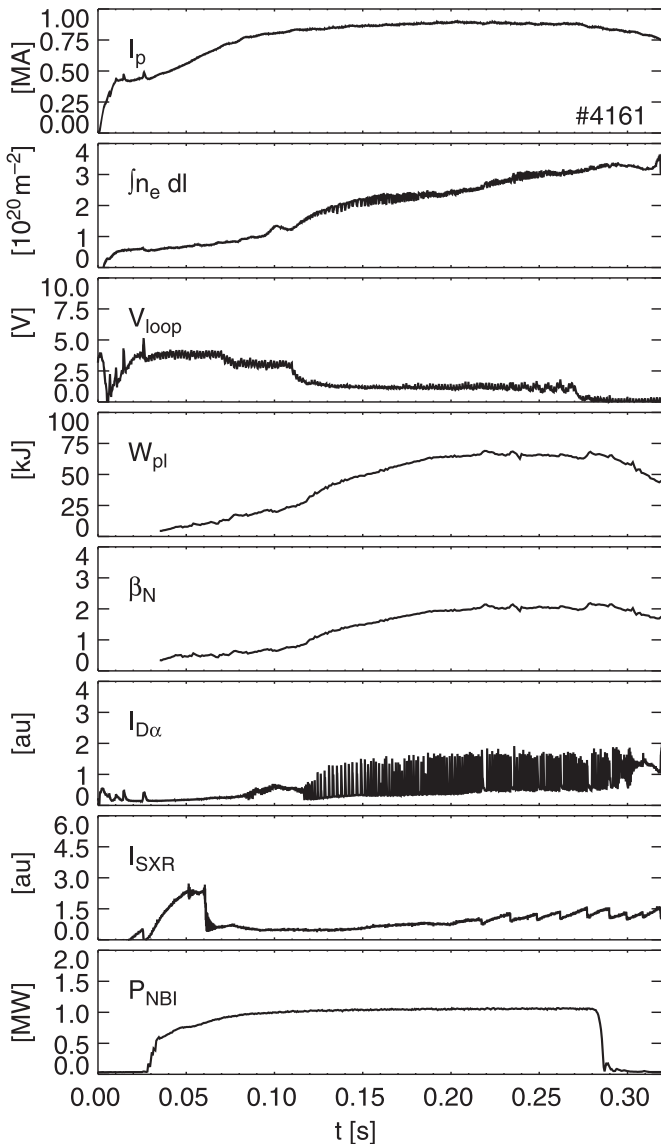
Figure 1. Temporal evolution of (from top panel down) plasma current, line-integral density, loop voltage, plasma energy, normalized β_N, D_α, central SXR emission and NBI beam power for a ELMY H-mode discharge from MAST. Reproduced from [64]. © IOP Publishing Ltd. All rights reserved.

The threshold power was found further to be minimized through careful configuration control; well-balanced double null plasmas in MAST and NSTX led to lower threshold powers than for unbalanced or single-null configurations [73, 74]. Since there were no significant changes in recycling or core impurity levels with these configuration changes, it was posited that the threshold power was influenced strongly by the parallel connection length, which also changed strongly with configuration [73]. On Pegasus, H-modes were obtained either in a limiter or a single null divertor plasmas, with the threshold being comparable in the limited and diverted configurations [66]. The threshold power scaling in Pegasus was found to be consistent with the q-dependence as predicted by the FM3 model [75]. Calculations by one of the authors

(S Kaye) showed L-H transitions on NSTX did not agree with the predictions of the FM3 model.

Later work on MAST and NSTX tested the impact of other operational aspects to see their effect on the L-H threshold power. On MAST, a shorter outer divertor leg led to lower threshold powers [76, 77], reflecting the possible impact of the proximity of the X-point to divertor plates and thus the effect of recycling neutrals. Application of resonant magnetic perturbations (RMPs) for $n = 2, 3, 4$ and 6 on MAST resulted in delayed transitions at low applied fields, with no transition at high applied fields [78]. The delayed transition was believed to be due to longer parallel connection lengths associated with the RMP application, which evolved in time to shorter connection lengths as q_{95} decreased during the discharge. Furthermore, the threshold power increased with increasing RMP magnitude, leading to power thresholds between 20% and 60% greater with RMP application than without. In NSTX, applied $n = 3$ magnetic perturbations led to almost a doubling of the normalized L-H power threshold (P_{LH}/n_e) [74, 79]. In the study, the discharges that transitioned into the H-mode at the lower applied magnetic fields also exhibited higher toroidal velocity shear toward the edge of the plasma.

The same NSTX L-H study presented in the above [79] also assessed several other factors that could influence the L-H transition. The particle fueling-less HHFW heating capability on NSTX allowed for studies of the dependence of P_{LH} on plasma species, an important concern for ITER, and it showed that the threshold power normalized to plasma density was 20% to 40% greater in helium than in deuterium. Furthermore, there was evidence of a strong hysteresis, with the H-L threshold approximately 30% to 40% lower than the L-H threshold, indicating that once in the H-mode, the NSTX discharges could remain in this state with $P_{heat} < P_{LH}$.

A unique observation on NSTX was the dependence of the threshold power on plasma current [79, 80], which has not been seen at higher aspect ratio. On NSTX, the dependence was strong (see figure 2), with threshold powers nearly doubling going from 0.7 to 1.0 *MA*. As will be shown below, this result is qualitatively consistent with the result that the P_{LH} at low aspect ratio depends on the total magnetic field at the edge, B_{TOT}, not just on the toroidal field [81]; at low aspect ratio, $B_T \sim B_P$, where B_P is the poloidal magnetic field, while at higher aspect ratio, $B_T \gg B_P$ at the edge. XGC0 [82] calculations showed that the neoclassical radial electric field well, caused by the thermal ion loss cone near the plasma edge, was distinctly deeper and exhibited stronger radial electric field (E_r) shear at low than high current, consistent with the lower threshold. The deeper well reflected the loss of lower energy particles and those with higher $v_\parallel/v$ than for the higher current (here v is the particle total velocity and $v_\parallel$ is the parallel component).

The NSTX results also showed lower thresholds for higher lithium evaporation rates used for wall conditioning, as well as for lower triangularity plasmas where the X-point was at larger major radius (see figure 10 in Kaye *et al* [79]). XGC0 was used again to explore possible neoclassical effects that could lead to lower thresholds at both larger X-point radius and with more lithium conditioning. It was found that maintaining the $E_r \times B$
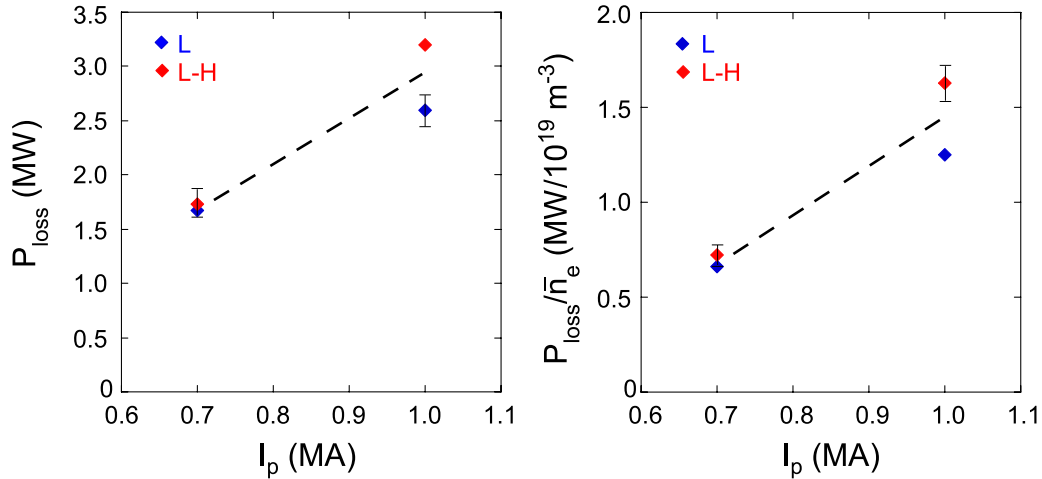
Figure 2. Loss power (left panel) and loss power normalized by line-averaged density (right panel) as a function of plasma current. Here, loss power is the L-H threshold power. Red symbols denote discharges that transition into the H-mode at that loss power, while blue symbols indicate discharges that remained in the L-mode for that loss power. Reproduced courtesy of IAEA. Figure from [79]. Copyright (2011) IAEA.

shear rate resulting from the thermal ion loss cone near the edge requires less heat flux, and thus leads to lower thresholds as the X-point radius increases with a lower divertor recycling to fueling ratio (low recycling with lithium conditioning) [83]. The easier access to H-mode in a low-recycling condition was reported also on Pegasus, which made use of titanium gettering [66].

Edge turbulence suppression was observed on MAST [73], NSTX [84] and Pegasus [66] once the plasma transitioned into the H-mode. In NSTX, no change in turbulence characteristics or shear flow was observed during the period immediately preceding the transition [84, 85]. In particular, NSTX studies [86, 87] indicate that turbulence was not contributing significantly to $E_r \times B$ shear, unlike in some regimes at higher aspect ratio where there is strong evidence of nonlinear energy transfer from turbulence to drive sheared zonal $E_r \times B$ flow directly [88]. This means that for STs, it is the equilibrium $E_r \times B$ shear that is produced by neoclassical and fast ion effects that is associated with the L-H transition. For instance, in NSTX, it was found that bounce precession fishbones, which cause large loss or redistribution of the fast ions reflected by large drops in the neutron rate, led directly to an L-H transition [61]. An incremental 3 kV m^{-1} radial electric field could result from the estimated loss of fast ions, and because of the factor of five to ten lower operating B_T at low relative to high aspect ratio, could lead to high rotational shear values.

Early statistical studies in both NSTX [61] and MAST [89] attempted to relate the transition characteristics to leading theories of the L-H transitions of the time. The theories were based on the drift-resistive ballooning mode [90, 91], peeling modes [92], the drift-Alfvén instability [93] and finite-β drift waves [94]. In the studies for both devices, the data were categorized by whether they were in the L-mode, H-mode, or either dithering or in an L-phase just prior to an L-H transition ('L-H'). In NSTX, the results indicated a clear separation of the L- and H-mode data with respect to the critical

parameters of the first three theories (figure 3). However, there was essentially no difference observed in the cluster of discharges that remained in the L-mode versus the L-mode points that transitioned into the H-mode. This result was found also in MAST [89]. This indicates that while these theories reflected differences between L- and H-mode plasmas, they could not predict the L-H transition.

The fourth theory, the finite-β drift wave theory, predicts a critical pedestal electron temperature for transition into the H-mode, where the critical temperature is related to the point where sheared flows can suppress the turbulence. This theory showed some success in modeling C-Mod and DIII-D [94], but was not successful in modeling the NSTX data; for NSTX, the $T_e/T_{e,crit}$ ranges were the same for the L-mode and the 'L-H' points. On the other hand, this theory showed some success in modeling MAST. Figure 4, shows the cluster of L-H points having slightly higher T_e values in the region of steepest gradient relative to the critical value, $T_{e,crit} = T_{EC}$ than do the L-mode points.

In partial summary of this section, the L-H power threshold studies in STs showed both similarities and differences with those performed at higher aspect ratio. Similar to high aspect ratio, power thresholds in STs were found to be higher with applied 3D magnetic perturbations, and in helium (vs deuterium) plasmas. Power thresholds were found to be lower using HFS vs LFS fueling, with the X-point farther away from the divertor plates, and with lower recycling conditions (including lithium wall conditioning in NSTX). The latter observations reflect the importance of parallel connection lengths and/or minimizing the effect and penetration of recycling neutrals. Among the differences relative to higher aspect ratio are a more significant reduction in the power threshold in connected Double Null than in Single Null plasmas, and no observation of a low density branch of increased power thresholds, although this latter observation has not yet been explored in a dedicated fashion. The observation of a power threshold on I_p is unique to STs, and this has motivated the
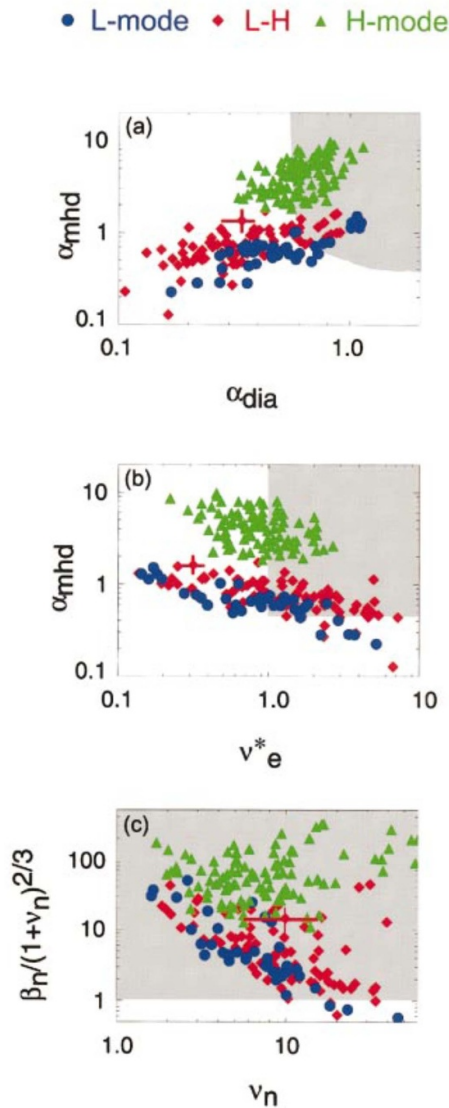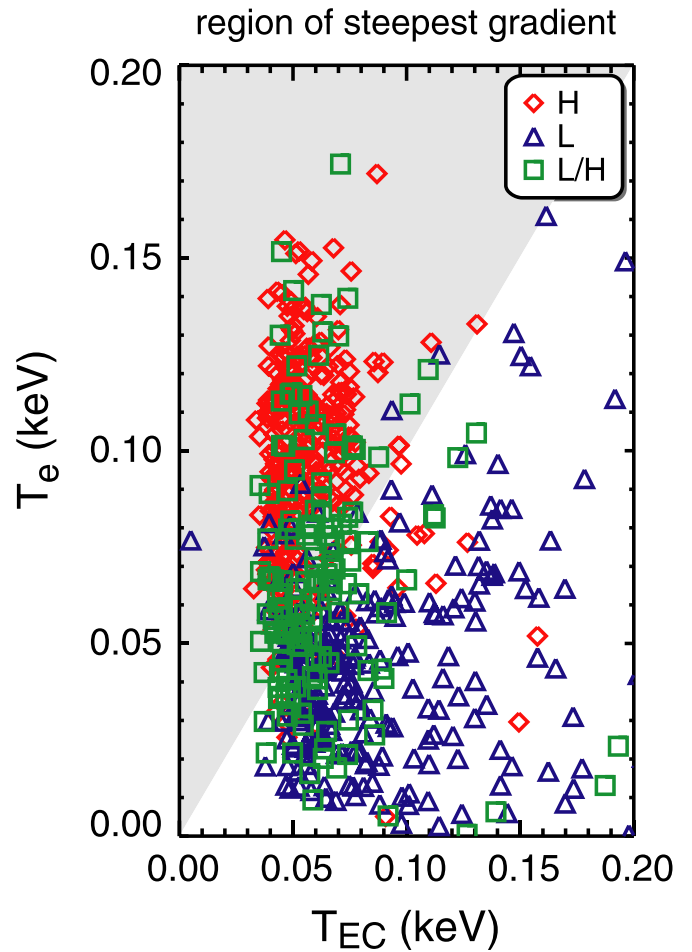
Figure 3. Comparison between experimental data and theory for (a) drift-resistive ballooning modes, (b) peeling modes, and (c) drift Alfvén modes. The shaded region in each plot indicates the theoretical prediction of H-mode access. Reprinted from [61], with the permission of AIP Publishing.

Figure 4. Comparison between experimental data from MAST and the finite-β drive wave theory. The shaded regions indicate where the theory predicts an H-mode. $T_{e,crit}$ is labeled as T_{EC} on the x-axis. Reproduced courtesy of IAEA. Figure from [89]. Copyright (2005) IAEA.

Figure 5. Measured P_{LH} compared to the ITPA scaling for several STs at different aspect ratios. Reprinted figure with permission from [65], Copyright (2016) by the American Physical Society.
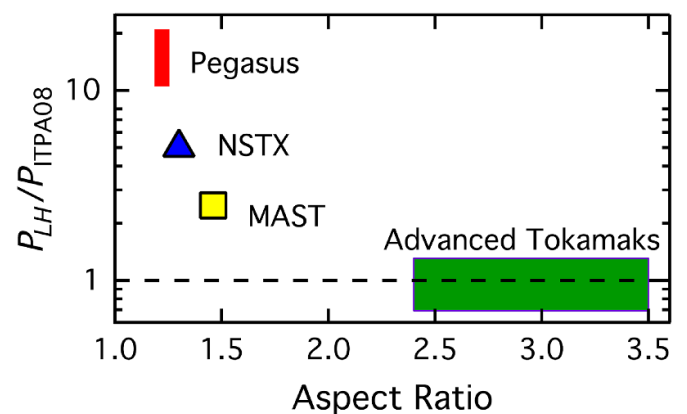
use of B_{TOT} instead of B_T in power threshold scalings, as will be discussed below.

L-H threshold powers in STs typically exceed those predicted by various scalings developed from conventional aspect ratio ($R/a \sim 2.5$ to 4) tokamaks by factors of several up to greater than an order of magnitude. In fact, the ranges of threshold powers for the three STs discussed, normalized to the conventional aspect ratio threshold power scaling predicted by Martin *et al* [95], exhibited a strong dependence on aspect ratio. As the aspect ratio decreases toward one (MAST to NSTX to Pegasus), this ratio increases significantly, as shown in figure 5.

This trend had been recognized implicitly in the re-analysis of the ITPA threshold database, augmented by NSTX and MAST threshold data [81]. It was found in this analysis that including an aspect ratio dependence given by
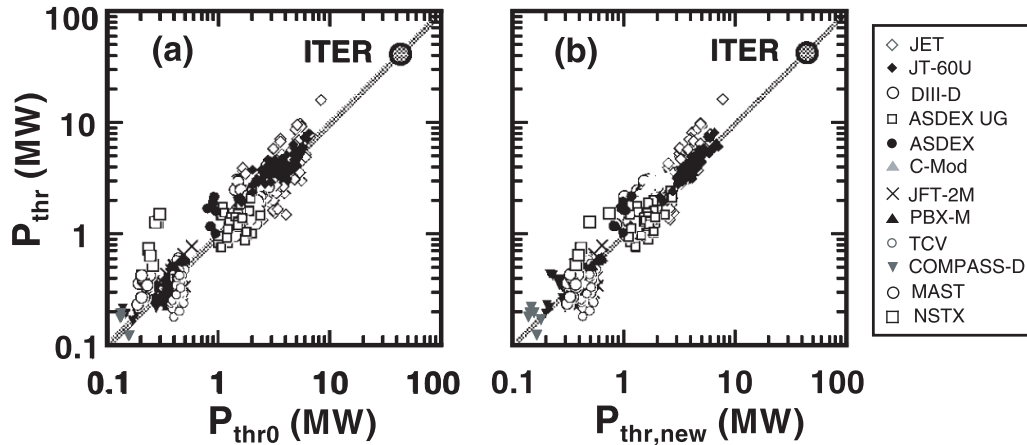
$$F(A) = \left[\frac{A}{1 - \left[\frac{2}{1+A} \right]^{1/2}} \right] \qquad (4)$$

Figure 6. Comparisons of experimental power thresholds ($P_{thr} = P_{LH}$) with scaling expressions from (a) Ryter *et al* [96] for conventional A and (b) Takizuka *et al* [81] accommodating ST data. Reproduced from [81]. © IOP Publishing Ltd. All rights reserved.

allowed the scaling to describe the low A data better than did the conventional aspect ratio scalings. The aspect ratio correction factor is related to the trapped particle fraction, the magnitude of which is related to parallel flow or current, which was hypothesized to impact the transition mechanism. With a higher trapped particle fraction (lower A), the parallel flow/current would be reduced. The work also considered two additional factors: total, instead of just toroidal magnetic field, and effective charge, Z_{eff} ($P_{LH} \propto Z_{eff}^{0.7}$). The use of the total magnetic field attempted to address the current dependence found in the NSTX threshold data, although its parameterization in the scaling, $|B_{TOT}|^{0.7}$, led to a weaker dependence than that observed on NSTX. The full formula is

$$P_{LH} = 0.072 B_{TOT}^{0.7} n_{20}^{0.7} S^{0.9} (Z_{eff}/2)^{0.7} F(A)^{\gamma} \quad (5)$$

where S is plasma surface area and $\gamma = 0.5 \pm 0.5$. P_{LH} for the conventional and ST-modified threshold scalings are compared in figure 6.

3. Global confinement scalings

Systematic and statistical studies have been conducted in STs, as they have in conventional aspect ratio tokamaks, to develop an understanding of the parametric dependencies of both thermal and global energy confinement times on both engineering and physics parameters. Engineering parameters are those that can be controlled externally, e.g. I_p, B_T, R, a, P_{heat}, n, κ, δ (triangularity), while dimensionless physics variables such as ρ_* (normalized Larmor radius), β, ν_* (normalized collisionality), characterize the plasma. The physics parameters, and other dimensionless variables such as R/a, q, κ, δ, are intercorrelated, and thus makes it more difficult to determine unambiguously the parametric variations directly, by using the dimensionless parameters as regression variables, or by transformation from engineering variable scalings. For the latter, due to the intercorrelation of the dimensionless variables, small changes in engineering variable dependencies can lead to large changes in the various

physics parameter dependencies. The best path forward to determine dependencies on physics parameters is through dedicated and controlled experiments, although these have not yet been performed in STs to the extent that they have at conventional aspect ratio.

Confinement studies have been performed primarily in MAST (CCFE, UK), NSTX (PPPL, U.S.), Globus-M (Ioffe Inst., Russia) and most recently Globus-M2, which is an upgrade of Globus-M. The comparison in operating parameters among these STs is given in table 1 (section 1). NSTX and MAST are similar in size and operating parameters, while Globus-M, M2 are smaller. Confinement studies, most notably at higher B_T, I_p and heating power will be conducted over the next several years in MAST-U, NSTX-U and ST40. Operating parameters for these STs are included in table 1 as well.

3.1. Dimensional variable scalings

For simplicity, the scalings are assumed to have the form:

$$\tau_E \propto B_T^{\alpha_B} I_p^{\alpha_I} R^{\alpha_R} n_e^{\alpha_n} P_{heat}^{\alpha_P} \kappa^{\alpha_\kappa} \ldots \quad (6)$$

where the coefficients have been determined historically through multiple linear regression (MLR) [97] or closely related approaches that take into account variable uncertainties [98, 99]. Recently, more advanced machine learning methods have been adopted [100–102]. In this sub-section, we will first discuss results of the parametric trends of confinement time based on engineering variables, followed by a similar discussion revolving around the physics variables in section 3.2. As will be seen, some differences that emerge from engineering scalings even within one device can be reconciled when viewed from the perspective of physics variables.

H-mode operation comprised the majority of confinement-related experiments in STs such as START, MAST, NSTX, Globus-M and Pegasus, and only limited work has been done on assessing Ohmic or L-mode confinement. First physics operation of NSTX found that Ohmic confinement followed the neoAlcator trend, with a nearly linear increase of confinement with line-averaged density, and a saturation of
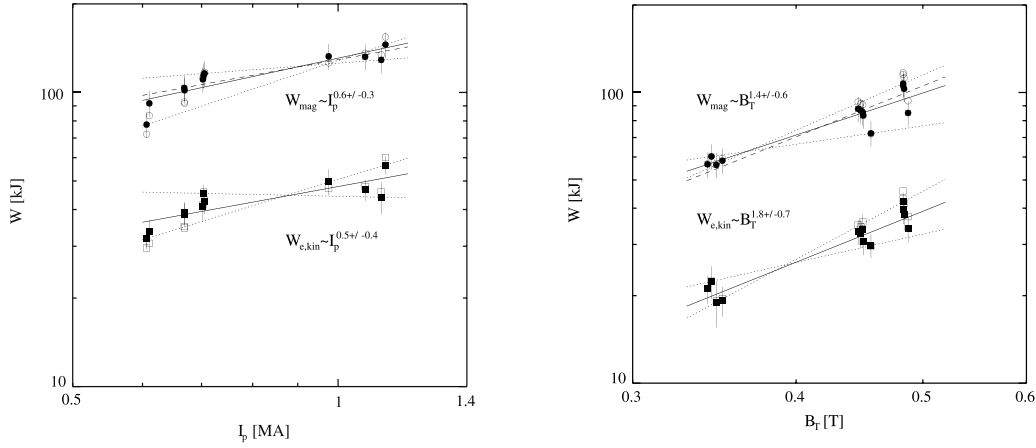
Figure 7. (left) Total and electron stored energy vs I_p and (right) vs B_T for MAST ELMy and ELM-free H-mode plasmas. The various lines show the confidence limits of the linear fits through the data. Reproduced courtesy of IAEA. Figure from [110]. Copyright (2009) IAEA.

the confinement for $\frac{n_e}{n_{GW}} > 0.8$ [103]. Additional Ohmic scaling results were reported on the Globus-M ST , where the energy confinement time τ_E was found to scale as $\tau_e \propto n_e$ for $n_e < 2.5 \times 10^{19}$ m^{-3}, but it was found to be weaker than linear at higher n_e and saturate at Greenwald fractions also of $\frac{n_e}{n_{GW}} \sim 0.8$ [104]. In addition, a linear dependence on I_p but a weak dependence on P_{heat} and $H_{98y,2} \sim 0.5$ to 0.7 was found in Ohmic H-modes. Confinement times in START Ohmic plasmas appeared to be bounded by the neoAlcator scaling predictions [105].

An L-mode study, performed during early neutral beam heating operation in NSTX [106], assessed the parametric dependence of global energy confinement time, which included the fast ion component, as determined from magnetic equilibrium reconstructions, and found that

$$\tau_E = 4.74 \times 10^{-4} B_T^{0.7} I_p^{1.01} n_e^{0.07} P_{loss}^{-0.37} \qquad (7)$$

in sec, T, MA, 10^{19} m^{-3} (line-averaged density), MW (total power lost across the separatrix). While the strong scaling in current is consistent with that seen at conventional aspect ratio, there is also a strong dependence on toroidal field, and a weaker degradation with loss power as compared to conventional aspect ratio.

Early H-mode experiments on STs indicated higher than L-mode energy confinement times. While not explicitly identified as H-modes, discharges on the high-β START ST produced discharges with flat density profiles and large edge density gradients representative of H-modes, and with calculated confinement times that were close to H-mode scaling predictions [107]. In a more dedicated study in START, ELMy discharges were found to exhibit similar trends to, and exceed the 97ELMy scaling [57, 58].

High neutral beam power operation in both MAST and NSTX resulted in routine access to the H-mode regime, and studies on both devices showed the H-mode confinement scaling to be quite different than that at conventional aspect ratio in terms of the dependence on I_p and B_T. Early studies with boronized wall conditioned discharges in NSTX [108]

involved both dedicated single variable scans as well as statistical studies. In these studies, an almost linear dependence of thermal confinement time on plasma current $\tau_E \propto I_p^{0.98}$ was observed at fixed B_T (0.45 T) and heating power (4.4 MW), although the plasma current increase from 0.65 to 1.2 MA was correlated with a 30% increase in density. In addition to this trend with plasma current, a significant B_T dependence from 0.25 to 0.45 T was also observed. Statistical analyses of the data using various methods confirmed a strong, nearly linear scaling with B_T. The correlation between the density and current was accounted for in the statistical analysis, where the I_p dependence was found to be clearly less than linear, with a strong, accompanying density dependence. Using ordinary MLR, the scaling was found to be

$$\tau_E = 4.69 \times 10^{-9} B_T^{1.08} I_p^{0.57} n_e^{0.44} P_{loss}^{-0.73}. \qquad (8)$$

Accounting for the errors-in-variables, the 'PCEIV' method modified the coefficients somewhat, most notably in a weaker power degradation ($P_{loss}^{-0.50}$), but the other dependencies remained similar.

Early experiments on MAST found H-enhancement factors strongly dependent on ELM frequency, with H decreasing from 1.5 to 0.5 as the ELM frequency increased [73]. MAST data that were included in the ITER H-mode database also provided the means to determine an aspect ratio dependence relative to the IPB98y,2 scaling, with $\tau_E \propto (R/a)^{-0.81}$ when bean-shaped (PBX, PBX-M) and circular cross-section data were omitted [109]. Dedicated, single parameter scans were performed on MAST to determine the I_p and B_T dependence of thermal confinement, and dependencies similar to those on NSTX (equation (8)) were found. Figure 7, shows the total and electron stored energies as a function of I_p and B_T for MAST H-mode plasmas. The solid and dashed lines in the plots show the fit and the maximum and minimum slopes consistent with uncertainties in the data. The data, which consist of both ELM-free and ELMing discharges, clearly follow the NSTX trend, with a weaker than linear scaling with plasma current and a strong (even stronger than NSTX) dependence
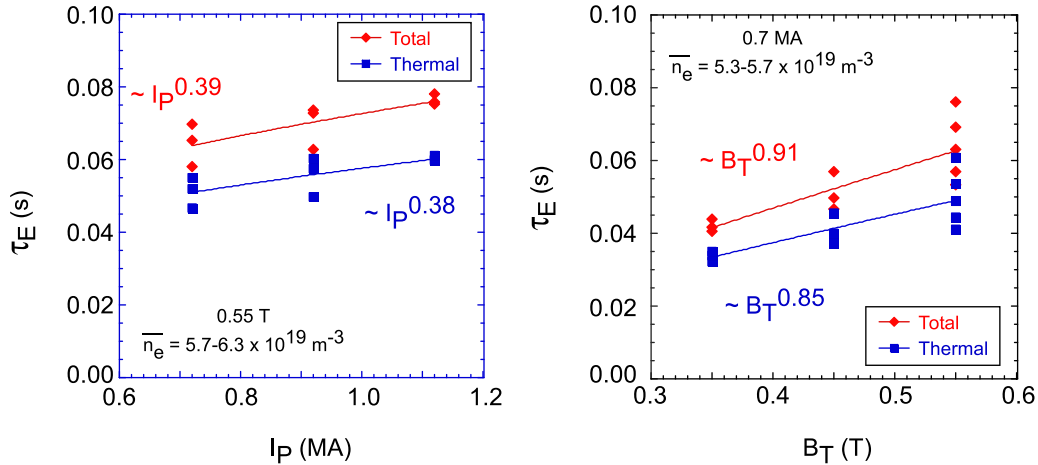
Figure 8. (left) Confinement time vs I_p and (right) vs B_T for NSTX H-mode plasmas with boronized walls. Reproduced courtesy of IAEA. Figure from [108]. Copyright (2007) IAEA.
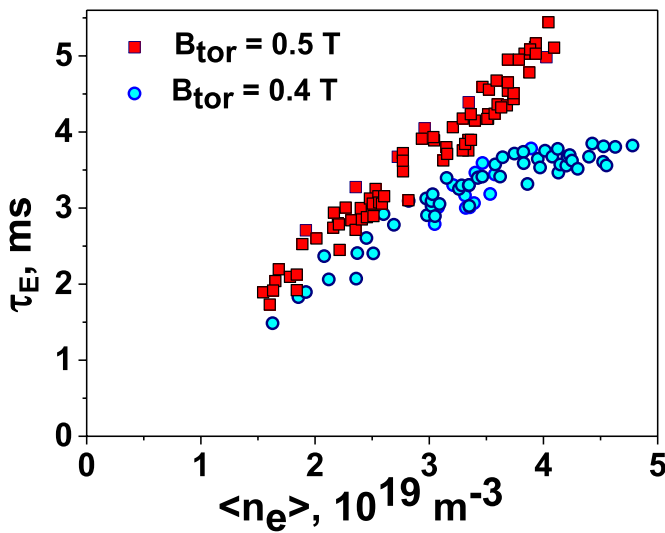
Figure 9. Dependence of energy confinement time on volume-averaged density on Globus-M. Reproduced courtesy of IAEA. Figure from [113]. Copyright (2018) IAEA.

on toroidal magnetic field. Given an estimate for fast ion content, the thermal energy confinement time at fixed density (1.1×10^{20} m^{-3}) in MAST was found to scale as

$$\tau_E = 0.186 B_T^{1.4} I_p^{0.59} P_{loss}^{-0.73} \tag{9}$$

similar to that in NSTX.

Later experiments in NSTX with boronized walls, but this time with only a small variation in density over the course of the scan, confirmed the weak I_p and strong B_T dependence. Figure 8 shows these trends.

The first neutral beam heating experiments in Globus-M showed a strong τ_E dependence on both I_p and B_T with $\tau_E \propto I_p^{0.8\pm0.1} B_T^{0.8\pm0.1}$ [111]. A subsequent study [112] refined the Globus-M scaling, and found that

$$\tau_E = 6.08 \times 10^{-3} B_T^{1.28\pm0.12} I_p^{0.48\pm0.21} n_e^{0.77\pm0.04} P_{loss}^{-0.54\pm0.26} \tag{10}$$
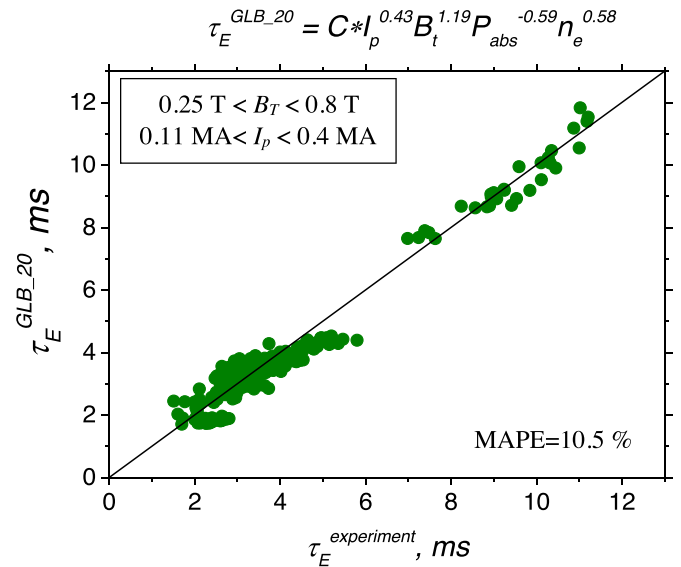

Figure 10. Comparison of the experimental confinement time values versus predicted values using the scaling given in equation (11). Reproduced courtesy of IAEA. Figure from [114]. Copyright (2021) IAEA.

consistent with scalings determined from MAST and NSTX data. It was found [113], however, that while $\tau_E \propto n_e B_T$, there are indications that confinement saturated above some, possibly B_T-dependent critical density (figure 9). Recent experiments on Globus-M2 with toroidal fields up to 0.8 T exhibited a B_T-dependent density saturation up to 0.7 T and found that the strong B_T scaling holds at these higher fields [114]. Figure 10, shows that the thermal confinement time from the combined Globus-M and Globus-M2 dataset, spanning the ranges of 0.25 T $< B_T <$ 0.8 T and 0.11 MA $< I_p <$ 0.4 MA is well represented by the scaling

$$\tau_{GLB20} \propto B_T^{1.19} I_p^{0.43} n_e^{0.58} P_{loss}^{-0.59}. \tag{11}$$

A study in NSTX that seemed to contradict the strong B_T scaling and weaker I_p scaling was one that was conducted with
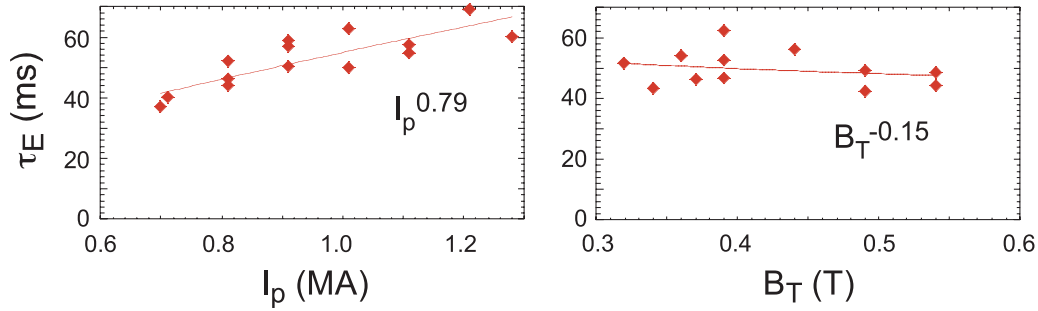
Figure 11. Thermal confinement times vs I_p (left) and B_T (right) for NSTX H-mode plasmas with lithium wall conditioning. Reproduced courtesy of IAEA. Figure from [120]. Copyright (2013) IAEA.

lithium conditioning of the plasma walls. To perform this type of wall conditioning, a downward facing lithium evaporator was utilized, with pre-shot lithium evaporation in the ranges of a few to up to 1000 mg. Lithium wall conditioning generally allowed for the discharges to achieve lower collisionality as compared to those with boronized walls. Additionally, at the lowest edge collisionalities in these lithiated plasmas, a fortuitous feedback between neoclassical ion energy transport and anomalous particle transport could be initiated, leading to a new regime, called the enhanced pedestal H-mode, in which the largest energy confinement enhancements were obtained [115–118]. Overall, the global and thermal electron energy confinement times in the lithium wall conditioned plasmas were found to increase linearly with amount of lithium deposition [119]. For modest amounts of lithium evaporation ($\sim$100 to 200 mg), dedicated, single parameter scans actually showed confinement scalings more similar to the ITER98y,2 scaling, with a nearly linear dependence on plasma current and a weak dependence on toroidal magnetic field (figure 11). These NSTX results that seem to contradict the NSTX confinement scaling given in equation (8) were reconciled by considering the variation of normalized confinement with collisionality, as will be discussed in the next sub-section on Dimensionless Variable Scalings.

Because NSTX and MAST operated at similar aspect ratio and plasma size, no size dependence in the ST confinement scalings could be deduced from these early studies. Furthermore, the Globus-M thermal confinement results in neutral beam heated plasmas were reported only recently. An approach to determining the size dependence in the ST scalings was performed by Buxton *et al* [121] under the assumption that the transport was controlled by plasma physics in a quasi-neutral plasma with no Debye length dependence. This assumption constrains fit coefficients for engineering parameters, including major radius, to guarantee that the fit is dimensionally correct (i.e. τ_E in *sec*.). In this work, the fit, including the size scaling, was based on the dataset used in Kaye *et al* [106]. It was recognized, however, that another assumption was required to mitigate the effect of correlations among the engineering variables in this dataset, and, therefore, assuming that the transport was gyroBohm, consistent with NSTX [108], the following scaling was developed:

$$\tau_E = 0.21 B_T^{0.91} I_p^{0.54} n_e^{-0.05} P_{loss}^{-0.38} R^{2.14} \qquad (12)$$

indicating a strong dependence on plasma size. Figure 12(a) shows a collection of START, MAST and NSTX data as a function of the IPB98y,2 scaling, while figure 12(b) shows the same dataset as a function of the scaling relation given above. The dataset is better described by equation (12) than by the IPB98y,2 scaling, with this scaling relation giving higher precision and accuracy.

Kurskiev *et al* [122] combined data from START, MAST, NSTX, Globus-M and Globus-M2 (up to 0.8 T) to derive the following size-dependent ST scaling, which is shown in figure 13. The scaling

$$\tau_{E,scal} = 0.066 I_p^{0.53} B_T^{1.05} P_{abs}^{-0.58} n_e^{0.65} R^{2.66} \kappa^{0.78} \qquad (13)$$

also indicates a strong dependence on plasma size.

The standard IPB98y,2 scaling, derived from devices with aspect ratio $R/a > 2.5$, has an aspect ratio dependence of $(R/a)^{-0.58}$, and it overpredicts the confinement time on STs, as can be seen in figure 2 in Kaye *et al* [123]. The ST data used for this comparison were taken from MAST and boronized-wall NSTX H-mode plasmas from the respective early experimental campaigns. The ST data was incorporated into the international multi-machine global confinement database not only for comparison, but also for assessing their effect on this aspect ratio scaling. A series of statistical studies were performed in Kaye *et al* [123], finding, with some minor modifications to the exponents of the other engineering variables, a stronger dependence on aspect ratio, with confinement scaling as $(R/a)^{-0.73}$ (see equation (3) of Kaye *et al* [123]); this indicates that confinement time improves as aspect ratio decreases, holding all other engineering variables fixed.

Local transport analyses were carried out in NSTX, MAST and Globus-M to understand the underpinning of the strong increase of confinement with toroidal field. In NSTX [108], it was found that the electron temperature profile broadened at fixed q, plasma current, heating power and density with increasing B_T (figure 14(a)), and this was accompanied by a reduction in the anomalous electron diffusivity for $r/a > 0.4$ (figure 14(b)). The ion temperature also increased with increasing B_T (figure 15(a)), but the ions remained in the neoclassical range in the outer half of the discharge (figure 15(b)). The electron transport was also seen to decrease in the outer half of the discharge with increasing current, but not as strongly as with increasing toroidal field, reflecting the weaker
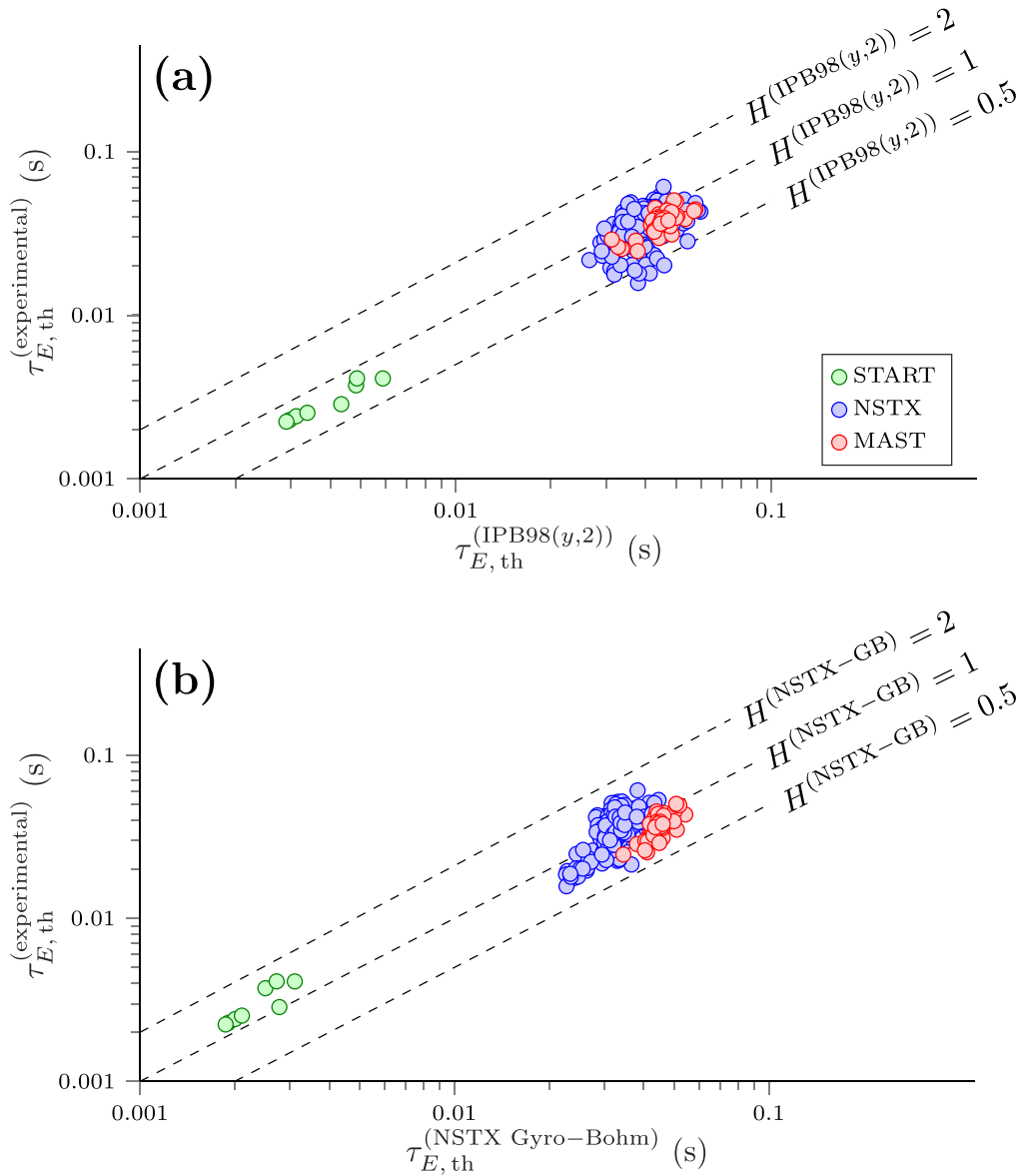
Figure 12. Comparison between (a) the IPB98y,2 scaling and (b) the NSTX gyroBohm scaling (equation (12)) and experimental data from START, MAST and NSTX. Reproduced from [121]. © IOP Publishing Ltd. All rights reserved.

dependence of confinement on I_p. The electron thermal diffusivity exhibited a strong decrease with increasing amounts of lithium deposition [119]. The variation of thermal diffusivities in the inner core of the plasma in NSTX may be controlled by energetic particle-driven modes [124], but no reduced model to characterize this has yet been developed.

Local transport studies in Globus-M were performed using the ASTRA code [111]. Because only a limited number of measured radial ion temperature points were available, T_i was calculated assuming a neoclassical ion thermal diffusivity. It was found for the range of B_T and I_p studied (0.4 to 0.5 T and 0.2 to 0.25 MA respectively), the measured T_i points fit well to the predicted profiles. Both T_i and T_e were found to increase with toroidal field at fixed I_p, and with increasing current at fixed B_T. The thermal diffusivities deduced from these analyses are shown in figure 16. The χ_e in the inner half

radius decreases with increasing B_T (unlike NSTX, where the decrease was in the outer half radius), while it decreases in the outer half radius with increasing I_p.

3.2. Dimensionless variable scalings

A more physics-based method of parameterizing energy confinement, one that connects more directly to neoclassical and turbulence theories of transport, is to cast the scaling in terms of dimensionless physics parameters. These include the normalized gyroradius ρ_*, beta β, normalized collisionality ν_*, and safety factor q, in addition to geometric parameters such as κ, δ, R/a, etc. The dimensionless variables relate to the engineering and plasma parameters in the following fashion:
$\rho_* = \frac{\rho}{a} \propto \frac{(MT)^{1/2}}{aB_T}$, $\beta \propto \frac{nT}{B_T^2}$, $\nu_* \propto \frac{anq}{\epsilon^{5/2}T^2}$. $q \propto \frac{B_T\epsilon a}{I_p}$, where M is
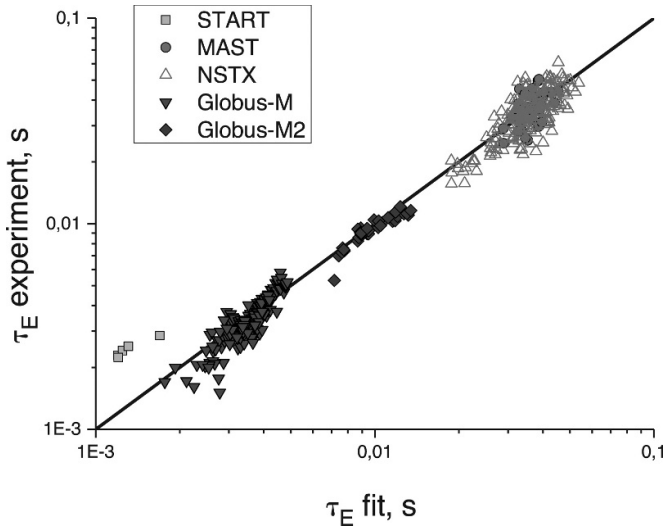
Figure 13. The results of the regression fit for the STs database. Reproduced with permission from [122].

ionic mass, $\epsilon = \frac{a}{R}$. T is plasma temperature, and n is plasma density. Additional parameters describing the plasma, such as the electron-ion temperature ratio T_e/T_i, and impurity content Z_{eff}, may be included as well.

In dimensionless form, the energy confinement can be written as

$$\Omega_c \tau_E \propto \rho_*^{\alpha_\rho} \beta^{\alpha_\beta} \nu_*^{\alpha_\nu} q^{\alpha_q} \ldots\ldots \quad (14)$$

where $\Omega_c \propto B$, is the ion cyclotron frequency, which is introduced to make the left-hand side of the equation dimensionless. The form above is consistent with the physics of confinement involving plasma phenomena that do not involve breaking the quasi-neutrality condition. Correspondingly, this constrains the powers of B, R, P and n in the form given in section 3.1, which can then be cast in terms of just three independent combinations, known as the 'Kadomtsev constraint' [125–127].

There are three primary approaches to determining the dimensionless scalings, each having pros and cons. The first is to use techniques such as MLR or PCEIV directly, as was done for the engineering variables. As can be seen from the definitions of the dimensionless variables, there are common engineering and plasma variables among them, potentially causing strong intercorrelations. Care must be taken, then, to identify and handle these correlations to avoid misleading results. The second approach is to use simple linear transformations from the engineering coefficients to the dimensionless variable coefficients based on definitions of the latter. This has been used previously for IPB98y,2, and for the ST scalings contained in Kaye *et al* [106], and is described nicely in Buxton *et al* [121]. Again, however, the correlations among the variables lead to extreme sensitivity in the transformed exponents; small changes in the engineering variable exponents can lead to large changes in the exponents of the dimensionless variable expressions. The third approach is based on experimental single parameter scans, for which careful discharge

tailoring is necessary to hold certain profiles fixed in order to fix the non-scanned dimensionless variables locally. Such experiments have been performed on conventional aspect ratio tokamaks [128, 129], and an attempt at this was made on MAST [130]. Other studies on STs focused on attempting to fix several dimensionless variables globally, while scanning another. This approach could not avoid inevitable variations in the 'fixed' parameters, as will be seen later in this section.

As was seen in section 3.1, there were stark differences between STs and conventional aspect ratio tokamaks in their parametric dependencies of τ_E on I_p and B_T. These differences are reflected in the dimensionless variable scalings as well, most notably in the dependence of normalized confinement on collisionality. It was recognized early on in MAST that plasmas at lower collisionality had higher confinement enhancements ($\tau_E/\tau_{E,98y2}$) than those at higher collisionality [109]. These results indicated a favorable collisionality dependence, with $H_{98y,2} \propto \nu_*^{-0.23}$ (as compared to $B\tau_{E,98y,2} \propto \nu_*^0$ for higher aspect ratio), and, although a correlation between ρ_* and ν_* existed, the effect on the collisionality exponent was deemed to be small.

Dimensionless parameter scans were performed in NSTX to investigate the dependence of confinement on $\nu_{e,*}$ (normalized electron collisionality) and β_T at constant q [131]. A factor of three variation in collisionality in the first scan was achieved in these boron-conditioned wall plasmas by varying the toroidal field and plasma current at constant B_T/I_p, while also varying plasma density at fixed heating power. These scans found a much stronger collisionality dependence than at higher aspect ratio, with $B\tau_E \propto \nu_{e,*}^{-0.97}$, although there was a $\sim$20% variation in both ρ_* and β_T across this collisionality range. Here, $\nu_{e,*}$ is the normalized electron collisionality. The β_T scan was accomplished by varying density and input power at constant B_T and q. The resulting near factor of three variation in β_T was accompanied by a 20% variation in ρ_* and $\nu_{e,*}$ across this range. The effect of these 20% variations in each of the scans was determined statistically to give a scaling range of $B\tau_E \propto \nu_{e,*}^{-0.7\pm0.2}\beta_T^{0.3\pm0.1}$, with an inverse correlation between the $\nu_{e,*}$ and β_T exponents. For this sensitivity analysis, the ρ_* variation was assumed to be in the gyroBohm range, with $\rho_{e,*}^{(-2.5\ to\ -3.5)}$.

Using a transformation from engineering to dimensionless variables, the authors in Valovic *et al* [110] found that for MAST H-mode plasmas,

$$B\tau_E \propto \rho_*^{-4.4} \beta^{1.0} \nu_*^{-0.74} q^{-2.1}. \quad (15)$$

The strong dependence on ρ_* and β was due to these variables having a strong correlation. The collisionality scaling was found to be strong, and consistent with that found on NSTX. The authors noted that this strong collisionality scaling was a consequence of the fact that $\alpha_I + \alpha_B \sim 2$ is much greater than their sum of 1.08 in the IPB98y,2 scaling. Assuming gyroBohm transport, the relation between the I_p and B_T exponents and those of the dimensionless variables is given by

$$\alpha_I + \alpha_B = (2 - 2\alpha_\beta)/(5/2 - \alpha_\beta - 2\,\alpha_\nu) \quad (16)$$
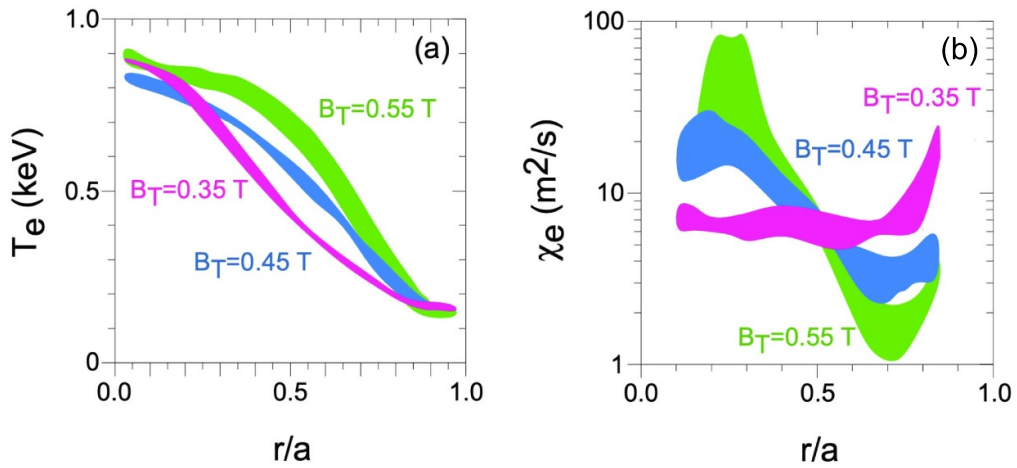
Figure 14. (left) Electron temperature and (right) electron thermal diffusivity as a function of r/a at various B_T in NSTX boronized wall H-mode plasmas. Reproduced courtesy of IAEA. Figure from [108]. Copyright (2007) IAEA.
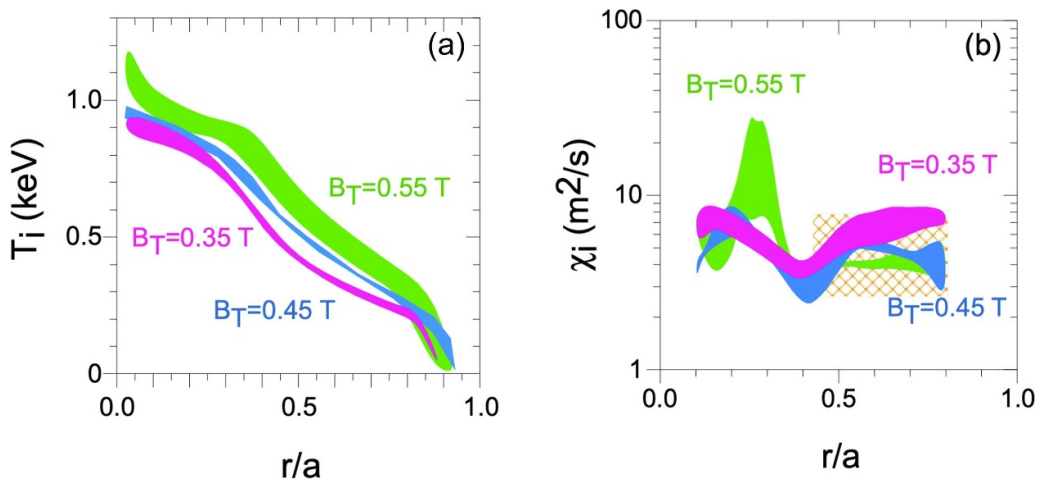
Figure 15. (left) Ion temperature and (right) ion thermal diffusivity as a function of r/a at various B_T in NSTX boronized wall H-mode plasmas. The yellow cross hatched region in the right-hand panel reflects the range of ion neoclassical thermal diffusivity over the range of B_T. Reproduced courtesy of IAEA. Figure from [108]. Copyright (2007) IAEA.
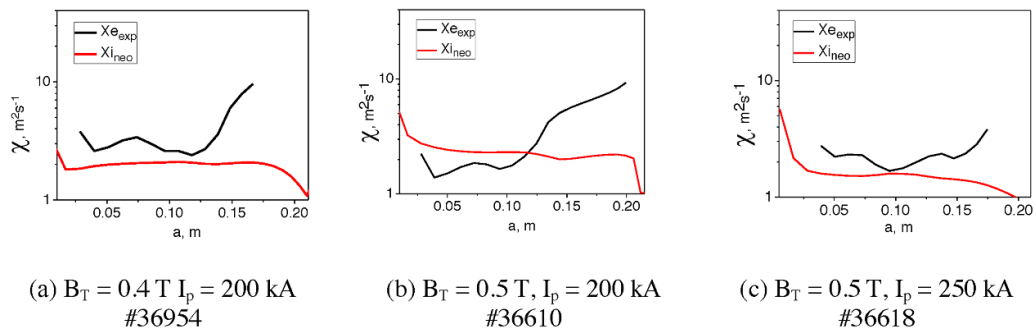
Figure 16. Electron and ion neoclassical thermal diffusivity at different B_T and I_p in Globus-M. Reproduced from [111]. © IOP Publishing Ltd. CC BY 3.0.
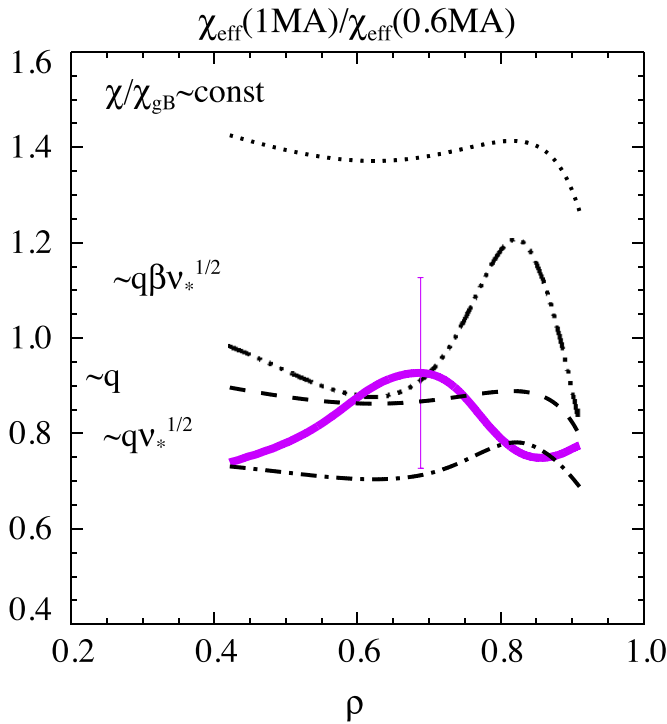
Figure 17. Pink line is the ratio of MAST experimental diffusivities, black lines are the ratios expected from different models calculated from n_e and T_e profiles and with $q \sim B_T/I_p$. Reproduced courtesy of IAEA. Figure from [110]. Copyright (2009) IAEA.

with the α_ν term being the dominant one that controls the $\alpha_I + \alpha_B$ sum. The authors found further that there was, additionally, a dependence on q. They noted these dependencies by comparing the effective thermal diffusivity χ_{eff} at two different currents with the assumption that the transport was gyroBohm ($\Omega_c \tau_E \propto \rho_*^{-3}$). The effective diffusivity treats the ions and electrons as a single fluid, and it is defined as $\chi_{\text{eff}} \propto Q_T/n\nabla T$, where it is assumed $T_e = T_i$, and Q_T is the total heat flux across a surface. The χ_{eff} ratios were found to be a factor of two lower than that expected if the transport was gyroBohm, but they could be reconciled if χ_{eff} also included dependencies on q, β and/or ν_* (see figure 17).

More controlled scans of the dependence of normalized confinement on dimensionless parameters were performed in MAST by tuning neutral beam power, magnetic field and plasma current in order to keep the plasma temperature and density profiles, and thus non-scanned dimensionless parameter profiles, similar [130]. Scans were performed to determine the ν_* and q dependencies of τ_E, with significant dependencies found in both. The results, shown in figures 18(a) and (b) are consistent with the scaling

$$B\tau_E \propto \nu_*^{-0.82\pm0.1} q_{eng}^{-0.85\pm0.2}. \qquad (17)$$

Here, $q_{eng} = 2\pi a^2 \kappa B_T/(R\mu_0 I_p)$. As can be seen in each scan, the other dimensionless variables were held fixed to within 10% in most cases.

The dimensionless variable scaling was extended through studies on NSTX [120]. As discussed in the previous section

on dimensional scalings, differences emerged in the I_p and B_T dependencies on NSTX when comparing discharges with boronized walls versus those with lithium wall conditioning. By constraining to limited ranges on both β and q to define subsets of data from each condition, it was found that these differences could be reconciled by expressing the normalized confinement as a function of collisionality. Figures 19(a)–(c) show the constrained data plotted as a function of collisionality. There was a variation of ρ_* across this range of collisionality, and this effect was taken into account by assuming three different dependencies of normalized confinement on ρ_*, with $B\tau_E \propto \rho_*^{0,-2,-3}$, reflecting a zero, Bohm and gyroBohm dependence. The fits lead to $-1.21 < \alpha_\nu < -0.79$ over the assumed range of exponents for ρ_*. Note that the boronized wall discharges do not achieve as low collisionality as the lithiated wall ones, although there is overlap between the two subsets in the $\nu_{e,*} \sim 0.1$ range. In this range, the normalized confinements of the two subsets are the same.

Dimensionless variable scaling studies have also been conducted in Globus-M neutral beam heated discharges with B_T up to 0.5 T [112]. Formal MLR of the Globus-M data found that

$$B\tau_E \propto \rho_*^{-2.7\pm0.12} \beta^{1.45\pm0.3} \nu_*^{-0.45\pm0.1} q^{0.85\pm0.05}. \qquad (18)$$

While this expression certainly indicates near gyroBohm scaling in terms of the ρ_* dependence, and a favorable, but not as strong dependence on ν_* as in MAST and NSTX, the dependence on q is actually inverted from that derived from MAST data (see equations (15) and (17)). It was pointed out by the authors of this work that the Pearson correlation coefficients indicated strong correlations among the variables, especially between β and q, which could account for the very different dependence. The addition of Globus-M2 data at higher B_T (up to 0.8 T) allowed for almost a factor of two lower collisionality than in the Globus-M dataset, and the resulting scaling with collisionality was found to be $B\tau_E \sim \nu_*^{-0.74}$ (see figure 20, where it was assumed that $B\tau_E \propto \rho_*^{-2.5}$ in order to compensate for the ρ_* variation over the dataset). The key finding here, is that, while the dependence on collisionality tends to become weaker at lower collisionality in higher aspect ratio devices [128], the Globus-M and M2 ST dataset indicates that as collisionality decreases the dependence actually strengthens, as is inferred by the results in equation (18) and figure 20.

As was done for the engineering variables, the ST data from NSTX and MAST were combined with the conventional aspect ratio data in the H-mode database to explore the scaling trends of normalized confinement with the dimensionless parameters [123]. The ST data had some, but not a major, effect on these combined scalings, which still showed a near gyroBohm dependence on ρ_*, a strong degradation with β, and a weak, but now slightly favorable scaling with ν_*. Applying different techniques that take into account data uncertainties, device weightings and different approaches (transforming engineering variable exponents vs direct regression) led to some variation in the dimensionless variable exponents (see table 2(b) in Kaye *et al* [123]), but the general trends for ρ_* and ν_* remained the same. There was a strong correlation between
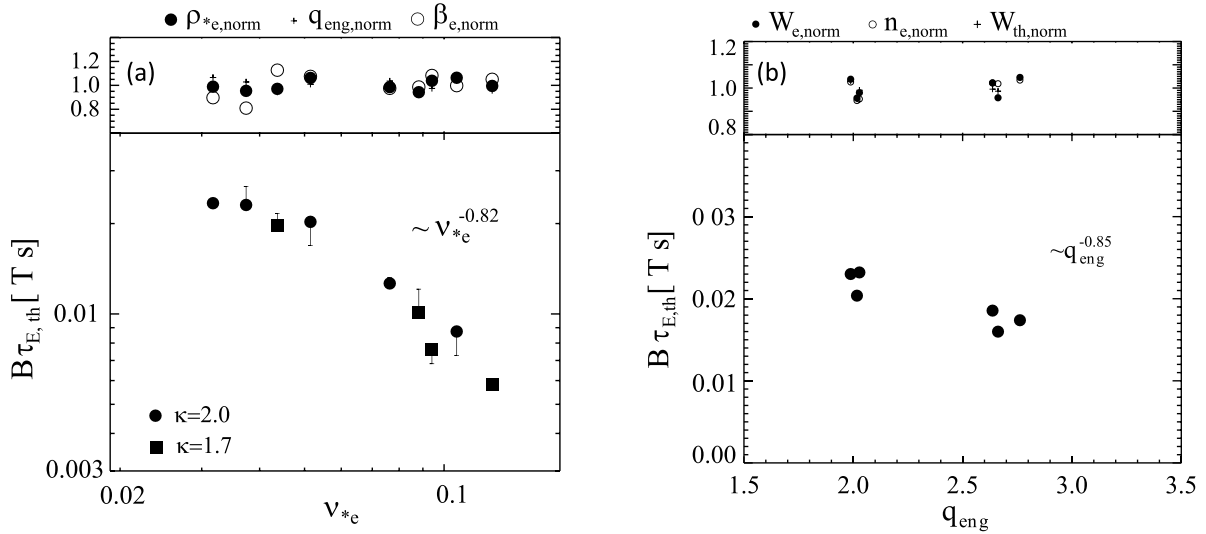
Figure 18. (a) Collisionality scan of thermal energy confinement time in MAST. Vertical bars show the size of the correction due to the variations in $\rho_{e,*}$, assuming gyroBohm scaling. Top panel shows variations of electron Larmor radius, β and q_{eng}, all normalized to average values along the scan. The scaling is based on $\kappa = 2$ data only. (b) Safety factor scan of thermal energy confinement time. Top panel show variations of electron energy content W_e, line-averaged density n_e, and thermal energy W_{th}, all normalized to average values along the scan. Reproduced courtesy of IAEA. Figure from [130]. Copyright (2011) IAEA.
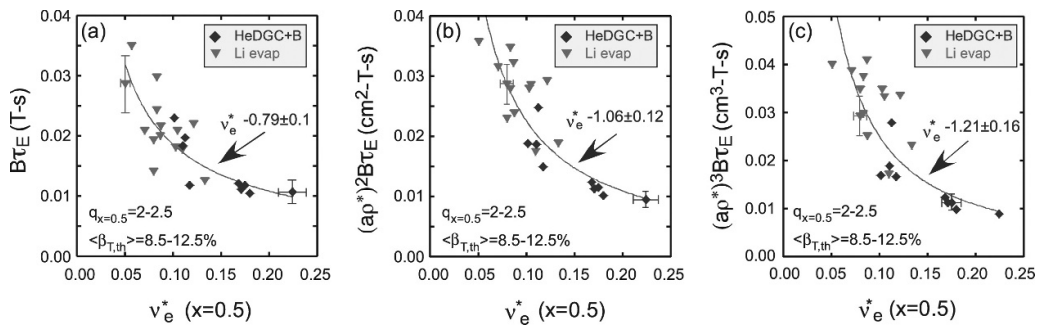

Figure 19. Normalized confinement time as a function of collisionality at $r/a = 0.5$ for NSTX H-mode discharges with boronized walls (blue points) and with walls conditioned through lithium evaporation (red points). Panels a through c assume no, Bohm and gyroBohm ρ_* dependencies respectively. Reproduced courtesy of IAEA. Figure from [120]. Copyright (2013) IAEA.

β and inverse aspect ratio ε in the database, which led to larger variations and correlated changes in the exponents of these parameters.

The local transport results in NSTX and Globus-M2 reveal the source of the strong favorable ν_* scaling in those devices, and especially why the different engineering scalings in NSTX discharges with different wall conditioning techniques are reconciled by examining the collisionality dependence. As was shown in figure 14, the electron temperature broadened for boronized wall conditioned NSTX discharges as B_T increased, leading to reduced electron thermal diffusivity. While I_p was held fixed in figure 14(a), a similar result was found for increasing B_T at constant q; as B_T increased and collisionality decreased, the T_e profile broadened in the mid-plasma region. This is also seen for lithium wall conditioned NSTX plasmas in figure 21, where the lithium conditioning was able to produce plasmas at even lower collisionality. There was an associated decrease in electron thermal diffusivity in the mid plasma region for these plasmas as well. Figures 22(a) and (b)

show the χ_e profiles themselves, and the profiles normalized to the gyroBohm parameterization ($\chi_e^{gB} \propto \rho_s^2 c_s/a$, where ρ_s is ion Larmor radius and c_s is ion sound speed at the electron temperature) respectively, color coded by collisionality, and the drop in χ_e is apparent. Interestingly enough, as the collisionality decreased, the ion thermal diffusivity became more anomalous; at the highest collisionalities, $\chi_i/\chi_i^{NC} \sim 0.5$, while at the lowest collisionalities $\chi_i/\chi_i^{NC} \sim 4$–5. How this particular behavior extends to the lower collisionalities obtainable in NSTX-U and MAST-U will be critical for establishing the physics basis of an ST pilot plant.

Globus-M shows an increase in T_e across the entire profile, and possibly a more peaked T_e profile, at lower collisionality (figure 23(a)). Accompanying this is a reduction in χ_{eff} (one-fluid effective χ) from the very core to $r/a \sim 0.6$ to 0.7 (figure 23(b)). Beyond this radius, the uncertainties in χ_{eff} are too large to draw any conclusions. It is worthwhile noting that while the decrease in χ_e in NSTX occurs outside the very core of the plasma, the reduction of χ_{eff} in Globus-M2 is
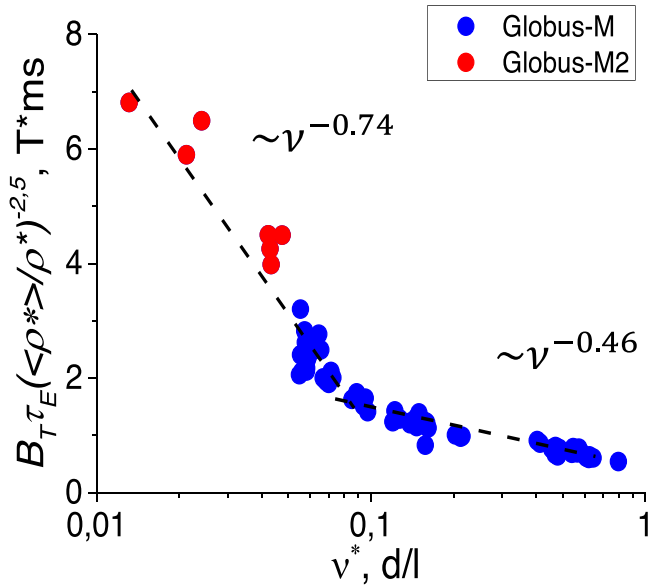
Figure 20. Normalized energy confinement versus collisionality assuming $B\tau_{E} \propto \rho_*^{-2.5}$. There was little variation of the dimensionless parameters q_{eng}, ρ_* and β across the range of collisionalities. Reproduced with permission from [132].
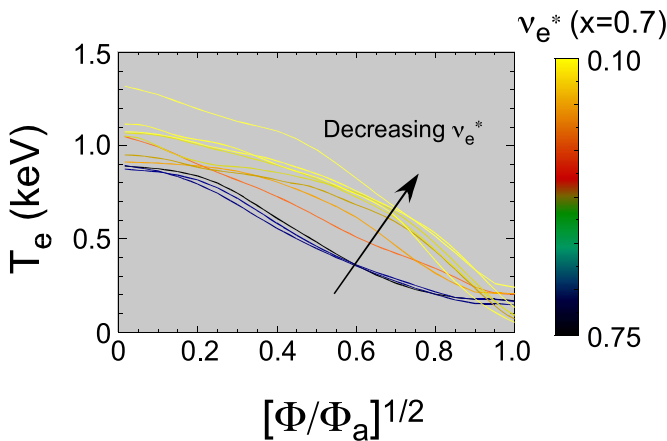
Figure 21. T_e profiles from NSTX for lithium wall conditioned plasmas color-coded by normalized electron collisionality at $r/a \sim 0.7$. Φ is toroidal flux. Reproduced courtesy of IAEA. Figure from [120]. Copyright (2013) IAEA.

most noticeable in the very core. We note that electron transport coefficients are subject to large uncertainties in the core of NSTX because high frequency energetic particle driven instabilities (discussed in section 7.4.4) may impact either electron heat transport or the NB power deposition profile in this region of the plasma.

4. Momentum transport

In this and following sections, we will adopt the nomenclature normally used in the literature for the following parameters: v_ϕ is the plasma velocity in the toroidal direction,

Γ_ϕ is the perpendicular flux of the toroidal momentum, and χ_ϕ is the toroidal momentum diffusivity in the perpendicular direction.

The toroidal rotation in neutral beam heated ST plasmas was found to be high, with thermal Mach numbers, $M_{th} = v_\phi/v_{th}$ up to 0.7 on MAST [130], and rotation velocities up to 1.6 times the carbon thermal velocity in NSTX [133]. These high toroidal rotation velocities, combined with high B_P/B_T in STs, result in strong radially sheared equilibrium $E_r \times B$ flow, γ_E, that acts to suppress many microinstabilities (with important consequences for STs that are discussed further in section 7). Flow shear can also have a strong effect on MHD stability [134], including its effect on sawteeth [135] and stabilization of the Resistive Wall Mode [136].

Momentum transport coeffcients, momentum diffusivity, χ_ϕ, and momentum pinch, v_ϕ^{pinch}, have been obtained in STs from measurements of the toroidal momentum flux Γ_ϕ, where

$$\Gamma_\phi = -mnR^2 \, \chi_\phi d\omega_\phi/dr + mnR^2 \, v_\phi^{pinch}\omega_\phi \qquad (19)$$

where ω_ϕ is the toroidal angular velocity. Both steady-state and perturbative momentum transport studies were carried out in neutral beam heated H-mode discharges in NSTX [137, 138]. An increase in central rotation velocity by 50% was associated with an increase in B_T from 0.35 to 0.55 T at fixed I_p. The rotation profile shape remained fairly constant over this range of B_T, as did the applied torque profiles, and the steady-state analysis, which neglects v_ϕ^{pinch}, indicated a reduction in the effective momentum diffusivity by up to a factor of four across the profile. On the other hand, at fixed B_T, while there was an increase in plasma rotation with increasing I_p, this was due more to a change in applied torque than in momentum transport; χ_ϕ showed little change over the variation in I_p. The momentum diffusivity was insensitive to the amount of lithium deposition except at the highest evaporation and lowest input torque levels, where χ_ϕ decreased by slightly less than a factor of two in the outer region of the discharge [119]. No dependence was seen in the inner region of the plasma. The magnitude of the steady-state momentum diffusivities inferred from experiment in the outer portion of the plasma, $r/a \sim 0.65$, generally yielded Prandtl numbers, $P_r = \chi_\phi/\chi_i$, in the range of 0.2–0.5.

Perturbation experiments performed using magnetic braking due to applied $n=3$ non-RMPs revealed inward momentum pinch velocities of 10–40 m s^{-1}. These significant inward pinches led to momentum diffusivities up to 7 m^2 s^{-1} larger than those determined by steady-state analysis (figure 24), and with corresponding Prandtl numbers in the range from 0.5 to 0.8. The Prandtl numbers in the inner region of the NSTX plasmas were lower. Analysis of MAST L-modes using steady-state analysis [139] exhibited a similar range of Prandtl numbers, with $P_r \sim 1$ for $r/a \sim 0.1$ to 0.7, but decreasing farther toward the edge (figure 25). Perturbation experiments using magnetic braking techniques similar to those used in NSTX were performed in MAST L-mode plasmas [140]. These low β targets complement the studies
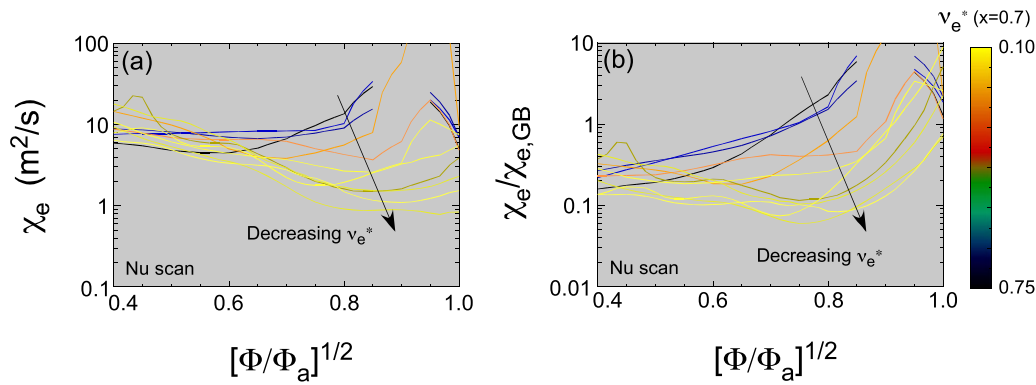
Figure 22. (a) χ_e profiles color-coded by electron collisionality at $r/a \sim 0.7$ for both boronized and lithium wall conditioned NSTX plasmas with minimal variation in β and q ('Nu scan'). This is from the same dataset as that shown in figure 21. (b) χ_e profiles normalized to χ_e^{gB} ($\propto \rho_s^2 c_s/a$). The profiles in both panels are color-coded by normalized electron collisionality at $r/a \sim 0.7$. Reproduced courtesy of IAEA. Figure from [120]. Copyright (2013) IAEA.
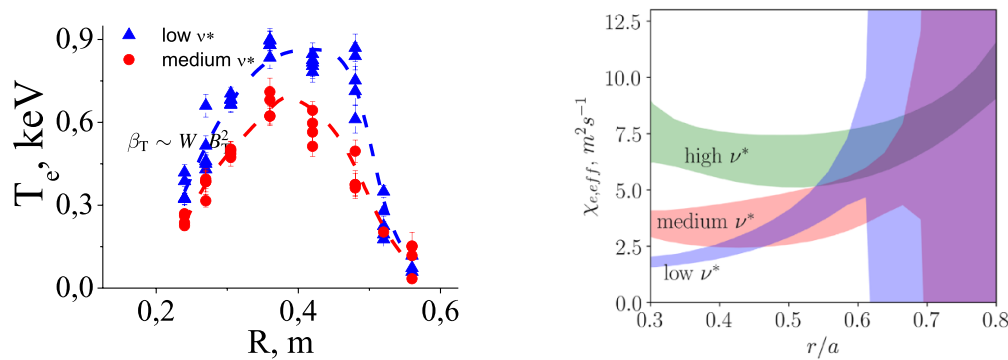
Figure 23. (left) Electron temperature profiles measured by Thomson Scattering for Globus-M plasmas at low ($\nu_* \sim 0.05$) and medium ($\nu_* \sim 0.1$) collisionalities. (right) Effective thermal diffusivity versus collisionality at fixed ρ_*, β_T, and q; high collisionality $\nu_* \simeq 0.4$, medium $\nu_* \simeq 0.1$, and low $\nu_* \simeq 0.05$. Reproduced courtesy of IAEA. Figure from [112]. Copyright (2019) IAEA.

in high β NSTX H-mode discharges. Linear GK calculations suggested that dominant low-k electrostatic turbulence could lead to only a weak pinch, or even outward convection. While this was consistent with observations, the experimental uncertainties were too large to provide a quantitative validation of the theory predictions.

The inferred pinch velocities in NSTX were compared to those predicted by the theories of Peeters [142] and Hahm [143], which were based on momentum transport by low-k turbulence. Both theories found $v_\phi^{pinch} \propto \chi_\phi/R$, although the Peeters theory included an additional dependence on density gradient scale length, L_n. A comparison of the theory predictions with the measured values of v_ϕ^{pinch} in the outer region of the NSTX plasmas is shown in figure 26. While both theories give reasonable agreement with the valued inferred from experiment for low v_ϕ^{pinch}, the Peeters theory appears to fit better for larger v_ϕ^{pinch}, which is where L_n tends to be smaller. Neither theory fits the data well in the inner region ($r/a \leqslant 0.35$), and, interestingly, linear GK simulations indicate that ITG/trapped electron mode (TEM) modes are unstable in the outer region, where there is agreement, but they are stable in the core, where the agreement is poor.

The Peeters theory dependence on density gradient scale length can also explain the apparent reduction in Prandtl number toward the edge in the MAST L-mode discharges (figure 25). In this region, L_n is small, and including the Peeters predicted inward pinch results in a χ_ϕ two times greater than that inferred from the steady-state analysis shown in figure 25, and brings the Prandtl number closer to 1.

It is worth noting here that $\chi_\phi/\chi_i \sim 0.5$ to 1, reflecting a low-k turbulence drive, in both NSTX and MAST H-mode discharges despite the ion energy transport being close to neoclassical in both devices. While the neoclassical ion energy transport is large and dominates any residual ion energy transport due to low-k turbulence, the neoclassical momentum transport is near zero and subdominant to that induced by whatever level of electrostatic low-k turbulence exists in these plasmas. Thus, this raises the question of whether momentum transport may be a better indicator of the residual electrostatic low-k turbulence than ion energy transport in ST H-modes.

Intrinsic rotation in the co-I_p direction has been observed in NSTX [144] and MAST [145]. In NSTX, the carbon intrinsic rotation was measured by passive charge-exchange in the outer
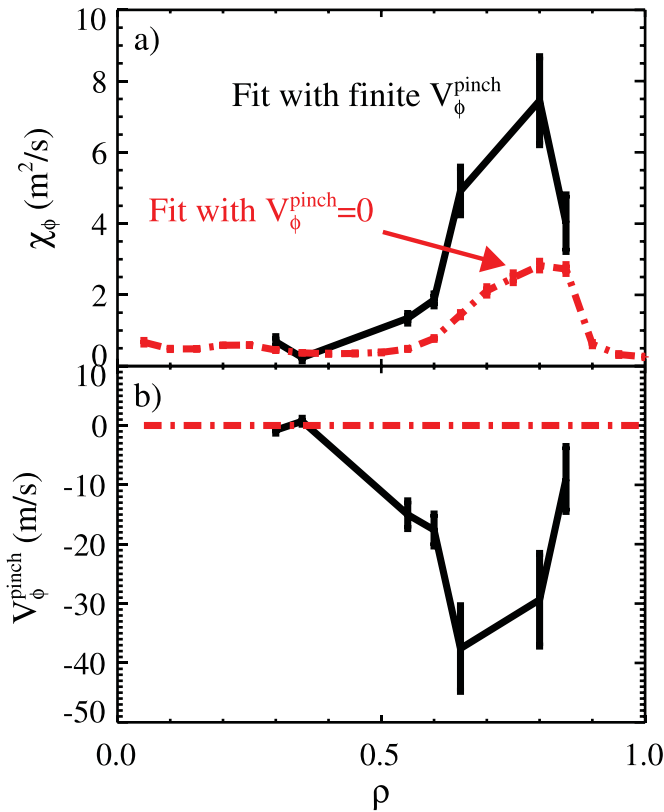
Figure 24. (a) Momentum diffusivity and (b) momentum pinch velocity inferred using $n = 3$ non-RMPs to an NSTX H-mode plasma. For comparison, the inferred diffusivity neglecting any momentum pinch is also shown (dashed). Reprinted figure with permission from [137], Copyright (2008) by the American Physical Society.
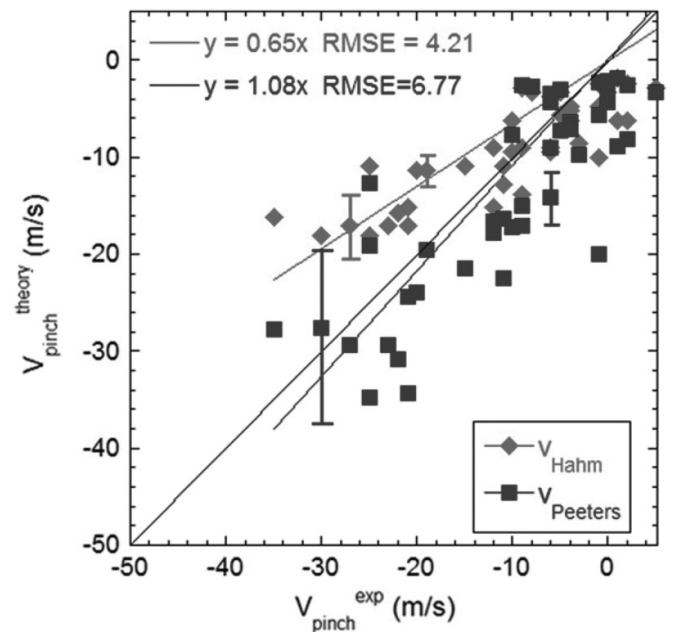

Figure 25. Profile of the Prandtl number calculated from TRANSP [141] analysis of MAST L-mode (green) and H-mode (magenta) discharges. Reproduced courtesy of IAEA. Figure from [137]. Copyright (2008) IAEA.

Figure 26. v_ϕ^{pinch} as computed by the Hahm (red) and Peeters (blue) theories versus experimentally inferred values for the outer region of NSTX H-mode plasmas. Reproduced courtesy of IAEA. Figure from [138]. Copyright (2009) IAEA.

part of the discharge following Ohmic L to H transitions. The magnitude of the rotation was found to be correlated strongly with the carbon ion temperature gradient, and a simple theoretical treatment was employed to determine the intrinsic torque. The intrinsic torque was found to scale as $\hat{s}\chi_i/L_{Ti}$, where $\hat{s} = (r/q)dq/dr$, and general agreement was found between theory and experiment for χ_i in the range of 0.5–6 m^2 s^{-1}, values consistent with those derived from NB-heated plasma transport studies in NSTX. Doppler backscattering spectroscopy (DBS) measurements on MAST showed rotation reversals, from the co-I_p to the counter-I_p direction as the ratio n_e/I_p increased. Co-I_p rotation was associated with lower normalized collisionality, reflecting the plateau regime of neoclassical transport. This result was examined in the context of a 1-D model of the intrinsic turbulent momentum flux driven by neoclassical non-Maxwellian corrections to the equilibrium distribution function [146, 147]; this momentum flux is inwards at low ν_* and reverses to become outward for $\nu_* > 1$. Integrating the model momentum flux to predict the flow profile, assuming a Prandtl number of 0.7, successfully captures the observed reversal of rotation with increasing collisionality, and the rising reversal density with increasing plasma current.

5. Particle transport

Particle transport in STs has received less attention than heat transport, but there have been several published studies. In MAST H-modes [109] the core density profiles, fueled by core neutral beam injection and neutral penetration from the outer regions, have been observed to be rather flat. Evolution

of the core density profile has contributions from the neutral beam source, the neoclassical Ware pinch and the diffusive particle flux. The diffusive particle flux was found to be almost zero in the core, where the observed dn_e/dt is dominated by the NB source and the Ware pinch. Since the density profile is almost flat, the diffusion coefficient is indeterminate. In a NSTX H-mode plasma with a steep radially localized density gradient at $0.5 < r/a < 0.6$, the particle diffusivity in this region has been determined experimentally from particle balance (TRANSP) to lie in the range $0.2 \text{ m}^2 \text{ s}^{-1} < D < 1.0 \text{ m}^2 \text{ s}^{-1}$, and it is consistent with nonlinear global GK simulations of low-n dissipative-trapped-electron turbulence [148]. Experiments with varying levels of lithium (Li) wall conditioning have been carried out on NSTX. Interpretive edge transport modeling of these plasmas using SOLPS [149] suggests that the impact of increasing Li is to reduce the effective particle diffusivity substantially at $0.8 < r/a < 0.94$ and increase it slightly at $0.94 < r/a < 1$ [119]. Conceptual designs of high fusion performance steady state STs require peaked density profiles to achieve core high fusion power and efficient off-axis current drive, and clearly particle transport will be crucial [109].

There are additional studies of impurity transport. MAST experiments with a time dependent He gas-puff have revealed that in L-mode plasmas at $I_p = 700$ and 900 kA, impurity transport was anomalous, with both diffusion and pinch decreasing with increasing I_p [150]. However, in an H-mode MAST experiment with comparable parameters at $I_p = 900$ kA the n_{He} profile peak did not penetrate inwards of mid-radius: impurity transport was close to neoclassical, with $D_{He} \sim \chi_i$, and an inward convection near the edge decreases and reverses to become outward at mid-radius [150]. Linear GK analysis at $r/a \sim 0.7$ suggests TEMs are responsible for anomalous impurity transport in L-mode, and that TEM are stable in H-mode because R/L_n is lower. Subsequently the L-mode discharge at $I_p = 900$ kA was repeated with gas puff sources of C and N to assess the dependence of light impurity transport spanning from He to N [151]. These experiments show a weak screening of C and N from the core, while the He profile was found to be peaked. Impurity transport coefficients in N and C were consistent with neoclassical theory for $r/a < 0.4$, but anomalous farther out: $D_{N,C} \sim 1\text{–}10 \text{ m}^2 \text{ s}^{-1}$, with a strong inward convective pinch $V_{N,C} \sim -40 \text{ m s}^{-1}$ near the plasma edge that becomes outward at mid-radius (see figure 27). These features are well described by the combination of neoclassical theory with a quasi-linear calculation of the anomalous impurity transport, which is again attributed to TEM in these plasmas [151].

Perturbative experiments using Neon gas injection into L-mode NSTX discharges found that the Ne impurity did not penetrate inside $r/a \sim 0.5$–0.6 before the onset of MHD activity and the measured impurity diffusivities were both compatible with neoclassical predictions and consistent with the low observed level of ion heat transport [154, 155].

Sources and transport of lithium and carbon were studied in lithium wall conditioned ELM-free NSTX discharges [156]. While carbon accumulation was observed in the plasma core,
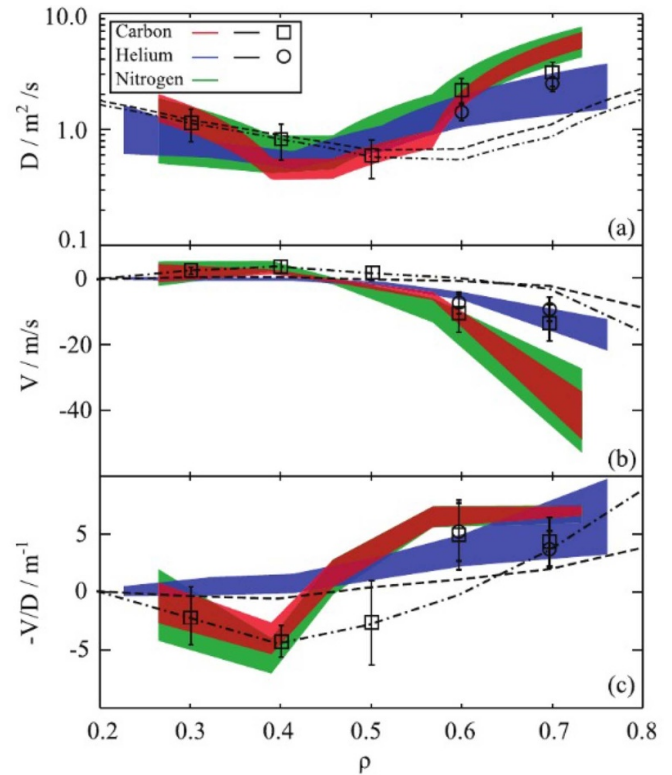
Figure 27. Radial profiles of transport coefficients for light impurities He, C, N measured in MAST, showing: (a) diffusivity, D; (b) convective velocity, V; and (c) the corresponding steady state impurity peaking factor, $-V/D$. NEO [152, 153] simulations of the neoclassical impurity transport coefficients for He and C are shown as dashed and dash-dotted lines. The quasilinear and neoclassical transport coefficients for He and C have been summed at $r/a = 0.6$ and $r/a = 0.7$, and they are indicated by symbols. Reproduced from [151]. © IOP Publishing Ltd. All rights reserved.

lithium densities remained below 1% of the carbon density. Lithium erosion at the divertor plate was found to be consistent with physical and temperature-enhanced erosion [157] while the application of lithium on graphite plasma facing components led to a moderate reduction in carbon sputtering. Toroidal asymmetries in divertor impurity influxes were found to be due to leading edges of divertor tiles (for carbon) and the toroidally asymmetric deposition from the lithium wall conditioning evaporators (for lithium) [158]. The latter toroidal asymmetries, in particular, could lead to inaccuracies in determining the total source of lithium impurities. Parallel scrape-off layer transport studies with the fluid edge transport code UEDGE [159] indicate stronger retention in the divertor for lithium impurities compared to carbon due to their shorter ionization mean free path and weaker classical parallel forces [160].

The core transport codes NCLASS [161], NEO [152, 153] and MIST [162] were used to study the impact of lithium conditioning on both the lithium and carbon core radial transport. It was found that changes in neoclassical transport due to changes in the deuterium temperature and density profiles together with the disappearance of ELMs could account for the increased carbon content in lithium wall conditioned discharges, although some additional anomalous transport was

needed to reproduce the evolution of the carbon profiles. Enhanced outward lithium transport due to the collisional coupling between that species and carbon partly explains weak core lithium accumulation, although the calculations also showed quantitatively that a reduced edge source of lithium was necessary to account for the low lithium density, which is consistent with the stronger divertor retention observed in the UEDGE simulations. The intrinsic impurities were found to behave neoclassically in H-mode discharges with boronized walls.

6. Internal transport barriers

A requirement for fusion power plants of any aspect ratio is to operate with low recirculating power by maximizing the plasma self-driven current, known as bootstrap current. This motivates the development of plasma scenarios with the large pressure gradients needed to drive bootstrap current. Of course, tailoring and controlling the pressure profiles is necessary to maintain plasma stability while simultaneously optimizing the self-driven current. ITBs have been explored as one route to this goal. Akin to the Edge Transport Barrier that is typical of H-mode plasmas, ITBs form farther toward the core, and they can manifest in all or some of the plasma profiles of electron temperature, density, ion temperature and plasma rotation. These ITBs are tightly coupled to either or both the magnetic or rotational shear, depending on the channel.

The development of ITBs has been observed in both MAST and NSTX L-mode plasmas. The first ITBs in MAST were generated using early neutral beam injection into low density $(1.5 \times 10^{19}$ m$^{-3})$ L-modes during the current ramp-up phase with either co- or counter-I_p injection [163, 164]. In these plasmas, the L-H transition was suppressed by using low field side fueling and operating in a disconnected Double (i.e. slightly Lower Single) Null Divertor configuration; both serve to raise the L-H power threshold. In these early studies, it was noted that the ITB region, taken to be the location of the strongest profile gradients, was generally associated with steep $d\omega_\phi/dr$ and weak or negative magnetic shear, $\hat{s}$. In the studies on MAST, the q and $\hat{s}$ profiles were determined from magnetic diffusion calculations in TRANSP. With co-injection, ITBs were seen in the T_i, T_e and v_ϕ profiles, with the T_i ITB forming and developing out to $r/a = 0.4$–0.6. In counter-injection discharges, the core rotation was found to be comparable to that with co-injection; the decrease in torque due to the enhanced lost energetic particles was compensated by the enhanced $j_r \times B$ due to the loss. In these counter-injection discharges, the ITBs were located at $r/a = 0.6$–0.7, and were observed in both T_e and n_e.

Subsequent ITB studies were carried out in MAST incorporating more detailed profile measurements, including that of the magnetic field pitch, a measurement on which the determination of the q and $\hat{s}$ profiles could be made [165, 166]. The more detailed comparison between co- and counter-injection ITBs indicated that particle confinement and density in the counter-injection ITB tended to be higher than that with co-injection, and while the total stored energy in the
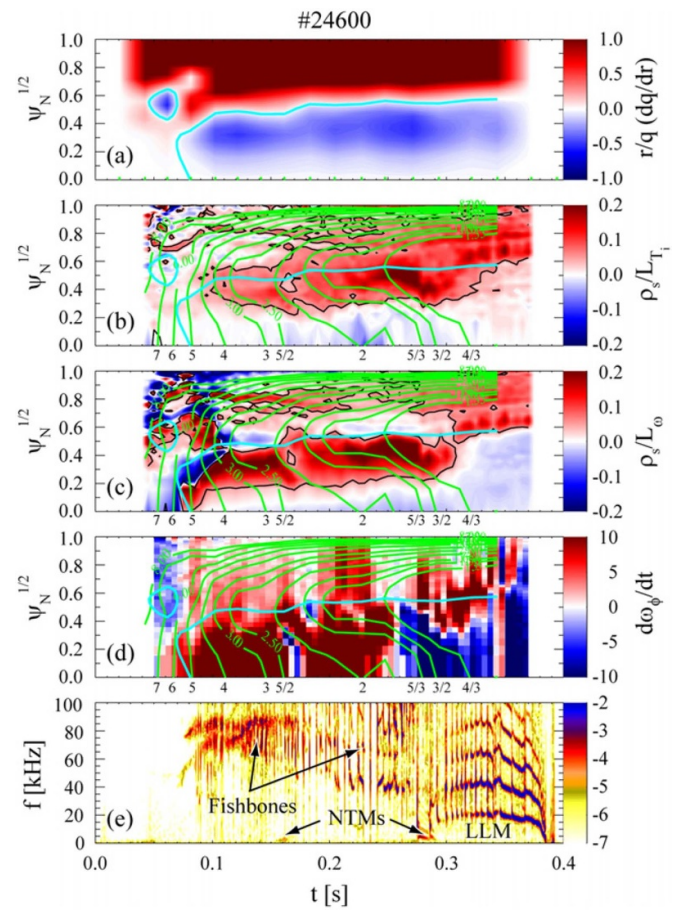

Figure 28. Evolution of (a) magnetic shear, (b) normalized ITG ρ_s/L_{Ti} and (c) toroidal rotation ρ_s/L_ω gradient, (d) rate of change in toroidal rotation ω_ϕ and (e) MHD in co-NBI MAST ITB discharge. Locations of rational surfaces (green, labeled below plots) and q_{min} (cyan) are also shown. Reproduced courtesy of IAEA. Figure from [165]. Copyright (2011) IAEA.

co-injection ITB was higher than that with counter-injection, most of that was due to the fast particle component, and the thermal stored energies in the two were comparable.

Figure 28 shows the time evolution for the co-injection ITB profiles of the magnetic shear, gradients in ion temperature and rotation, $d\omega_\phi/dt$ and MHD activity. No electron temperature or density ITB is seen with co-injection. The ion temperature ITB forms near the location of q_{min}, while the rotation ITB is localized to a region of maximum negative $\hat{s}$, which is a few cm inside of q_{min}. In these plasmas, transport analysis indicates $\chi_i \sim \chi_i^{NC}$ inside the ITB; outside, $\chi_i/\chi_i^{NC} \sim 4$–10. With time, the coupling of MHD and energetic particle-driven modes gives rise to enhanced neoclassical toroidal viscosity braking of the plasma rotation, reducing the rotation gradient and the strength of the T_i ITB. The ITB is finally 'destroyed' at the onset of an internal kink mode as the central q value, $q_0 \sim 1$.

The counter-injection ITB is different from that with co-injection in several respects. The magnetic shear is only weakly negative in the core region ($r/a < 0.4$), but because of enhanced fast particle loss, the $E_r \times B$ shear gradient extends
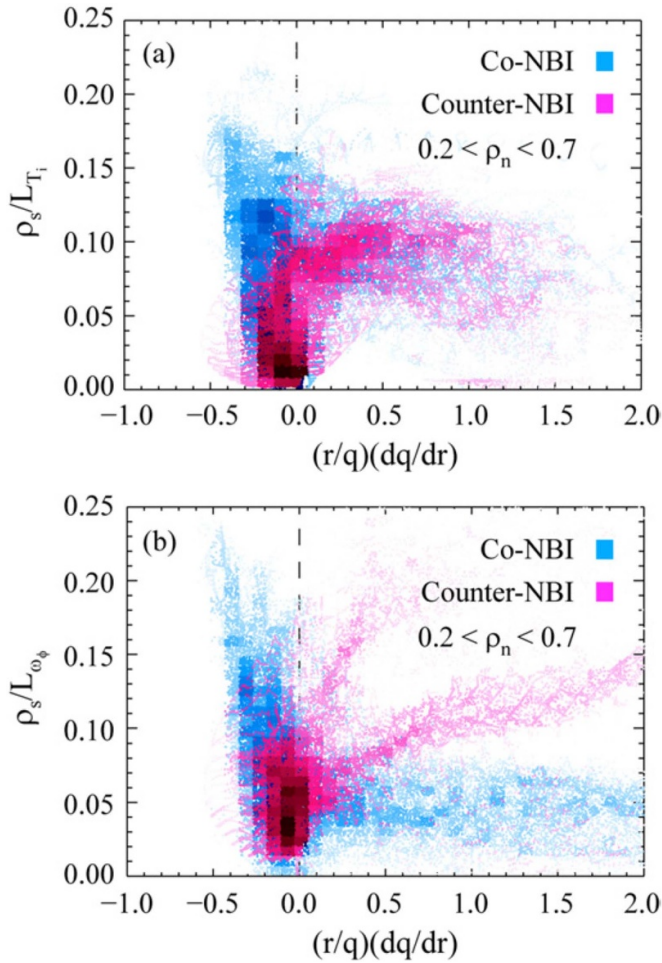
Figure 29. Dependence of normalized gradients of ion temperature ρ_s/L_{Ti} (a) and rotation rate $\rho_s/L_{\omega,\phi}$ (b) on magnetic shear $\hat{s}$ for several MAST ITB discharges with co- or counter-NBI heating. Reproduced courtesy of IAEA. Figure from [165]. Copyright (2011) IAEA.

across a broad region of the peripheral plasma, quite different than for the co-injection case. Field *et al* [165] found localized maxima in ρ_s/L_{T_i}, related to q_{min} (the minimum q value) passing through rational values, but no clear indication of a maximum gradient in either T_i or T_e, unlike the earlier studies. Steep density gradients were also observed at the edge and in the $\hat{s} < 0$ region inside $r/a \sim 0.4$. In these discharges, at $r/a = 0.4$, $\chi_\phi/\chi_i \sim 0.1$–$0.3$ and χ_i is within a factor of two of χ_i^{NC}.

The statistical dependence of the T_i and v_ϕ rotation gradients on magnetic shear is shown in figure 29. It is seen that for co-injection ITB discharges, the large ρ_s/L_{Ti} and $\rho_s/L_{\omega,\phi}$ are more localized to the negative $\hat{s}$ region. For counter-injection, $\rho_s/L_{\omega,\phi}$ evolves to higher values, and bifurcates, as $\hat{s}$ increases to more positive values. Microinstability analyses for the co-NBI ITBs will be summarized in section 7.1, but the results indicate that negative $\hat{s}$ is sufficient to stabilize low-k modes inside q_{min}.

Observations of ITBs were made also on NSTX, and the analysis here focused on high-k, electron-scale turbulence effects [167, 168]. It was found in this work that with sufficient

negative $\hat{s}$, the electron temperature profiles were no longer stiff, and their gradients could exceed critical gradients for electron temperature gradient (ETG) modes by a large margin. The ITBs in the various channels formed early in L-mode discharges with either Neutral Beam or HHFW RF heating, with the formation reflected by a rapid rise in both $T_e(0)$ and $T_i(0)$. The profile gradient scale lengths, along with q and magnetic shear profiles for a developed ITB are shown in figure 30. It is seen that the innermost T_e ITB is close to but a few cm inside the minimum $\hat{s}$, while farther out the T_i ITB is just outside the peak R/L_{v_ϕ} and a few cm inside q_{min}. There is no n_e ITB, and the rotation ITB location, as in MAST, lies very close to the maximum negative $\hat{s}$, a few cm inside q_{min}. Consequently, it appears that that $E_r \times B$ shear is important for suppressing modes causing ion transport, while negative $\hat{s}$ is more important for electron transport suppression.

In these NSTX ITBs, the electron temperature profile is no longer pinned by strong stiffness to the marginal R/L_{T_e} threshold for the onset of ETG, which will be discussed in section 7.3, and which is shown in figure 38(a). The measured high-k turbulence amplitudes are up to a factor of ten lower at the ITB location, where R/L_{T_e} is very high. $E_r \times B$ shear was not responsible for these T_e ITBs; high-k turbulence was found to be suppressed using torque-free HHFW heating only, where the $E_r \times B$ shear was measured to be near zero. At the location of the ITBs, $\chi_i \sim \chi_i^{NC}$, and $\chi_e < \chi_i^{NC}$. The GK studies of these plasmas are summarized in section 7.3.

7. Gyrokinetic analysis and turbulent fluctuations

The τ_E scaling expressions described in section 3 are a valuable guide to ST confinement, but understanding their ranges of validity and physical basis requires deeper knowledge of turbulent transport. Extensive investigations of microinstabilities in START, MAST, NSTX, Globus-M, and conceptual designs of burning STs [7, 32] have used gyrokinetic (GK) calculations with local codes GS2 [169], GYRO [170] (also capable of global simulations), and GKW [171], and global codes including finite ρ_* effects such as GTS [148] and ORB5 [172, 173]. This section reviews what GK calculations have revealed about core turbulence and anomalous transport in STs, focusing on heat transport; momentum transport was discussed in section 4, and particle and impurity transport were covered in section 5.

Beneficial impacts of equilibrium geometry on ST microstability [1] were uncovered in early studies motivated by START and NSTX [31, 174, 175]; favorable magnetic drifts allied with higher dp/dr in STs, were found capable of suppressing drift-wave instabilities that drive anomalous transport [32]. Furthermore, in experiments with tangential NBI, the compact nature of the ST leads to high toroidal flows that can act to suppress the turbulence, especially at ion-scales [176], though the externally driven flows are expected to be modest in an ST reactor. On the other hand, trapped electron modes (TEMs), driven at steep dn/dr should be boosted in STs by the larger trapping fraction. At the high β accessible in STs [51, 108], electromagnetic modes including kinetic
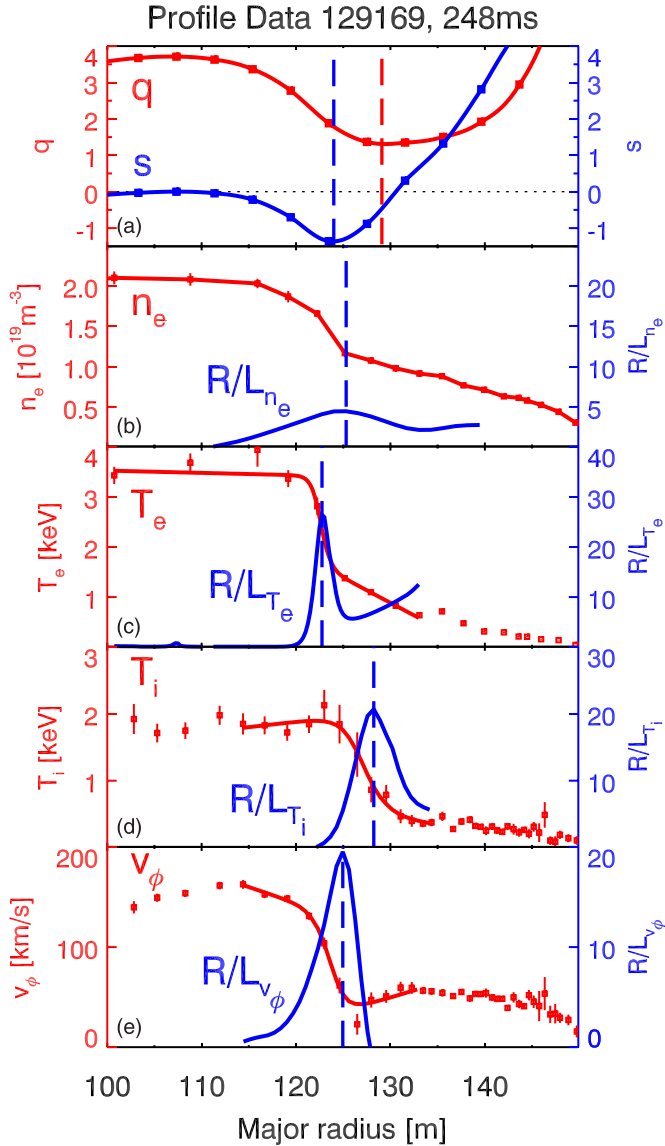
Figure 30. Kinetic profiles of an NSTX ITB. Using the left-hand axes are (a) q, (b) electron density n_e, (c) electron temperature T_e, (d) ion temperature T_i and (e) toroidal velocity v_ϕ. Using the right hand axes are (a) magnetic shear, $\hat{s}$ and (b)–(e) the normalized inverse gradient scale lengths. Vertical dashed lines indicate radial positions of interest for q_{min}, maximum negative $\hat{s}$, and peak normalized inverse gradient scale lengths. Reprinted from [167], with the permission of AIP Publishing.

ballooning modes (KBMs) [177, 178], microtearing modes (MTMs) [179, 180], and fast particle driven global and compressional Alfven eigenmodes (GAEs, CAEs) [124, 181] may become unstable and complement the usual electrostatic ion and electron temperature gradient (ITG, ETG) driven modes.

ST heat losses through the ion channel are often close to neoclassical in the plasmas and collisionalities accessed in ST H-mode plasmas so far [72, 108, 182–184]. Ion heat losses have been observed, however, to become more anomalous at lower collisionality in NSTX plasmas, where at lower ν_* linear GKs finds hybrid TEM/KBM modes with growth rates exceeding γ_E across more of the plasma cross section

[120]. The ion neoclassical transport in STs is higher than that at conventional aspect ratio, but it is still usually dominated by electron heat transport, which has therefore received more attention [185, 186]. The following sub-sections review GK studies of ST core plasmas, organized by mode type and normalized binormal wavenumber, $k_y\rho_i$, and give holistic microstability overviews for several selected topics, including H-mode pedestal, lithium conditioning, pellet fuelling, high power, and long pulse plasmas.

7.1. Ion scale modes at $k_y\rho_i \leqslant O(1)$: (excluding MTMs)

Local microstability studies have identified a range of unstable modes at $k_y\rho_i \leqslant O(1)$ in the core of STs. In MAST L- and H-modes these include: ITG, TEM driven at higher R/L_n [177, 180, 187], ion-driven TEM (coined the 'ubiquitous mode') [188, 189], electromagnetic modes destabilized by finite-β including KBM and MTM (MTMs will be discussed in the next section) [177]. Similar modes are also found in NSTX, where broader ranges in ν_* and β are accessible. In low ν_* NSTX H-modes, hybrid TEM/KBM modes become unstable at the edge and may be linked with increasingly anomalous Q_i [120]. In a high β NSTX plasma GYRO finds an electromagnetic hybrid ITG-KBM mode (destabilized by $\delta B_\parallel$) dominating ion-scales at $r/a = 0.7$ [190]. Globus-M finds R/L_{Te} is constant and clamped by TEMs at mid-radius at the lower $\nu_{e,*}$ end of an Ohmic density scan [104]. An analytic approximation to the critical ETG for TEMs [191] is given by:

$$\frac{R}{L_{Te,crit}^{TEM}} = \frac{0.357\sqrt{\epsilon} + 0.271}{\sqrt{\epsilon}}$$
$$\times \left[4.9 - 1.31\frac{R}{L_n} + 2.68\hat{s} + \ln(1 + 20\nu_{eff})\right]. \quad (20)$$

In the density ramp $R/L_{Te,crit}^{TEM}$ and τ_E increase while $R/L_{Te,crit}^{ETG}$ [192] decreases with increasing n_e, until τ_E saturates at a transition from TEM to ETG turbulence above $n_e \sim 2.5 \times 10^{19}$ m^{-3} [104]. TEMs are stabilized at higher n_e by reducing R/L_n and increasing ν_*, while decreasing Z_{eff} drives ETGs more unstable.

Global nonlinear electrostatic simulations of ion-scale turbulence in various NBI-heated NSTX plasmas have been performed using the global GTS code, which, excluding δB and electron-scales, often underpredicts Q_e^{exp}. In a strongly rotating L-mode, GTS finds Kelvin–Helmholtz (KH)/ITG turbulence at $0.6 < r/a < 0.8$, with $Q_i^{GTS} \sim Q_i^{exp}$, but Q_e^{exp} dominates and $Q_e^{GTS} \ll Q_e^{exp}$ [193]. In an NBI heated H-mode, $Q_i^{exp} \sim Q_i^{GTS} + Q_i^{NC}$ before and after an I_p ramp-down, with negligible ion-scale turbulence in the latter state [194], but with the larger Q_e^{exp} still underpredicted. Interesting results for an H-mode with steep density, temperature and rotation gradients at mid-radius, find dissipative TEMs (DTEMs) dominating over collisionless TEMs (CTEMs), as the longer wavelength DTEM is more robust to $\nu_{e,*}$ and γ_E [193, 195]. The DTEM turbulence saturates as a large-scale quasi-coherent eddy with few toroidal modes. While Γ^{GTS}, Q_i^{GTS} and χ_ϕ^{GTS} all compare favorably with experiment in $0.5 < r/a < 0.6$, $Q_e^{GTS} \sim Q_e^{exp}/4$.
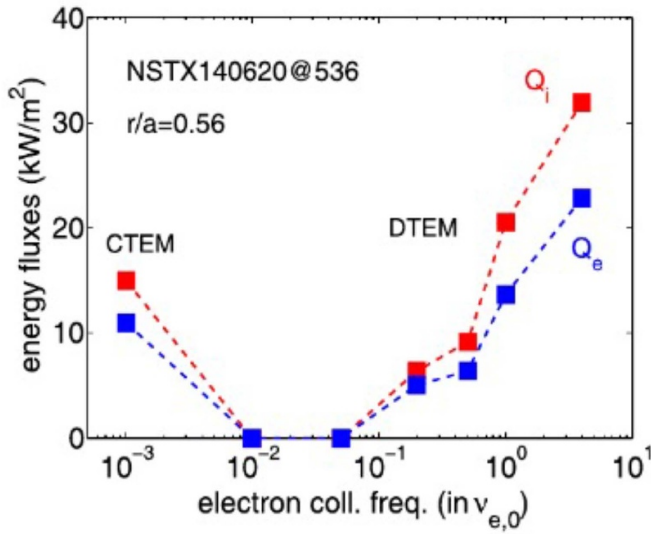
Figure 31. Simulated TEM-driven ion and electron heat fluxes for an NSTX equilibrium as functions of normalized electron collision frequency. Reprinted from [193], with the permission of AIP Publishing.

The fluxes have minima in $\nu_{e,*}$ at the CTEM-DTEM transition (see figure 31), which is suggested as a potential performance sweet spot for future STs [196]. Above the minimum $Q_{e,i}^{DTEM}$ increases with $\nu_{e,*}$ aligning qualitatively with the ST scaling $\tau_E \propto \nu_*^{-1}$ [108, 130].

Another global GK study for MAST using the ORB5 code (although with only adiabatic electrons and without $E_r \times B$ flow shear stabilization) allowed profiles to relax to a quasi-steady state to simulate MAST H and L-mode shots and met with some success [197].

There is broad support for flow shear suppression of turbulence in STs, where equilibrium flow shear often exceeds growth rates, particularly for ion-scale modes in plasmas with tangential NBI. Nonlinear GS2 simulations including γ_E, but neglecting Coriolis and centrifugal effects [171] at mid-radius in a MAST H-mode, find that toroidal flow shear can completely suppress ion-scale turbulence [198]. In toroidal equilibrium flows, $\mathbf{v}_\phi = R\Omega\,\hat{\mathbf{e}}_\phi$, is the sum of flows parallel and perpendicular to the equilibrium magnetic field, where $v_\parallel = \frac{B_T}{B}v_\phi$ and $v_\perp = \frac{B_P}{B}v_\phi$. The ratio of the the perpendicular component of the flow shear (which suppresses turbulence), $\gamma_E = \frac{dv_\perp}{dr}$, to the parallel component of the shear (which drives KH and parallel velocity gradient (PVG) turbulence [199]), $\gamma_p = \frac{dv_\parallel}{dr}$, is given by $\gamma_E/\gamma_p = B_P/B_T = q/\epsilon$. In ST geometry, B_P/B_T is large, which favors the suppression over the drive of turbulence by sheared toroidal equilibrium flows. Direct experimental evidence for flow shear suppression of ITG comes from NBI heated MAST L-modes, where local R/L_{Ti} measurements increase with increasing γ_E and decreasing q/ϵ [200]. An inverse correlation is also observed between R/L_{Ti} and the gyro-Bohm normalized ion heat flux estimated using beam emission spectroscopy (BES), Q_i^{BES}/Q^{gB}, indicating R/L_{Ti} is close to a critical threshold where $Q_i^{ITG} \sim Q_i^{NC}$ [200]. Theory

calculations of sub-critical PVG-ITG turbulence at zero magnetic shear [201–203] find that the weaker transient mode amplification factor $\propto e^{q/\epsilon}$ should make STs more resilient to such turbulence.

7.1.1. Ion-scale fluctuation measurements. Fluctuation measurements observe ion-scale turbulence outside ITBs in co-NBI MAST L-modes. Steep dT_i/dr and $d\omega_\phi/dr$ form at the ITB just inside q_{min}, where $\hat{s} < 0$. Negative magnetic shear, $\hat{s} < 0$, is found using GS2 to be sufficient to suppress all modes in the ITB, even neglecting γ_E [165]. Similar findings were reported for low $\hat{s}$ in a high β NSTX plasma [190]. Outside the ITB, where $\hat{s} > 0$ and γ_E is weaker, GS2 finds ITG modes resilient to flow shear that have growth rates boosted by kinetic electrons [165]. Global ORB5 simulations, with kinetic electrons and flow shear, confirm this and predict significant ITG turbulence outside the ITB [204]. ORB5 simulations find that flow shear stabilization is asymmetric with respect to the sign of γ_E owing to global effects, and that ITG turbulence spreads a short distance into the linearly stable region inside the barrier albeit impeded by stronger γ_E inside the ITB. BES measures ion-scale density fluctuations consistent with ITG turbulence at the edge of similar plasmas, and the measured correlation lengths, but not correlation times, are consistent with nonlinear ORB5 simulations [205]. Local GS2 simulations of the same plasma were post-processed using a synthetic diagnostic to reconstruct the BES data [206]; the simulations reproduced Q_i^{exp} but with significantly lower fluctuation amplitudes, and they found reasonable agreement with all measured turbulence correlation properties apart from the radial correlation length [207]. GS2 reveals that this turbulence is sub-critical, with R/L_{Ti} very close to threshold [208].

Ion-scale turbulence simulations scanning in R/L_T pass through the turbulence threshold and expose a transition between two distinct turbulent states [208]. Near threshold turbulence is dominated by sparse, long lived, spatially large structures with comparable amplitudes to fluctuations far above threshold that generate low levels of transport. As R/L_T increases above threshold the density of large-scale fluctuations rises, until they interact to break up into the more familiar sea of small, weak, volume-filling fluctuations causing higher transport (see figure 32). Close to threshold up-down symmetry is broken by flow shear induced tilting of the spatial correlation function, but symmetry is restored at high R/L_T [208]). This symmetry breaking tilt is observed experimentally in MAST BES measurements, suggesting ion scale turbulence is close to threshold [209]. The BES estimated normalized ion heat flux in MAST depends strongly on radial correlation length and tilt but is found to be insensitive to flow shear [210]. Significant poloidal velocity fluctuations, consistent with ion-scale zonal flows, are observed in velocimetry analysis of low-frequency filtered BES data (and in DBS), and may supplement equilibrium flow shear in generating the tilt [210].

Extensive analysis of BES ion-scale density fluctuation data from MAST L-mode, H-mode and ITB discharges reveals
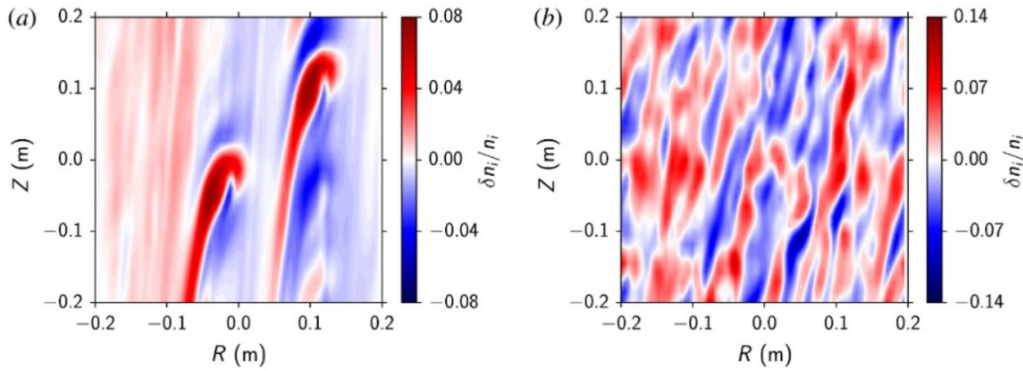
Figure 32. Normalized δn_e fluctuations in the poloidal plane (left) close to, and (right) well above the ITG threshold. Reproduced with permission of The Licensor through PLSclear from [208]. © Cambridge University Press 2016.

a 'grand critical balance' where times associated with fluctuation decorrelation, parallel streaming, diamagnetic drift, and magnetic drift are all comparable: $\tau_c \sim \tau_{st} \sim \tau_* \sim \tau_M$ [210, 211]. This demonstrates the turbulence is 3D and anisotropic with $L_\parallel > L_y > L_x$ where x, y are in the radial and binormal directions respectively. The measured turbulence correlation time is much shorter than an estimate of the nonlinear time based on measured drift wave fluctuations. Postulating that zonal flows (not measured directly by BES) decorrelate the turbulence instead, would require a ratio of zonal to drift wave amplitudes $|\delta\Phi_{ZF}|/|\delta\Phi_{DW}| \propto \nu_{*,i}^{-0.8}$, which is consistent with previous findings from [212].

7.2. MTMs at Ion and sub-ion binormal scales

MTMs generate magnetic islands on rational surfaces that tear confining flux surfaces and generate predominantly electron heat transport. They are driven by R/L_{Te} and propagate in the electron direction with frequency $\omega \sim \omega_{*,e}$. MTMs dominate over ITG at $k_y \rho_i < 1$ at mid-radius in MAST, NSTX and Globus-M H-mode plasmas where local $\beta_e \sim 5\%$ to 10% [179, 180, 213]. While MTMs were first found frequently to be dominant in STs, it is increasingly recognized that MTMs also impact on conventional aspect ratio tokamaks including in ITBs and in the H-mode pedestal [214, 215]. Local GK studies for the high performance phase in conceptual ST reactors [7, 216] indicate that MTMs and KBMs are likely to be the fastest growing modes, with MTMs dominant over an extended range of binormal scales and likely to have significant impacts on transport.

MTMs are less well understood than more familiar electrostatic (ETG, ITG, and TEM) and electromagnetic (KBM) modes, and so here we review what linear GK simulations have revealed about their properties. Microtearing eigenfunctions have a multiscale character: $\delta\Phi$ is highly extended in ballooning angle θ, which accommodates high radial wavenumbers, while $\delta A_\parallel$ is localized in θ and radially extended[4]. MTMs are unstable above critical thresholds in β and R/L_{Te}

[177, 217, 218], and other linear properties include: instability arising over a wide ν_e/ω range peaking at $\nu_e/\omega = O(1)$ [217, 218], γ^{MTM} sensitive to R/L_{Te}, ν_{ei}, R/L_n, β, R/L_p, and $\hat{s}$, γ^{MTM} is weakly sensitive to poloidal shaping [218], γ^{MTM} is insensitive to $\delta B_\parallel$, kinetic ions [177], and width of the perturbed current layer, $d = O(\rho_i)$ [217, 219]. Scans, using simplified circular $s - \alpha$ local equilibrium fits to MAST, reveal further properties of MTMs [217, 220]: magnetic drifts are destabilizing, trapped particles are destabilizing at low ν_{ei}/ω but they are stabilizing at high ν_{ei}/ω, the instability arises over a finite window in β (e.g. $0.05 < \beta < 0.35$), and MTMs are stable if both $\delta\Phi$ and magnetic drifts are excluded. The energy dependence in the collision operator is essential for MTM instability in most theories [221–225], but artificially removing this from GS2 was found to have weak/strong impact on γ^{MTM} when drifts are included/excluded [177, 217, 220].

MTMs are also unstable in the shallow gradient plateau inboard of the pedestal top in MAST [226, 227] and NSTX [228]. Edge MTMs exhibit most properties of core MTMs [217, 218], with two key differences: $\delta\Phi$ is less extended along the field line but still includes high k_r because of higher magnetic shear; and γ^{MTM}_{edge} can be maximal at $\nu_{ei} = 0$[5] (and not at finite ν_{ei} as in the core [217, 218]) indicating a collisionless drive [227, 228][6]. γ^{MTM}_{edge} increases strongly with trapped particle fraction, and figure 33 illustrates γ^{MTM}_{edge} dependence on ν_{ei} and inverse aspect ratio ε [227]. Electron drift, precession, and bounce frequencies are comparable to the mode frequency, challenging usual analytic theory approaches. The linear drive mechanism for MTMs is complex [217, 218, 227], and yet to be fully understood analytically.
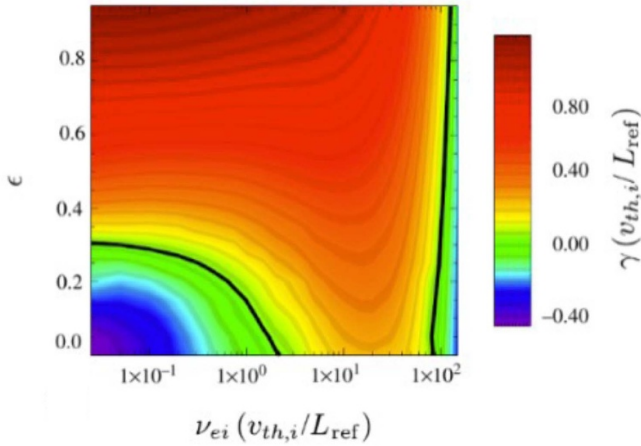
MTMs dominate at $r/a = 0.6$ in a collisional high β ($\beta_e \sim 10\%$) NSTX H-mode [108]. γ^{MTM} peaks for ν_{ei} in the range $1 < Z_{eff}\nu_{ei}/\omega < 4$, with the experimental $Z_{eff}\nu_{ei}$ typically below the peak where increasing Z_{eff} is destabilizing

---

[4] Recent local GK analysis for a high β conceptual ST reactor have exposed $A_\parallel$ eigenfunctions with an extended chain of narrow peaks in ballooning angle

[216]. The individual peaks in $A_\parallel$ are poloidally narrow and co-located (i.e. they are 2π apart in ballooning angle).

[5] NB The reduction of γ^{MTM} with decreasing ν_{ei} underpins core nonlinear simulations for neutral beam-heated NSTX plasmas finding $Q_e^{MTM} \sim \nu_{ei}$ [219], which aligns with the confinement scaling $B\tau_E \sim \nu_*^{-1}$ [108, 130].

[6] Collisionless MTMs are reported by several authors [229, 230], while other calculations find collisions essential for instability [231].

Figure 33. Growth rate of edge MTM versus ν_{ei} and inverse aspect ratio ε, for a circular $s-\alpha$ fit to the local equilibrium at the MAST pedestal top ($\epsilon^{1/2}$ sets the trapped particle fraction). The black line indicates marginal stability. Reprinted figure with permission from [226], Copyright (2012) by the American Physical Society.

[218]. γ^{MTM} dependencies on $\hat{s}$, q and $\hat{s}/q$ are non-monotonic; around the experimental value on this surface increasing $\hat{s}/q$ is destabilizing for $0.6 < \hat{s}/q < 1.3$, but becomes stabilizing for $\hat{s}/q > 2$ due to increased field-line-bending. Locally this results in γ^{MTM} and γ^{ETG} having opposite trends with Z_{eff} and $\hat{s}/q$, which may help distinguish modes experimentally. At $r/a > 0.8$, KBMs (or hybrid ITG/KBMs) at lower $k\rho_i \sim$ 0.15–0.35 become dominant over MTMs, especially at high $|R/L_n|$, β_e, and low $Z_{\text{eff}}\nu_{ei}$.

MTMs may play a role in the $\tau_E \propto \nu_*^{-1}$ scaling, which was verified over an extended ν_* range in NSTX using lithium wall conditioning, and is attributed to reduced Q_e at lower ν_* for $r/a > 0.5$ [120]. Local ν_* variation is large at $r/a = 0.6$: at high ν_* MTMs are virulent with $\gamma^{MTM} \gg \gamma_E$; at lower ν_*, γ^{MTM} is reduced with $\gamma^{MTM} \sim \gamma_E$. Farther out at $r/a = 0.7$, the hybrid TEM/KBM is unstable over a wider radial range at lower ν_* due to an increase in T_e/T_i, though its influence on Q_i is unclear, as $\gamma^{KBM-TEM} \sim \gamma_E$. NSTX and MAST collisionality scans were performed with ν_{ei} below the peak in $\gamma^{MTM}(\nu_{ei})$, where growth rates align with $\tau_E \propto \nu_*^{-1}$ scaling [130, 218]. The weaker scaling $\tau_E \propto \nu_*^{-0.4}$ at the lower B_T of Globus-M (see equation (18)) may be explained by ν_{ei} in the scan ranging above the peak in $\gamma^{MTM}(\nu_{ei})$.

Higher wavenumber MTMs are robustly unstable at $3 < k_y\rho_i < 15$ in the core of HHFW heated NSTX L-modes, where $q_0 \sim 3$ is higher than in typical H-modes, $\hat{s}$ is low, and core values of $\beta_e \sim 5\%$ [232]. (Similar MTMs also dominate sub-ρ_i-scales at mid-radius in a conceptual burning ST [7]). While $\delta\Phi$ eigenfunctions are less extended in ballooning angle than for core MTMs [180, 218], radial wavenumbers are similar as $k_y\rho_i$ is higher [232]. γ^{MTM} increases with R/L_{Te} and ν_{ei}, and is higher in D^+ than in He^{2+} plasmas [232]. At outer radii, MTMs are stable at lower β_e and ETG is the dominant instability.

First estimates of MTM transport were for a beam heated NSTX H-mode with $P_{NBI} = 6$ MW [233], where MTMs at $0.1 < k_y\rho_i < 1$ dominate in the steep dT_e/dr region at $0.4 < r/a < 0.75$ [233]. Nonlinear MTM theory predicts magnetic fluctuations scale as $\delta B/B \sim \rho_e/L_{Te}$ [234], suggesting large $\delta B/B$ in low B machines (as is typical in STs). MTMs saturate nonlinearly to form overlapping islands centered on different rational surfaces, and electron heat transport can be estimated using a simple test-particle transport model from stochastic magnetic fields [235]. In the collisional limit (valid for this plasma), this gives a model heat diffusivity, $\chi_e^{MTM} = (\rho_e/L_T)^2 \, v_{th,e}^2/(\nu_{ei}q)$ that predicts substantial transport at mid-radius with $\chi_e^{MTM} \sim 0.5\chi_e^{exp}$ [233]. If this model dominated heat loss, the associated energy confinement time scaling would be consistent with $\tau_E \sim a^2/\chi_e \propto B$ reported for STs [130, 131]. Another electron heat transport mechanism is required for $r/a < 0.3$, where T_e is too flat to drive MTMs. In NSTX discharges with core $\hat{s} < 0$, however, core confinement improves with the suppression of MTMs and χ_e [233].

Nonlinear local GYRO calculations [219, 236] were performed at $r/a = 0.6$ in the MTM dominated collisional high β NSTX H-mode, studied linearly in [219] as discussed above, where ETG was found to be stable. The calculations included kinetic electrons and ions as well as electron pitch angle scattering, but neglected γ_E. Nonlinear MTM simulations are challenging because of the need to capture both the rational surface spacing and fine radial scales in $\delta\Phi$ [7]. Grids used ≤ 16 binormal wavenumbers $0 < k_\theta\rho_s < 0.75$, and ≤ 540 points in a radial domain extending $80\rho_s$. In the saturated state, shown in figure 34, δn_e fluctuations peak off the outboard mid-plane and have correlation lengths $L_x \sim 0.7\rho_s \ll L_y \sim 4\rho_s$, while $\delta A_\parallel$ approaches the box scale radially and peaks at the lowest resolved finite $k_\theta\rho_s$. Simulations find $\delta B_r/B \sim \rho_e/L_{Te}$, consistent with nonlinear MTM theory [234]. Magnetic flutter carries $\sim 98\%$ of the heat flux and $Q_e \gg Q_i$. $\chi_e^{sim} \sim 1.2\chi_e^{gB}$ is consistent with χ_e^{exp}, and with a collisionless Rechester–Rosenbluth estimate [235] following [233] giving $\chi_e^{mod} \sim 0.92 \, \chi_e^{gB}$. Scans in this parameter range (see figure 35) find that χ_e/χ_e^{gB} scales almost linearly with ν_*, and it increases sharply with both R/L_{Te} and with β_e above critical values that exceed linear thresholds. Restarting a saturated simulation with the experimental γ_E, however, largely suppressed the MTM turbulence, although artificially increasing R/L_{Te} by 20% partly restored Q_e^{MTM} to a level approximately three times smaller than Q_e^{exp} [219].

7.3. Electron scales: ETG modes

ETG modes, the electron-scale analogue of ITG, can produce substantial electron heat transport with $\chi_e \gg \chi_e^{gB}$ [237, 238], and are unstable for $R/L_{Te} > R/L_{Te,crit}^{ETG}$. Linear local GK

---

[7] First attempts at nonlinear MTM simulations for MAST using GS2 failed to saturate due to unexplained nonlinear instability of the highest k_x modes on the grid [188, 220].
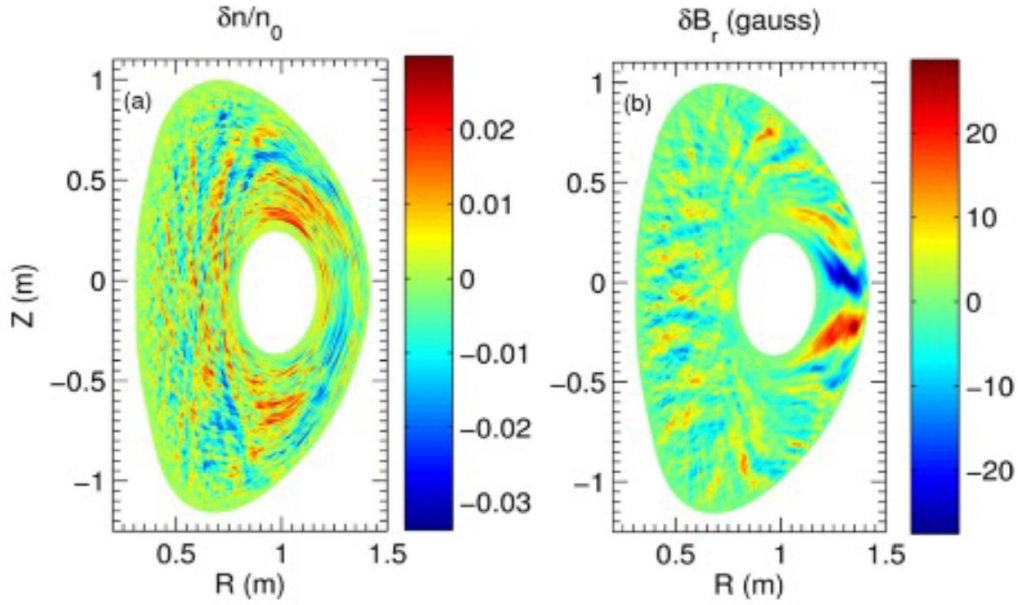
Figure 34. Contour plot of (a) δn_e and (b) δB_r in the poloidal plane from the saturated state of local nonlinear MTM simulations for NSTX. Reprinted from [219], with the permission of AIP Publishing.
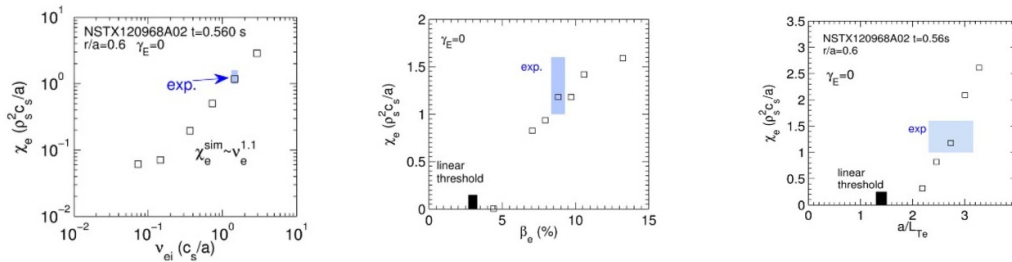
Figure 35. χ_e^{exp} and χ_e from nonlinear GYRO simulations of MTM turbulence in NSTX, showing dependencies on: (left) ν_{ei}, (middle) β_e, and (right) a/L_{Te}. $\chi_e \propto \nu_{ei}^{1.1}$, and linearly increases with β_e in this region of parameter space, but over a more extended region the dependence is non-monotonic and χ_e rolls over to decrease at higher ν_{ei} or β_e. Reprinted from [219], with the permission of AIP Publishing.

simulations have been used to obtain an approximate formula for the ETG threshold for typical core conditions [192]:

$$
\frac{R}{L_{Te,crit}^{ETG}} = Max\left[\left(1 + \frac{Z_{\text{eff}}T_e}{T_i}\right)\left(1.33 + 1.91\frac{\hat{s}}{q}\right)(1 - 1.5\epsilon) \right.
$$
$$
\left. \times \left(1 + 0.3\epsilon\frac{d\kappa}{d\epsilon}\right), 0.8R/L_n \right]. \quad (21)
$$

This formula captures the stabilizing impacts of impurities (demonstrated for MAST [239]), $\hat{s}/q$, and density gradients, but is not expected to be accurate at high β, high dp/dr, $\hat{s} \leqslant 0$, or with strong shaping. ETG is sensitive to finite β effects particularly from $\delta B_\parallel$ [175, 240, 241], and both $\delta B_\parallel$ and full magnetic drift velocity $v_{\nabla B}$ must be retained [241]: the low $k_\perp \rho_i$ approximation canceling the $\delta B_\parallel$ drive with the dp/dr contribution to $v_{\nabla B}$ [242], is inaccurate for ETG even at $\beta \ll 1$ [241]. In strongly rotating beam heated

STs, virulent ETG modes well above threshold (i.e. $R/L_{Te} \gg R/L_{Te,crit}^{ETG}$) are less susceptible to flow shear suppression than ITG, because $\gamma^{ETG} \gg \gamma_E$ while $\gamma^{ITG} \sim \gamma_E$. GK simulations and experimental data reveal regimes where ETG carries significant Q_e in mid/outer radius regions of MAST and NSTX.

In MAST H-modes, at mid-radius where density is flat and $\beta \sim 0.1$, GS2 finds $\gamma^{ETG} \gg \gamma_E$ with peak growth around $k_y\rho_e \sim 0.2$–0.3 [180], in conditions where including $\delta B_\parallel$ reduces γ^{ETG} [177]. Collisions have little influence on γ^{ETG} at high wavenumber where $\nu_{ei}/(\epsilon\omega) \ll 1$ [243, 244], but at lower k_y, collisional detrapping when $\nu_{ei}/(\epsilon\omega) > 1$ reduces the linear drive [198, 244]. In NSTX H-modes, perturbative Li pellet experiments find stiff T_e profiles in monotonic q plasmas consistent with a critical R/L_{Te} [108], χ_e profile shapes agree with an analytic electrostatic model of ETG transport [108, 245], and at $r/a = 0.65$ $\chi_e \sim 5$–20 χ_e^{gB}, as expected from ETG turbulence. ETG may also play a role in discharges from an NSTX ν_* scan outside mid-radius, where $R/L_{Te} >$
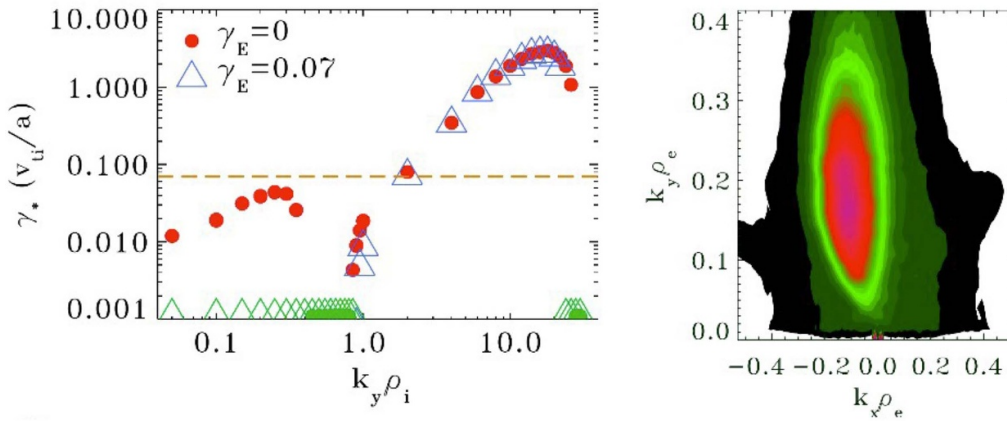
Figure 36. (left) Effective growth rates as functions of $k_y\rho_i$ with (triangles) and without (circles), γ_E^{exp} indicated by horizontal dashed line, at mid-radius in a MAST H-mode, demonstrating the suppression of ion scale modes. Symbols at the γ_*-axis minimum denote stable modes. (right) Fieldline averaged saturated spectrum of $\delta\Phi^2(k_x, k_y)$ for an ETG simulation with $\gamma_E = 4\,\gamma_E^{exp}$, demonstrating anisotropy and γ_E induced eddy tilting. Reproduced from [198]. © IOP Publishing Ltd. All rights reserved.

$R/L_{Te,crit}^{ETG}$ [120] and GYRO finds γ^{ETG} and R/L_{Te} decreasing with decreasing ν_* [120].

Single scale nonlinear ETG simulations are physically justified if there is a mechanism to provide a low-k_y cut-off by suppressing ion-scales. First nonlinear electromagnetic simulations of ETG turbulence for a MAST H-mode used GS2 at $r/a = 0.4$, where $\beta_e \sim 0.049$ and $R/L_n \sim 0$ [246]. Calculations with/without collisions, with/without kinetic ions, with various grid resolutions and neglecting flow shear found electrostatic transport dominating negligible magnetic flutter transport in the saturated state, with $\chi_e^{ETG} \sim \chi_e^{exp} \gg \chi_e^{gB}$. The excess over χ_e^{gB} is due to strong streamers (with $k_y \gg k_x$) and weak zonal modes, and Q_e depends weakly on β_e in spite of $\delta B_\parallel$ reducing γ^{ETG} [198, 241, 247]. Farther out at $r/a = 0.8$, $\hat{s}/q$ and R/L_n are larger and $\chi_e^{ETG} \ll \chi_e^{exp}$. Later electrostatic GS2 simulations for the same local equilibrium, included flow shear and collisions that each individually suppress low k_y [198]. These calculations confirm that anisotropic ETG turbulence with $k_y \gg k_x$ gives $Q_e^{ETG} \sim Q_e^{exp}$ and is robust to the experimental level of γ_E (see figure 36). ETG turbulence could, however, be suppressed by artificially increasing γ_E to $10 \times \gamma_E^{exp} = O(\gamma^{ETG})$ [198]. These findings were verified using GYRO (with non-periodic boundary conditions) [198, 248], where it was also noted that the anisotropic nature of ETG turbulence must be carefully accounted for on interpreting fluctuation measurements (e.g. from the NSTX high-k scattering system that is sensitive to modes with $k_r = 9\,k_\theta$ [248]).

Low-β NSTX H-mode plasmas in a scan with normalized electron collisionality $\nu_{e,*}$ spanning a factor 2.5, exhibited the energy confinement scaling, $B\tau_E \propto \nu_{e,*}^{-0.82}$ [243] consistent with a scan at higher β [108]. ETG is unstable (with MTMs stable) at the high-k scattering location near mid-radius where $\beta_e \sim 0.02$. High-k fluctuations, however, increase at lower ν_* counter to expectation from the τ_E scaling, which is not fully understood and could be a local effect [243].

Global electrostatic simulations of NSTX, using GTS with adiabatic ions find ETG turbulence dominated by anisotropic

streamers making significant contributions to electron heat transport [193]. Turbulence saturation involves an initial transient dominated by ETG streamers at $k_\theta\rho_s \sim 13$, subsequent transfer of energy to a high frequency e-GAM at $m = 1$, and downshift of the streamer spectrum to $k_\theta\rho_s \sim 6$ with concurrent slow growth of a low frequency zonal flow. It was speculated that collisional damping of zonal flows and e-GAMs, could indirectly lead to a favorable scaling $Q_e^{ETG} \propto \nu_*$ following a similar mechanism reported for ITG [212]. GTS also computed ETG turbulence in an RF-only L-mode before and after switching-off the RF heating, which resulted in a rapid reduction of electron-scale fluctuations and Q_e^{exp} dropping by a factor 2 [249]. Equilibrium gradients and the simulated electron heat flux, Q_e^{GTS}, were, however, similar before and after cessation, and only close to Q_e^{exp} in the latter state without RF; the discrepancy is not understood.

The collisionality dependence of ETG turbulence was explored at mid-radius in MAST using GS2. Artificially scanning ν_{ei} at fixed R/L_{Te} reveals that the saturated Q_e falls with decreasing ν_*, due to an evolving balance between zonal and non-zonal fluctuations [244]. At low ν_{ei}, long computation times, $tv_{th,e}/a = O(10\,000)$, were needed to reach the transport relevant saturated state. At low ν_{ei}, resistive collisional damping is weak, and zonal modes grow sufficiently large to break up the transport enhancing radial streamers that form early in the simulation. ETG turbulence is marginal in these simulations, and the saturation process differs from the standard picture developed in the strongly driven limit where zonal secondaries are weak [237]. The simulations find $Q_e^{ETG} \sim \nu_{ei}$ (see figure 37), consistent with a theoretical model of interactions between resistively damped zonal modes, drift waves and linear drive [244]. This Q_e^{ETG} scaling aligns with the energy confinement scaling obtained from H-modes in NSTX and MAST, $B\tau_E \propto \nu_*^{-1}$ [108, 130].

Electron internal transport barriers (e-ITBs) were produced on NSTX at locations with $\hat{s} < -0.4$ with $\chi_e < 0.1\,\chi_e^{gB}$ and $R/L_{Te} \sim 20 \gg R/L_{Te,crit}^{ETG}$ (see figure 38). High-k fluctuation measurements suggest local suppression of ETG turbulence in
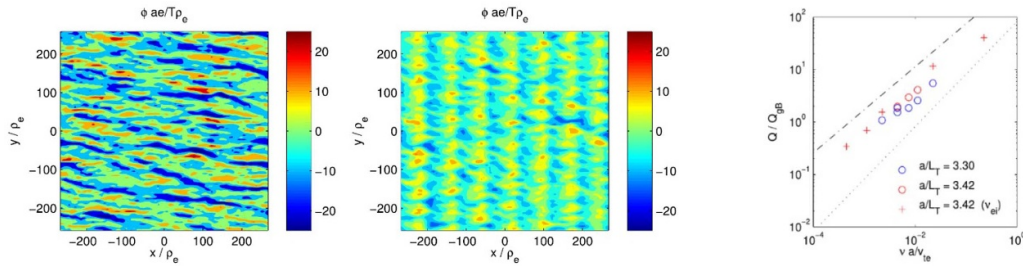
Figure 37. Normalized electrostatic potential at outboard midplane from GS2 simulation of ETG turbulence in MAST-like parameters at $\nu = 0.2\,\nu^{exp}$ (left) pseudo-saturated state dominated by streamers at $t = 1200a/v_{th,e}$, (middle) long-time saturated state at $t = 7835a/v_{th,e}$ with lower transport because zonal flows have broken up the streamers, (right) normalized electron heat flux from ETG turbulence has linear dependence on collisionality for several values of R/L_{Te}. Reproduced from [244]. © 2017 EUROfusion University of Oxford.
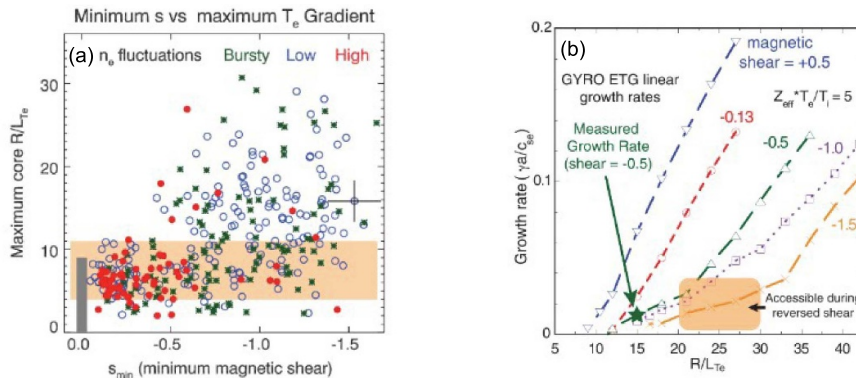
Figure 38. Plots from study of e-ITB plasmas in NSTX. (a) Maximum core R/L_{Te} versus minimum magnetic shear, showing improved access to extremely high R/L_{Te} and suppression of high-k fluctuations at increasingly negative $\hat{s}$. (b) Linear GYRO results showing ETG growth rates reducing with increasingly negative $\hat{s}$, but without any significant change to $R/L_{Te,crit}^{ETG}$. Reprinted figure with permission from [168], Copyright (2011) by the American Physical Society.

the e-ITB [167, 168], while paradoxically linear GKs finds this region should be super-critically unstable to ETG (robust to the uncertainty in Z_{eff}). Strong negative $\hat{s}$ is the key ingredient for triggering e-ITB formation and the transition from stiff to weak ETG transport. Flow shear is thought not to be responsible, as barriers can be generated in HHFW heated plasmas where $\gamma_E \sim 0$. During the lifetime of the e-ITB, intermittent bursts of high-k fluctuations grow on timescales consistent with ETG and may regulate R/L_{Te} inside the barrier. Nonlinear electrostatic local GYRO simulations [168] for an RF heated NSTX e-ITB with negligible γ_E, found significant ETG turbulence only for $R/L_{Te} \gg R/L_{Te,crit}^{ETG}$, and that the upshift in R/L_{Te} needed to access the nonlinear threshold gets larger as $\hat{s}$ becomes more negative (see figure 39(a)). Above the nonlinear critical threshold the turbulence character changes, with off-mid-plane streamers at the top and bottom of the e-ITB flux surfaces (see figure 39(b)). Global GYRO calculations find that ETG driven heat flux is comparable with experiment in the outer region of the barrier where $\hat{s}$ is less negative, and that the turbulence cannot penetrate to the inner barrier where $\hat{s}$ is more negative and $Z_{eff}T_e/T_i$ is larger. It was recently shown in [250] that at strong R/L_{Te}, ETG fluctuations with $k_x \gg k_y$ and peak amplitudes at the top and bottom of the flux surface can be linearly unstable, consistent with figure 39(b).

7.3.1. Electron-scale fluctuation measurements. High-k microwave scattering observations provide direct support for R/L_{Te} driven fluctuations consistent with ETG turbulence in NSTX He plasmas heated by HHFW, where the fluctuations strikingly appear when $R/L_{Te} > R/L_{Te,crit}^{ETG}$ and it is found that equation (21) only slightly underestimates the critical gradient computed using GS2 [251, 252]. Flow shear suppression of ETG turbulence is possible near marginal stability and has been observed under such conditions in high-k scattering observations from NSTX [253].

Density gradient stabilization of ETG was first observed on NSTX after an ELM increased R/L_n locally by a factor of 5, while χ_e halved and high-k scattering found suppression of ETG density fluctuations at $k_\perp \rho_s < 10$ consistent with linear GS2 [243, 254]. Later in a slowly evolving NBI heated NSTX H-mode with R/L_n increasing at the high-k scattering location, the fluctuations moved to lower amplitudes and frequencies in the plasma frame, supporting the stabilizing influence of R/L_n on ETG [255].

Electron-scale δn_e fluctuations were measured in the core of a MAST L-mode using DBS, sensitive to modes with $k_y \gg k_r$ (c.f. $k_y \ll k_r$ from NSTX high-k scattering). First results reveal that for $7 < k_\perp \rho_i < 11$, $|\delta n|^2 \sim k_\perp^{-\alpha}$, $\alpha = 4.7 \pm 0.2$ [256], where the exponent is close
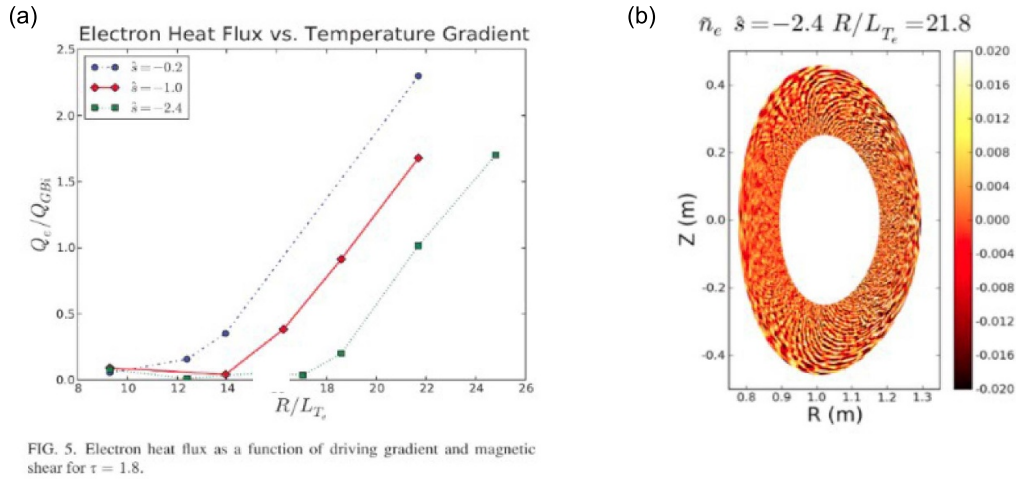
FIG. 5. Electron heat flux as a function of driving gradient and magnetic shear for $\tau = 1.8$.

Figure 39. (a) ETG electron heat flux versus R/L_{Te} for different values of $\hat{s}$ inside an NSTX e-ITB. The nonlinear threshold gradient is increasingly upshifted beyond the linear threshold as $\hat{s}$ gets more negative. (b) Density fluctuations in poloidal cross section from a local GYRO calculation of ETG turbulence at R/L_{Te} above the nonlinear threshold, showing high amplitude fluctuations giving significant electron heat transport at the top and bottom of the flux surface. Reprinted from [167], with the permission of AIP Publishing.
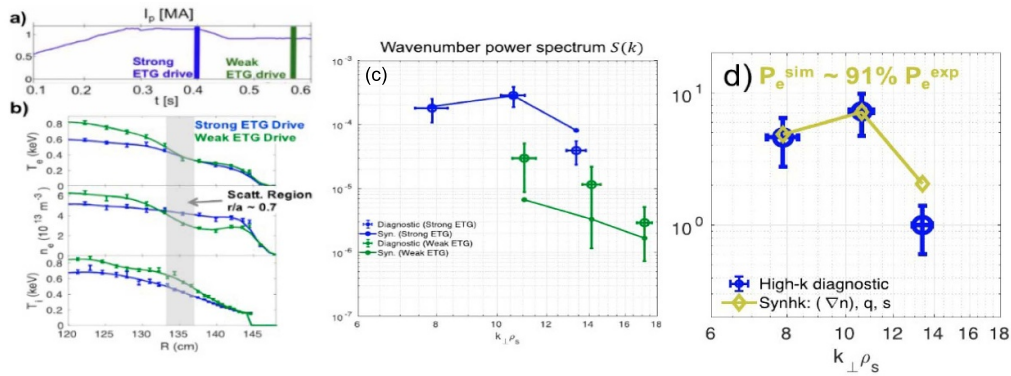
Figure 40. (a) I_p time trace from NBI heated NSTX H-mode at modest β, indicating two times when ETG drive is strong and weak. (b) Radial profiles of T_e, n_e and T_i at these times. (c) Comparisons of fluctuation spectra from the high-k scattering diagnostic at $r/a = 0.7$ (open circles with error bars), with synthetic diagnostic spectra from nonlinear GYRO simulations of ETG turbulence (solid points connected by line). Blue and green correspond to times with high and low ETG drive, respectively. (d) Experimental and synthetic wavenumber spectral shape match well for the strong ETG condition where the ETG GYRO simulation used R/L_n optimized to within $R/L_n^{exp} \pm 1\sigma$, $q = 0.9q^{exp}$, and $\hat{s} = 1.2\hat{s}^{exp}$. In (c) and (d) the diagnostic spectra were scaled by a constant which was chosen to minimize 'distance' from the synthetic spectrum for the strongly driven case. Reproduced from [258]. © IOP Publishing Ltd. All rights reserved.

to 13/3 as expected from a theory-based power law [257].

Compelling evidence for transport relevant ETG turbulence comes from an extensive validation study using the NSTX high-k scattering system during an I_p ramp-down in a moderate β NBI-heated discharge [258]. R/L_n increases by a factor four between two times at the high-k scattering location, $r/a = 0.7$, where fluctuations reduce in amplitude (see figure 40). Improving on earlier work [255], fluctuation measurements were compared with synthetic diagnostics based on local nonlinear GYRO simulations at both times. These demonstrate impressive simultaneous agreement for Q_e, fluctuation frequency spectra (which poorly discriminate between models), fluctuation wavenumber spectral shape, and the ratio of fluctuation levels in strongly and weakly driven conditions (see figure 40). This strongly supports electron thermal transport

being caused by electron-scale ETG turbulence at the outer-core of this moderate β H-mode plasma, in conditions of both strong and weak ETG drive [258].

7.4. Holistic microstability analysis for select regimes

7.4.1. Edge pedestal. The transition between the shallow gradient core and the steep H-mode pedestal, triggers a sharp change in microstability in a relatively collisional MAST H-mode pedestal, with modest bootstrap current and dn_e/dr dominating dp/dr [226, 259]. In the steep pedestal KBMs dominate at $k_\perp \rho_i < 1$ (close to marginal), but MTMs and ETG at higher k_y [256] dominate the shallower plateau inboard of the pedestal top. This stark mode transition is triggered by an increasing pedestal density gradient post-ELM (see figure 41(c)) and contributes to the pedestal recovery [226].
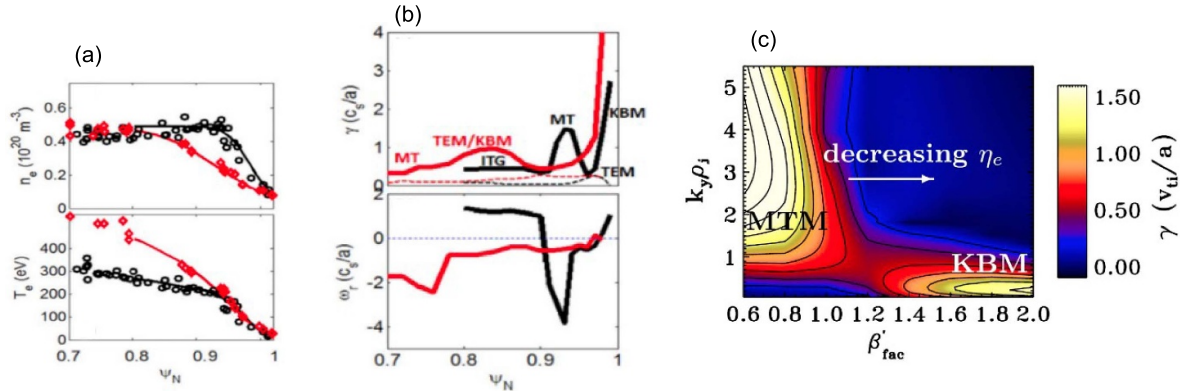
Figure 41. (a) n_e (top) and T_e (bottom) profiles from NSTX discharges with (red) and without (black) 5355 mg Li coating applied to PFCs prior to the discharge. (Reproduced with permission from Canik *et al* [228]). (b) Growth rates and frequencies of the dominant microinstability at $k_\theta \rho_s \leqslant 1$ as a function of normalized poloidal flux for NSTX equilibria shown (left) with (red) and without (black) Li conditioning shown in (a). (c) Contour plot showing growth rate of dominant modes as a function of $k_y \rho_i$ from a scan around the local MAST equilibrium of a surface that joins the expanding pedestal during ELM recovery. In the scan dn_e/dr and R/L_n are multiplied by a factor β'_{fac}, which closely represents the measured pedestal profile evolution, and dominant MTMs are supplanted by KBMs on joining the pedestal. Reprinted figure with permission from [226], Copyright (2012) by the American Physical Society.

Similar results are found at comparable but slightly higher collisonality in non-Li H-mode pedestals in NSTX [228, 260] (see figure 41(b)), where ETG is also unstable from mid-pedestal outwards. The MTM-KBM mode transition is also seen at the pedestal top of a lower ν_* MAST H-mode pedestal, but mid-pedestal enhanced bootstrap current gives KBMs access to second stability [261]. DBS and cross-polarization DBS (CP-DBS) in MAST have measured δn and δB fluctuations at the pedestal top during the ELM recovery in type-I ELMs. Linear GK calculations find that ETG dominates, with MTM also unstable at the location and wavenumbers $3 < k_\perp \rho_i < 4$ measured by DBS/CP-DBS. The measured $(\delta B/B)/(\delta n/n) \sim 0.05$ is closer to the value 0.02 expected linearly from ETG than 0.4 for MTMs.

ETG transport is also believed to be important in H-mode pedestals of conventional aspect ratio devices. In JET H-modes with higher levels of gas fueling, confinement is degraded; this is associated with lower R/L_n, and higher $\eta_e = L_{Te}/L_n$ in the pedestal [262], which enhances ETG driven electron heat transport [250]. It was also recently reported that ETGs make significant contributions to pedestal heat transport in DIII-D [263].

7.4.2. Impact of lithium. Li coatings applied to PFCs in NSTX reduce edge recycling, improve confinement [228] and substantially change profiles (see figure 41(a)). The density pedestal is broader but shallower with Li, and inside Ψ_{95}, dT_e/dr is steeper and χ_e is lower. Radial profiles of the dominant microinstabilities at $k_\theta \rho_s < 1$ (illustrated in figure 41(b)) are quite different with and without Li. Without Li, MTMs dominate at a conventional pedestal top, but with Li MTMs are stabilized by higher dn_e/dr and are replaced by hybrid TEM/KBM modes with lower growth rates comparable to γ_E. MTM growth rates at the pedestal top are insensitive to large reductions in ν_e, as seen in MAST [227]. Outside Ψ_{95} both

cases are unstable to ETG modes, but lower R/L_n with Li results in more virulent ETG that may limit dT_e/dr. In both plasmas the pedestal is close to the KBM stability boundary but in second-stability where growth rates decrease with increasing pressure gradient.

7.4.3. Pellet fueling. Local microstability was analyzed in edge pellet fueled MAST H-modes, on three surfaces close to the pellet ablation peak during 10 ms following pellet launch [187]. Microstability was strongly impacted by large local equilibrium excursions induced by the pellet. The most striking feature is an asymmetry between the stabilizing and destabilizing impacts of the pellet on TEMs, inside and outside the ablation peak, which arises because of favorable and unfavorable drifts respectively at these locations, and could result in more pellet particles being transported outwards than into the core. On the surface with $dn/dr > 0$, the favorable/unfavorable drift regions are inverted from the usual situation. On this surface, the drifts are favorable at $\theta = 0$ (outboard side), and unfavorable at $\theta = \pi$. Without collisions CTEMs would be unstable at $\theta = \pi$, but CTEMs are stabilized by the level of collisions in this MAST plasma.

7.4.4. Enhanced electron heat transport/anomalous fast ion redistribution at high power. At high NBI heating power, P_{NBI}, NSTX H-modes have flat core T_e, which is correlated with large amplitude GAEs and CAEs (see figure 42(a)). If the P_{NBI} source is classically transferred to the plasma, the core electron heat transport is very hard to explain because gradients of the thermal species are too low to drive microturbulence [124]. One possibility is that core Q_e is enhanced by stochastic electron orbits generated by multiple overlapping GAEs [124, 264]. Alternatively CAEs and GAEs could couple to kinetic Alfven waves (KAWs) and convey the NBI energy and momentum sources to a resonance at larger radius where
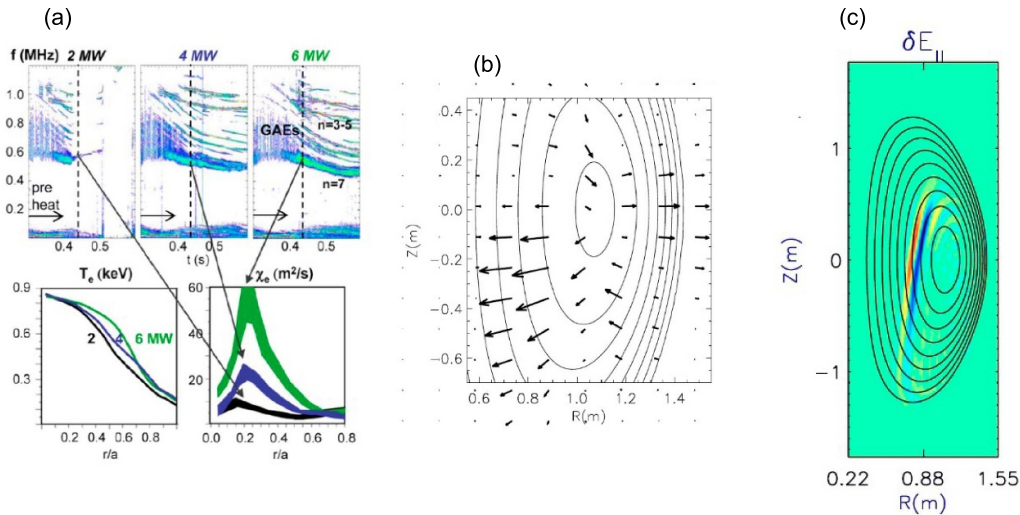
Figure 42. (a) Correlation between GAE activity (top), T_e flattening (bottom left), and increasing core χ_e (bottom right) with increasing beam power (Reprinted figure 3 with permission from: Stutman *et al*, Phys. Rev. Lett., 102, 115 002, 2009. Copyright 2009 by the American Physical Society.). Alternatively results from nonlinear hybrid MHD-particle simulations illustrated in (b) and (c) suggest redistribution of the fast ion heating profile off-axis by 'energy channelling' due to interactions between GAE and KAW. (b) Simulations for $n = 4$ modes show an outward flux of fast ion energy arising from the coupling of core driven GAEs to KAWs driven at an off-axis resonance. (c) Contour plot of $\delta E_\parallel$ (from the same simulation) shows the off-axis resonance location where plasma electrons are heated by the KAW. (b) and (c) reprinted from [266], with the permission of AIP Publishing.

they are transferred to the thermal plasma, in a process called 'energy channeling' [265] (see figures 42(b) and (c)) . Nonlinear hybrid MHD-particle simulations find that energy channeling involving CAEs coupling to KAWs, appears the more plausible explanation [266]. Novel reflectometry of GAEs and CAEs in similar discharges, however, find amplitudes that are too low to support either mechanism, and also rule out significant stochastic ion heating from CAEs [267]. Experiments at higher B_T and using flexible NBI configurations on NSTX-U will impact fast particle modes and should help address this question. GAEs on NSTX-U have already been observed at higher frequency and toroidal mode number than on NSTX, and they are found to be suppressed by higher pitch beam ions injected by off-axis NBI [268], consistent with theory and hybrid MHD-particle simulations [269].

7.4.5. Long steady discharges. Long steady discharges that will be delivered by NSTX-U and MAST-U are ideal for confinement studies. Initial transport studies on NSTX-U for a long pulse L-mode with $P_{NBI} = 2.6$ MW, $\langle n_e \rangle = 4.3 \times 10^{19}$ m^{-3} and $\beta_T = 4.1\%$ show that $\chi_e \gg \chi_i$ and $\chi_i \sim \chi_i^{NC}$ at $0.2 < r/a < 0.8$ [184], which is consistent with local GYRO calculations in $0.45 < r/a < 0.7$, where ITG turbulence is either stable or weakly growing with $\gamma^{ITG} \ll \gamma_E$. At $r/a = 0.47$, β and Z_{eff} may be sufficiently large to trigger a dominant electron heat transport contribution from Q_e^{MTM} with $\gamma^{MTM} > \gamma_E$. Electron-scale nonlinear ETG calculations predict large contributions from Q_e^{ETG} at $r/a = 0.47, 0.56, 0.66$. Farther out at $r/a = 0.76$, however, ETG is diminished and ITG dominates transport because γ_E is lower and decreasing with radius. This is consistent with BES finding broadband ion-scale fluctuations growing with radius. Interestingly BES finds bi-modal

poloidal phase velocities at $r/a \sim 0.68$ that could indicate the presence of two types of mode at ion scales, but these were not found in nonlinear GK simulations. These NSTX-U plasmas have complicated microturbulence at both electron and ion scales that exhibit strong radial dependence, and more sophisticated calculations including non-local profile variation, δB, and multi-scale interactions may be needed [184].

8. Reduced transport modeling

Transport modeling predictions, using reduced models that are either phenomenological or physics-based, have been compared against data from a modest number of ST discharges. Early transport simulations for Ohmic discharges on START tested ion neoclassical transport expressions and four models of anomalous electron heat transport that combine theory and phenomenological elements [270]. T_i profiles could be predicted quite well when low aspect ratio corrections [270] were implemented in the Chang–Hinton expression for χ_i^{NC} [271, 272], and the measured T_e profiles were also reasonably consistent with predictions from several models of anomalous electron heat transport: Rebut–Lallia–Watkins (RLW) [273] (representing electron heat transport from MTMs), Lackner–Gottardi [274], and the T11 model [275]. Taroni's Bohm model [276], however, overestimated T_e by an order-of-magnitude. The phenomenological canonical profiles transport model (CPTM), based on self-consistent pressure profiles, has modeled T_e, T_i and n_e profiles reasonably well in the gradient zone of Ohmic and NB-heated discharges in MAST [277]. CPTM was subsequently extended to describe a pedestal, and applied to ELMy and ELM-free H-mode discharges in both MAST and JET. The predicted temperature profiles

were found to be insensitive to the heating profile, density profile peaking was predicted at low collisionality, the predicted pedestal temperature increased with I_p, and low temperature pedestals were predicted in MAST H-modes [278]. A further CPTM extension to include toroidal rotation (calibrated using ELMy H-mode and hybrid discharges from JET) was also applied to MAST, where it gave reasonable predictions of toroidal rotation [279].

Transport predictions for NSTX H-mode discharges were obtained using several reduced models that target or include MTM heat transport. Wong *et al* [280] applied the Drake theory [234] of saturated MTM mode amplitude to determine the associated electron thermal diffusivity appropriate to the resulting stochastic magnetic fields. Wong *et al* estimated the MTM island width from the linear mode structure as calculated by GS2, and the magnetic field perturbation saturated amplitude from $\delta B/B \approx \rho_e/L_T$. The Drake theory was developed for a shearless slab and was not tested for ST geometry, but nevertheless its prediction for χ_e is within a factor of two of the inferred experimental χ_e for $r/a \geqslant 0.45$.

The RLW model was also tested on NSTX H-modes. RLW gave reasonable matches to T_e^{exp} at radii and times where GK calculations found unstable MTMs [281]. Since RLW is independent of ν_* and β, it did not capture transport dependencies across the range of these parameters in the NSTX experiments, and thus gave poorer agreement especially at the lower collisionalities and where the GK calculations find that MTM is stable. The multi-mode transport model (MMM) was recently upgraded to include MTMs, which improved T_e predictions for a high ν_* NSTX plasma [282]. The growth rates as a function of collisionality of the MTM transport component of this model were validated against linear GK simulations. Transport predictions from this reduced model agree well with NSTX experimental T_e profiles at high collisionality, but further development of the model is needed to capture accurately the experimentally observed dependence across the full range of collisionality.

Early attempts at more physics-based transport modeling for STs tested TGLF [283] against discharges from MAST and NSTX [176]. These simulations included ion neoclassical transport and used TGLF for anomalous transport in the radial zone where $q > 1$ and $\rho < 0.82$. (Data from two of the MAST discharges, including the most suitable discharge for transport modeling which was an H-mode with $q > 1$ throughout the plasma, are available in the ITPA tokamak profile database [284].) Ion neoclassical transport was found to dominate the ion heat channel, and T_i measurements were consistent with transport predictions using the Chang–Hinton formula for χ_i^{NC} [271, 272] if the toroidal field parameter is specified appropriately for low aspect ratio (see related discussions in [270]). Low-k turbulence is largely suppressed by flow shear, apart from in the outer quarter of the simulated region, and collisions play a significant role in suppressing the drive from trapped electrons. Outside $q = 1$, electron heat transport is dominated by high-k ETG, but transport contributions from low-k turbulence double χ_e over the outer quarter in radius: the modeled electron transport is slightly too low. In $q < 1$ regions in the MAST discharges, and at $\rho < 0.4$ and $q > 1$ in NSTX, the

measured electron transport is much larger than predicted by TGLF, indicating that another mechanism (like MHD or fast particle driven instabilities) must be impacting the apparent electron energy transport [176, 197].

The GLF23 transport model [285] is a simpler predecessor to TGLF, and includes Shafranov shift effects and flow shear stabilization. GLF23 was also used to model a small number of sawtooth-free MAST L-modes [197], and provided remarkably good predictions for the profile evolution of T_i and T_e for $r/a > 0.4$ as long as the flow shear suppression was included. Like TGLF, however, GLF23 also under-predicted the level of transport in the core.

An updated TGLF model [286] using both the 'SAT0' and 'SAT1' saturation models was tested against an NSTX-L-mode discharge [287]. It was found that the SAT1 model, which accounts for cross-scale coupling, gave much better agreement between the predicted T_e profile and the measured one. Neither the SAT0 or SAT1 models have been successful in predicting T_e from NSTX H-mode discharges. More recent updates to the saturation model in TGLF have been made, and they require dedicated validation.

9. Summary and future work

In this review we have presented results, which show that many fundamental energy transport and confinement properties of STs are different from those at higher aspect ratio. The origin of these differences is based on equilibrium geometry; relative to conventional aspect ratio plasmas, ST plasmas have more extreme toroidicity (i.e. reduced region of bad curvature) as well as relatively larger $E_r \times B$ shearing rates, both of which serve to suppress electrostatic drift wave instabilities. In addition, operating at high β makes the ST more prone to electromagnetic instabilities with both MTMs and KBMs becoming important in the core of ST plasmas, while mattering only at extremely high performance or in the pedestal region at higher aspect ratio. Data from STs have revealed a stronger dependence of energy confinement time on B_T and a weaker dependence on I_p than is observed at higher aspect ratio, although these dependences, even in a single ST device, are influenced by wall recycling through different wall conditioning techniques. Related to these B_T and I_p dependences, the ST data have also revealed a very strong improvement in normalized confinement with decreasing collisionality, $\Omega\tau_E \propto \nu_{e,*}^{-1}$, which is much stronger than at higher aspect ratio. Further, ST confinement scalings inferred from dimensionality constraints, as well as from a limited database spanning a range of major radius, indicate a strong scaling of confinement on plasma size, with $\tau_E \propto R^{2.1-2.7}$. These trends require further confirmation, but the confinement scalings with both size and collisionality bode well for an ST-based FPP.

In the present generation of STs, heat transport is predominantly through the electron channel, which is highly anomalous. Ion transport outside the very core of the plasma, and especially in H-modes, is near neoclassical values (reflecting the suppression of the low-k electrostatic drift wave instabilities), although neoclassical ion thermal diffusivities can be in

the ≥ 1 m^2 s^{-1} range. There is some inferred evidence that ion transport becomes more anomalous at the lowest ST collisionalities attained to date. Studies of particle and momentum transport have been more limited, but the latter may indeed be impacted by any subdominant low-k drift wave turbulence. ITBs have been observed in both MAST and NSTX, and, as at higher aspect ratio, their existence and properties are sensitive to local values of q and $\hat{s}$.

GK studies in the present generation of STs, coupled with low- and high-k turbulence measurements, have shed light on the underlying physics controlling transport in the plasma core, but outside the central region of the plasma; in the central core energetic particle driven modes may lead to high electron transport and/or modifications of the neutral beam heating deposition profile. Outside the central core at lower β, both ion- and electron-scale electrostatic drift turbulence may be responsible for transport, while at higher β, MTMs, KBMs, and hybrid TEM/KBMs increasingly play a role. All of these modes are sensitive to $\hat{s}$, q and R/L_n. Flow shear affects the balance between ion- and electron-scale modes. Considerable work has been devoted to understanding electron heat transport from MTMs, which are complex modes with instability thresholds in R/L_{Te} and β, and growth rate sensitivity (some non-monotonic) to collisions, $\hat{s}$, R/L_n and q.

Non-linear GK simulations have identified ST regimes dominated by MTMs and ETGs, where the electron heat flux falls with decreasing collisionality, consistent with the normalized energy confinement scaling, although flow shear was neglected in these calculations. High-β plasmas with large α_{MHD} (where high-n ballooning instability might be expected), exhibit significant transport in all channels; the growth rates for hybrid TEM/KBM modes can be dominant in this regime. Non-linear ETG simulations predict significant heat fluxes in some high- and low-β H-modes. We note, however, that in some plasmas where ETG and MTMs are both unstable, initial multi-scale non-linear simulations [288] find that ETG suppresses MTMs.

A wealth of fluctuation data from BES, DBS, and high-k scattering has facilitated detailed comparisons with GK simulations and the study of fluctuations at ion and electron scales in MAST and NSTX. These data have provided compelling evidence for the presence of ITG and ETG turbulence in some plasmas, and direct experimental support for the impact of experimental actuators like γ_E, R/L_n and $\hat{s}$ on turbulence and transport.

An ST FPP or reactor certainly requires an extrapolation in parameters from present experiments, and its success can only really be demonstrated by its construction and operation. We can base extrapolations on the encouraging trends from experiments to date, but to build confidence these trends must continue to be tested against data from future experiments that extend into more relevant regions of parameter space. The reliability of the extrapolations should also be tested against predictions from first-principles based GK simulations of turbulence and transport. One of the most critical issues for the next generation of ST experiments is to determine whether the strong improvement of normalized confinement with decreasing collisionality is sustained at the lower collisionalities that

move toward parameter regimes expected in ST burning plasmas, and to identify the modes responsible for the transport in this parameter regime. Understanding the underlying transport mechanisms is crucial since enhanced confinement is a basic requirement for a number of aspects of ST performance and for informing the design of an ST power plant; a continued strong improvement of confinement with decreasing collisionality is key to achieving high $nT\tau_E$ (equation (2)) and high fusion power through access to the MHD beta limit (equation (3)). Further, enhanced confinement is important for attaining the high, stable β_N that is necessary to achieve a high bootstrap current fraction.

GK simulations based on existing devices indicate that transport from MTMs, ETGs, and DTEMs should decrease at lower collisionality, and that longer wavelength KBMs and TEM/KBMs may become more significant for transport. Nevertheless, local GK studies for conceptual ST reactors indicate that MTMs and KBMs are likely to be dominant. The MTMs are predicted to dominate over an extended range of binormal scales, and they may cause more transport losses than KBMs during a high performance phase. Performing high fidelity first-principles simulations to estimate the transport from such modes is a key challenge that must be addressed.

NSTX-U with up to 18 MW of auxiliary heating power (see table 1), B_T up to 1 T and I_p up to 2 MA will be able to explore a collisionality regime up to five times lower than that in NSTX, thus testing the confinement and transport processes of both the thermal plasma and energetic particles in this more reactor relevant regime. NSTX-U, with its ability to achieve very high β_N/l_i will also explore the high-β route to non-inductive, long-pulse operation, with high τ_E being necessary for accessing this regime. Further, while NSTX-U will explore heat flux mitigation in conventional divertor configurations, future upgrades to NSTX-U could involve the implementation of liquid lithium divertors. MAST-U operation in a parameter range similar to that of NSTX-U will also explore the confinement and transport at lower collisionalities than achieved in MAST, but its main focus will be to exploit its flexibility to test a wide range of divertor configurations, the most notable being the long-legged Super-X divertor approach to mitigating divertor target power loads. Establishing reduced plasma-material interaction methodologies is critical for maintaining core plasma purity and developing optimized core-edge scenarios that can lead to sustained high performance. ST40 will be operating at higher toroidal field (3 T) than either NSTX-U or MAST-U to achieve fusion relevant ion temperatures [289] and to develop the physics basis for using high temperature superconducting magnets to target the delivery of scientific break-even with fusion powers of $Q \geq 2$. Globus-M2 plasmas will continue to operate at high B_T, and data from this ST, along with data from NSTX-U, MAST-U and ST40 will form the basis for establishing/confirming the size scaling for ST confinement.

These new experiments will open up avenues for continued and extended physics studies of ST confinement and transport, which will help resolve a number of outstanding issues important for developing a broad physics basis for an ST power plant. The importance of establishing the size scaling

of confinement was already mentioned. Scaling studies have identified strong correlations among dimensionless variables. Expanded parameter regimes will allow for more understanding of the trends of confinement; most notably, higher B_T will help resolve uncertainties with the ρ_* scaling as well as the correlation between the β and q scalings. Expanded diagnostic sets, most notably in their ability to measure poloidal velocity shear, δn, δT, and δB turbulence, and comparison to GK simulations enhanced with the inclusion of synthetic diagnostics, will give a better experimental underpinning of the modes driving transport.

ST power plants may be RF heated, and further intrinsic rotation measurements and modeling will aid in projections of possible microturbulence and MHD mode suppression in these devices. Some GK simulations have identified 'sweet spots' in collisionality for reduced transport, and this theory result can be tested in the reduced collisionality accessible in the newer devices. Particle transport studies and model development are necessary for understanding whether peaked density profiles generating high core fusion power in STs can be achieved, and studies of impurity transport will help to understand potential dilution by helium ash and radiation losses. Also important is the effect of energetic particle-driven modes on the energetic particle distribution, which can affect both non-inductive current drive and fusion power production. Further, the new experiments will drive progress on understanding and optimizing core-pedestal interactions to allow access to stable high performance scenarios. These can be accomplished through both the flexibility of the devices as well as diagnostics and theory specifically targeting these phenomena.

The impact of fast particles on thermal confinement in the plasma core remains an open question. This relates to the nature of interactions between turbulent transport processes associated with the thermal plasma and fusion α-particles, which will be critical for all burning plasma devices. Data from NSTX-U and MAST-U will help to resolve the puzzle as to whether (and if so, how) electron heat confinement is degraded in strongly heated high β ST plasmas with fast particle driven GAE and CAEs, and to explore how available actuators may be exploited to optimize performance.

The expanded operating ranges of these STs will extend the space that is available for validation of theoretical predictions to complement the empirical experimental approach. This will include comparing GK simulations coupled to synthetic diagnostics with experimental measurements of turbulence and kinetic profiles. Advances in computer science will boost the fidelity of turbulence modeling that can be achieved through more comprehensive GK simulations, which will be critical for advancing our understanding of ST transport. One such area is the need for advanced multi-scale simulations that can model the interactions between electromagnetic turbulence arising at electron and ion scales. Another important area for exploration is that of the non-linear relation between turbulence and zonal flows, the latter providing a non-linear saturation mechanism. Also, because of the relatively larger scale sizes at low aspect ratio due to lower B_T, global rather than local simulations may lead to more accurate pictures of the plasma microturbulence. Advances in computer science

will allow for more accurate and self-consistent treatments of flow shear, the importance of thermal plasma transport caused by energetic particle-driven modes, and the ability to provide global descriptions including phenomena like avalanching and turbulence spreading.

These first-principles studies will contribute to the development of higher quality reduced models with broader range of validity, which are urgently needed for predictive calculations to describe uncharted plasma regimes. To date, only mostly semi-heuristic, reduced models have been used, and with success only in limited parameter ranges. More sophisticated physics-based reduced models will be developed by exploiting advances in computer science to base the models on higher fidelity GK simulations (e.g. multi-scale and/or global), to help build confidence in projections of to ST burning plasma regimes.

Research to date has revealed much about transport and confinement in STs, and it indicates that STs have considerable potential. However, many questions must be addressed more fully to build confidence in the capacity of STs to deliver fusion energy. Considerable progress can be expected over the next few years with data from expanded diagnostics in new machines such as NSTX-U, MAST-U, Globus-M2, ST40, and advances in simulations and computing. This will be critical for assessing the feasibility of an ST-based fusion reactor.

Data availability statement

No new data were created or analysed in this study.

Acknowledgments

ORCID iDs

S M Kaye ⓘ https://orcid.org/0000-0002-2514-1163
J W Connor ⓘ https://orcid.org/0000-0001-9666-6103
C M Roach ⓘ https://orcid.org/0000-0001-5856-0287

References

[1] Peng Y-K M and Strickler D J 1986 *Nucl. Fusion* **26** 769
[2] Peng Y-K M 2000 *Phys. Plasmas* **7** 1681
[3] Voss G M *et al* 2008 *Fusion Eng. Des.* **83** 1648
[4] Abdou M A *et al* 1996 *Fusion Technol.* **29** 1
[5] Peng Y-K M *et al* 2005 *Plasma Phys. Control. Fusion* **47** B263
[6] Peng Y-K M *et al* 2009 *Fusion Sci. Technol.* **56** 957
[7] Wilson H R *et al* 2004 *Nucl. Fusion* **44** 917
[8] Menard J E *et al* 2011 *Nucl. Fusion* **51** 103014
[9] Costley A E, Hugill J and Buxton P 2015 *Nucl. Fusion* **55** 033001

[10] Menard J E *et al* 2016 *Nucl. Fusion* **56** 106023
[11] Sykes A *et al* 2018 *Nucl. Fusion* **58** 016039
[12] Menard J E 2019 *Phil. Trans. R. Soc.* A **377** 20170440
[13] Costley A E 2019 *Phil. Trans. R. Soc.* A **377** 20170439
[14] Wilson H R, Chapman I and Denton T (the STEP Team) 2020 Step: along the pathway to fusion commercialization *Commercialising Fusion Energy* (Bristol: IOP Publishing) pp 8–1–18
[15] Costley A E and McNamara S A M 2021 *Plasma Phys. Control. Fusion* **63** 035005
[16] Kaye S M *et al* 1999 *Fusion Technol.* **36** 16
[17] Ono M *et al* 2001 *Nucl. Fusion* **41** 1435
[18] Darke A C *et al* 1995 *Fusion Technol.* **1** 799
[19] Sykes A 1994 *Plasma Phys. Control. Fusion* **36** B93
[20] Menard J E *et al* 1997 *Nucl. Fusion* **37** 595
[21] Roberto M and Galvao R M O 1992 *Nucl. Fusion* **32** 1666
[22] Sabbagh S A *et al* 2004 *Nucl. Fusion* **46** 635
[23] Bickerton R J, Connor J W and Taylor J B 1971 *Nat. Phys. Sci.* **229** 110
[24] Galeev A A 1971 *Sov. Phys. JETP* **32** 752
[25] Gerhardt S P *et al* 2011 *Nucl. Fusion* **51** 073031
[26] Sabbagh S A *et al* 2013 *Nucl. Fusion* **53** 104007
[27] Greenwald M 2002 *Plasma Phys. Control. Fusion* **44** R27
[28] ITER Physics Basis Expert Group on Confinement and Transport 1999 *Nucl. Fusion* **39** 2175
[29] Sykes A, Turner M F and Patel S 1983 β-limits in tokamaks due to high-n ballooning modes *Proc. 11th Eur. Conf. Controlled Fusion and Plasma Physics (Aachen)* (*Petit-Lancy, Switzerland*) vol 2 (European Physical Society) p 363
[30] Troyon F *et al* 1984 *Plasma Phys. Control. Fusion* **26** 209
[31] Rewoldt G *et al* 1996 *Phys. Plasmas* **3** 1667
[32] Kotschenreuther M *et al* 2000 *Nucl. Fusion* **40** 677
[33] Gorelenkov N N *et al* 2004 *Phys. Plasmas* **11** 2586
[34] Takase H 2001 *J. Phys. Soc. Japan* **70** 609
[35] Kotschenreuther M *et al* 2007 *Phys. Plasmas* **14** 072502
[36] Ryutov D 2007 *Phys. Plasmas* **14** 064502
[37] Jarboe T R 1989 *Fusion Technol.* **15** 7
[38] Jarboe T R *et al* 1998 *Phys. Plasmas* **5** 1807
[39] Bongard M W *et al* 2019 *Nucl. Fusion* **59** 076003
[40] Hanada K *et al* 2008 Physical design of MW-class steady-state spherical tokamak *QUEST, IAEA Fusion Conf. Proc.* p FT/P3-25
[41] Ono Y *et al* 2003 *Nucl. Fusion* **43** 789
[42] Ono Y *et al* 2008 Ion and electron heating characteristics of magnetic reconnection in TS-3 and UTST merging startup experiments *IAEA Fusion Conf. Proc.* p EX/P9-4
[43] Nagata M *et al* 2003 *Phys. Plasmas* **10** 2932
[44] Chung K J *et al* 2013 *Plasma Sci. Technol.* **15** 244
[45] Wang W H *et al* 2005 *Plasma Phys. Control. Fusion* **47** 1
[46] Takase H *et al* 2001 *Nucl. Fusion* **41** 1543
[47] Maekawa T *et al* 2005 *Nucl. Fusion* **45** 1439
[48] Majeski R J *et al* 2006 *Phys. Rev. Lett.* **97** 075002
[49] Majeski R J *et al* 2009 *Nucl. Fusion* **49** 055014
[50] Ono M and Kaita R 2015 *Phys. Plasmas* **22** 040501
[51] Gryzanevich M *et al* 1998 *Phys. Rev. Lett.* **80** 3972
[52] Gartska G D *et al* 2003 *Phys. Plasmas* **10** 1805
[53] Schlossberg D J *et al* 2017 *Phys. Rev. Lett.* **119** 035001
[54] Gusev V K *et al* 2009 *Nucl. Fusion* **49** 104021
[55] Minaev V B *et al* 2018 *IOP Conf. Ser.: J. Phys.* **1094** 012001
[56] Carolan P G *et al* 1998 *Plasma Phys. Control. Fusion* **40** 615
[57] Sykes A *et al* 2000 *Phys. Rev. Lett.* **84** 495
[58] Snipes J A and (the H-mode Threshold Database Group) 1997 An analysis of the H-mode threshold in ITER *Proc. 24th Conf., Berchtesgaden, Part III* p 96
[59] Maingi R *et al* 2002 *Phys. Rev. Lett.* **88** 035003
[60] Maingi R *et al* 2003 *Nucl. Fusion* **43** 969
[61] Kaye S M *et al* 2003 *Phys. Plasmas* **10** 3953
[62] Sykes A *et al* 2001 *Nucl. Fusion* **41** 1423

[63] Counsell G F *et al* 2002 *Plasma Phys. Control. Fusion* **44** B23
[64] Field A R *et al* 2002 *Plasma Phys. Control. Fusion* **44** A113
[65] Thome K *et al* 2016 *Phys. Rev. Lett.* **116** 175001
[66] Thome K *et al* 2017 *Nucl. Fusion* **57** 022018
[67] Menard J E *et al* 2017 *Nucl. Fusion* **57** 102006
[68] Battaglia D J *et al* 2018 *Nucl. Fusion* **58** 046010
[69] Harrison J R *et al* 2021 Overview of first results from MAST-Upgrade *Proc. 28th IAEA Fusion Conf., Virtual* p EX/P6-39
[70] Maingi R *et al* 2004 *Plasma Phys. Control. Fusion* **46** A305
[71] Akers R J *et al* 2002 *Phys. Plasmas* **9** 3919
[72] Field A R *et al* 2004 Core heat transport in the MAST Spherical Tokamak *Proc. 22nd IAEA Fusion Conf., Vilamoura* p EX/2–11
[73] Lloyd B *et al* 2003 *Nucl. Fusion* **43** 1665
[74] Maingi R *et al* 2010 *Nucl. Fusion* **50** 064010
[75] Fundamenski W *et al* 2012 *Nucl. Fusion* **52** 062003
[76] Lloyd B *et al* 2007 *Nucl. Fusion* **47** S658
[77] Andrew Y *et al* 2019 *Plasma* **2** 328
[78] Scannell R *et al* 2015 *Plasma Phys. Control. Fusion* **57** 075013
[79] Kaye S M *et al* 2011 *Nucl. Fusion* **51** 113019
[80] Bush C E *et al* 2003 *Phys. Plasmas* **10** 1755
[81] Takizuka T 2004 for the H-mode Threshold Database Group *Plasma Phys. Control. Fusion* **46** A227
[82] Chang C S, Ku S and Weitzner H 2004 *Phys. Plasmas* **11** 2649
[83] Battaglia D J *et al* 2013 *Nucl. Fusion* **53** 113032
[84] Zweben S *et al* 2010 *Phys. Plasmas* **17** 102502
[85] White A E *et al* 2006 *Phys. Plasmas* **13** 072301
[86] Diallo A *et al* 2017 *Nucl. Fusion* **57** 066050
[87] Zweben S *et al* 2021 *Phys. Plasmas* **28** 032304
[88] Schmitz L 2017 *Nucl. Fusion* **57** 025003
[89] Counsell G F *et al* 2005 *Nucl. Fusion* **45** S157
[90] Rogers B N *et al* 1998 *Phys. Rev. Lett.* **81** 4396
[91] Guzdar P N *et al* 2001 *Phys. Rev. Lett.* **87** 015001
[92] Wilson H R *et al* 1999 *Phys. Plasmas* **6** 1925
[93] Pogutse O *et al* 1997 *Cont. Fusion Plasma Phys.* **21A** 1545
[94] Guzdar P N *et al* 2002 *Phys. Rev. Lett.* **89** 265004
[95] Martin Y R and Takizuka T and the H-mode Threshold Database Group 2008 *J. Phys. Conf. Ser.* **123** 012033
[96] Ryter F (the H-mode Threshold Database Group 2002 *Plasma Phys. Control. Fusion* **44** A415
[97] Draper N R and Smith H 1981 *Applied Regression Analysis* 2nd edn (New York: Wiley)
[98] Anderson T W 1984 *Ann. Stat.* **12** 1
[99] Gelman A 2009 *Bayesian Data Analysis* 2nd edn (Boca Raton, FL: Chapman and Hall)
[100] Allen L and Bishop C 1992 *Plasma Phys. Control. Fusion* **34** 1291
[101] Murari A *et al* 2017 *Nucl. Fusion* **57** 126017
[102] Spears B K *et al* 2018 *Phys. Plasmas* **25** 080901
[103] Kaye S M *et al* 2001 *Phys. Plasmas* **8** 1977
[104] Kurskiev G S *et al* 2017 *Plasma Phys. Control. Fusion* **59** 045010
[105] Sykes A *et al* 1999 *Nucl. Fusion* **39** 1271
[106] Kaye S M *et al* 2006 *Nucl. Fusion* **46** 848
[107] Sykes A *et al* 1997 *Plasma Phys. Control. Fusion* **39** B247
[108] Kaye S M *et al* 2007 *Nucl. Fusion* **47** 499
[109] Valovic M *et al* 2005 *Nucl. Fusion* **45** 942
[110] Valovic M *et al* 2009 *Nucl. Fusion* **49** 075016
[111] Telnova A Y *et al* 2017 *J. Phys. Conf. Ser.* **907** 012014
[112] Kurskiev G S *et al* 2019 *Nucl. Fusion* **59** 066032
[113] Bakharov N N *et al* 2018 *Nucl. Fusion* **58** 126029
[114] Kurskiev G S *et al* 2021 *Nucl. Fusion* **61** 064001
[115] Maingi R *et al* 2009 *Phys. Rev. Lett.* **103** 075001
[116] Maingi R *et al* 2010 *Phys. Rev. Lett.* **105** 135004
[117] Gerhardt S P *et al* 2014 *Nucl. Fusion* **54** 083021

[118] Battaglia D J *et al* 2020 *Phys. Plasmas* **27** 072511
[119] Maingi R *et al* 2012 *Nucl. Fusion* **52** 083001
[120] Kaye S M *et al* 2013 *Nucl. Fusion* **53** 063005
[121] Buxton P *et al* 2019 *Plasma Phys. Control. Fusion* **61** 035006
[122] Kurskiev G S *et al* 2021 Energy confinement in the spherical tokamak Globus-M2 with a toroidal magnetic field reaching 0.8 T *Nucl. Fusion* accepted (https://doi.org/10.1088/1741-4326/ac38c9)
[123] Kaye S M *et al* 2006 *Plasma Phys. Control. Fusion* **48** A429
[124] Stutman D *et al* 2009 *Phys. Rev. Lett.* **102** 115002
[125] Connor J W and Taylor J B 1977 *Nucl. Fusion* **17** 1047
[126] Connor J W 1988 *Plasma Phys. Control. Fusion* **30** 619
[127] Kadomtsev B B 1975 *Sov. Phys. - J. Plasmas Phys.* **1** 295
[128] Petty C C 2008 *Phys. Plasmas* **15** 080501
[129] Luce T 2008 *Plasma Phys. Control. Fusion* **50** 043001
[130] Valovic M *et al* 2011 *Nucl. Fusion* **51** 073045
[131] Kaye S M *et al* 2007 *Phys. Rev. Lett.* **98** 175002
[132] Petrov Yu V *et al* 2021 *Nucl. Fusion* accepted (https://doi.org/10.1088/1741-4326/ac27c7)
[133] Bell R E 2006 *Rev. Sci. Inst.* **77** 10E902
[134] Menard J E *et al* 2003 *Nucl. Fusion* **43** 330
[135] Chapman I T *et al* 2007 *Plasma Phys. Control. Fusion* **49** B385
[136] Berkery J W *et al* 2017 *Phys. Plasmas* **24** 056103
[137] Solomon W *et al* 2008 *Phys. Rev. Lett.* **101** 065004
[138] Kaye S M *et al* 2009 *Nucl. Fusion* **49** 045010
[139] Meyer H *et al* 2009 *Nucl. Fusion* **49** 104017
[140] Guttenfelder W *et al* 2017 *Nucl. Fusion* **57** 056022
[141] Hawryluk R J *et al* 1980 An empirical approach to tokamak transport *Physics of Plasmas Close to Thermonuclear Conditions* vol 1, ed B Coppi (Brussels: CEC) p 19
[142] Peeters A G, Angioni C and Strinzi D 2007 *Phys. Rev. Lett.* **98** 265003
[143] Hahm T S *et al* 2007 *Phys. Plasmas* **14** 072302
[144] Park J-K *et al* 2013 *Nucl. Fusion* **53** 063012
[145] Hilleshein W H *et al* 2015 *Nucl. Fusion* **55** 032003
[146] Barnes M *et al* 2013 *Phys. Rev. Lett.* **111** 055005
[147] Parra F and Barnes M 2015 *Plasma Phys. Control. Fusion* **57** 045002
[148] Wang W X *et al* 2006 *Phys. Plasmas* **13** 092505
[149] Schneider R 2006 *Contrib. Plasma Physics* **46** 3
[150] Henderson S S *et al* 2014 *Nucl. Fusion* **54** 093013
[151] Henderson S S *et al* 2015 *Plasma Phys. Control. Fusion* **57** 095001
[152] Belli E A and Candy J 2008 *Plasma Phys. Control. Fusion* **50** 095010
[153] Belli E A and Candy J 2012 *Plasma Phys. Control. Fusion* **54** 015015
[154] Stutman D *et al* 2003 *Phys. Plasmas* **10** 4387
[155] Leblanc B P *et al* 2004 *Nucl. Fusion* **44** 513
[156] Scotti F *et al* 2013 *Nucl. Fusion* **53** 083001
[157] Scotti F *et al* 2015 *J. Nucl. Mater.* **463** 1165
[158] Scotti F *et al* 2017 *Nucl. Mater. Energy* **12** 768
[159] Rognlien T D *et al* 1992 *J. Nucl. Mat.* **196–198** 347
[160] Scotti F 2014 Modifications of impurity transport and divertor sources by lithium wall conditioning in the national spherical torus experiment *PhD Thesis* Princeton University
[161] Houlberg W 1997 *Phys. Plasmas* **4** 3320
[162] Hulse R 1983 *Nucl. Technol. Fusion* **3** 259
[163] Akers R J *et al* 2003 *Plasma Phys. Control. Fusion* **45** A175
[164] Meyer H *et al* 2004 *Plasma Phys. Control. Fusion* **46** A291
[165] Field A R *et al* 2011 *Nucl. Fusion* **51** 063006
[166] Lloyd B *et al* 2011 *Nucl. Fusion* **51** 094013
[167] Yuh H *et al* 2009 *Phys. Plasmas* **16** 056120
[168] Yuh H Y *et al* 2011 *Phys. Rev. Lett.* **106** 055003
[169] Kotschenreuther M, Rewoldt G and Tang W M 1995 *Comput. Phys. Commun.* **88** 128
[170] Candy J and Waltz R E 2003 *J. Comput. Phys.* **186** 545

[171] Peeters A G and Strintzi D 2004 *Phys. Plasmas* **11** 3748
[172] Jolliet S *et al* 2007 *Comput. Phys. Commun.* **177** 409
[173] Bottino A *et al* 2007 *Phys. Plasmas* **14** 010701
[174] Roach C M, Connor J W and Janjua S 1995 *Plasma Phys. Control. Fusion* **37** 679
[175] Bourdelle C 2003 *Phys. Plasmas* **10** 2881
[176] Staebler G M *et al* 2008 Testing the trapped gyro-Landau fluid transport model with data from tokamaks and spherical tori *Proc. 22nd IAEA Fusion Conf. (Geneva, Switzerland)* p TH/P8-42
[177] Roach C M *et al* 2005 *Plasma Phys. Control. Fusion* **47** B323
[178] Redi M H *et al* 2005 Testing gyrokinetics on C-Mod and NSTX *Proc. 32nd Conf. on Plasma Physics, Tarragona, Spain, ECA* vol 29C p -5.041
[179] Redi M H *et al* 2003 Gyrokinetic calculations of microturbulence and transport for NSTX and Alcator-CMOD H-modes *Proc. 30th Conf. on Plasma Physics (St. Petersburg, Russia)* vol ECA 27A p -4.94
[180] Applegate D J *et al* 2004 *Phys. Plasmas* **11** 5085
[181] Belova E V *et al* 2015 *Phys. Rev. Lett.* **115** 015001
[182] Roach C M *et al* 2001 *Nucl. Fusion* **41** 11
[183] Telnova A *et al* 2020 *Plasma Phys. Control. Fusion* **62** 045011
[184] Guttenfelder W *et al* 2019 *Nucl. Fusion* **59** 056027
[185] Ren Y *et al* 2017 *Nucl. Fusion* **57** 072002
[186] Guttenfelder W *et al* 2013 *Nucl. Fusion* **53** 093022
[187] Garzotti L *et al* 2014 *Plasma Phys. Control. Fusion* **56** 035004
[188] Connor J W *et al* 2006 Turbulent transport in spherical tokamaks with transport barriers (poster) *Proc. 21st IAEA Fusion Conf. (Chengdu, China)* p TH/P2-2
[189] Coppi B and Pegoraro F 1977 *Nucl. Fusion* **17** 969
[190] Belli E A and Candy J 2010 *Phys. Plasmas* **17** 112314
[191] Peeters A G *et al* 2005 *Phys. Plasmas* **12** 022505
[192] Jenko F, Dorland W and Hammett G W 2001 *Phys. Plasmas* **8** 4096
[193] Wang W X *et al* 2015 *Phys. Plasmas* **22** 102509
[194] Ren Y *et al* 2019 *Nucl. Fusion* **60** 026005
[195] Wang W X *et al* 2015 *Nucl. Fusion* **55** 122001
[196] Menard J E *et al* 2012 *Nucl. Fusion* **52** 083015
[197] Akers R J *et al* 2008 Transport studies in the MAST spherical tokamak *Proc. 22nd IAEA Fusion Conf. (Geneva, Switzerland)* p EX/2-2
[198] Roach C M *et al* 2009 *Plasma Phys. Control. Fusion* **51** 124020
[199] Catto P J, Rosenbluth M N and Liu C S 1973 *Phys. Fluids* **16** 1719
[200] Ghim Y-C *et al* 042003 *Nucl. Fusion* **54** 2014
[201] Schekochihin A A, Highcock E G and Cowley S C 2012 *Plasma Phys. Control. Fusion* **54** 055011
[202] Highcock E G *et al* 2010 *Phys. Rev. Lett.* **105** 215003
[203] Highcock E G *et al* 2012 *Phys. Rev. Lett.* **109** 265001
[204] Saarelma S *et al* 2012 *Plasma Phys. Control. Fusion* **54** 085012
[205] Field A R *et al* 2014 *Plasma Phys. Control. Fusion* **56** 025012
[206] Fox M F *et al* 2017 *Plasma Phys. Control. Fusion* **59** 034002
[207] van Wyk F *et al* 2017 *Plasma Phys. Control. Fusion* **59** 114003
[208] van Wyk F *et al* 2016 *J. Plasma Phys.* **82** 905820609
[209] Fox M F *et al* 2017 *Plasma Phys. Control. Fusion* **59** 044008
[210] Field A R *et al* 2014 Influence of flow shear on the structure of ion-scale turbulence in MAST *Proc. 25th IAEA Fusion Conf. (St Petersburg, Russia)* p EX/P4-38
[211] Ghim Y-C *et al* 2013 *Phys. Rev. Lett.* **110** 145002
[212] Lin Z *et al* 1999 *Phys. Rev. Lett.* **83** 3645
[213] Kiselev E O *et al* 2019 *J. Phys.: Conf. Ser.* **1383** 012003
[214] Jian X *et al* 2021 *Phys. Plasmas* **28** 042501
[215] Hatch D R *et al* 2021 *Nucl. Fusion* **61** 036015

[216] Patel B S *et al* 2021 Linear gyrokinetic stability of a high β non-inductive spherical tokamak *Nucl. Fusion* accepted (https://doi.org/10.1088/1741-4326/ac359c)
[217] Applegate D J *et al* 2007 *Plasma Phys. Control. Fusion* **49** 1113
[218] Guttenfelder W *et al* 2012 *Phys. Plasmas* **19** 022506
[219] Guttenfelder W *et al* 2012 *Phys. Plasmas* **19** 056119
[220] Applegate D J 2007 Gyrokinetic studies of a spherical tokamak H-mode plasma *PhD Thesis* Imperial College London
[221] Drake J F and Lee Y C 1977 *Phys. Fluids* **20** 1341
[222] Gladd N T *et al* 1980 *Phys. Fluids* **23** 1182
[223] D'Ippolito D A, Lee Y C and Drake J F 1980 *Phys. Fluids* **23** 771
[224] Catto P J and Rosenbluth M N 1981 *Phys. Fluids* **24** 243
[225] Hazeltine R D, Dobrott D and Wang T S 1975 *Phys. Fluids* **18** 1778
[226] Dickinson D *et al* 2012 *Phys. Rev. Lett.* **108** 135002
[227] Dickinson D *et al* 2013 *Plasma Phys. Control. Fusion* **55** 074006
[228] Canik J M *et al* 2013 *Nucl. Fusion* **53** 113016
[229] Predebon I and Sattin F 2013 *Phys. Plasmas* **20** 040701
[230] Swamy A K *et al* 2014 *Phys Plasmas* **21** 082513
[231] Hamed M *et al* 2019 *Phys. Plasmas* **26** 092506
[232] Smith D R *et al* 2011 *Plasma Phys. Control. Fusion* **53** 035013
[233] Wong K L *et al* 2007 *Phys. Rev. Lett.* **99** 135003
[234] Drake J F *et al* 1980 *Phys. Rev. Lett.* **44** 994
[235] Rechester A B and Rosenbluth M N 1978 *Phys. Rev. Lett.* **40** 38
[236] Guttenfelder W *et al* 2011 *Phys. Rev. Lett.* **106** 155004
[237] Dorland W *et al* 2000 *Phys. Rev. Lett.* **85** 5579
[238] Jenko F and Dorland W 2002 *Phys. Rev. Lett.* **89** 225001
[239] Reshko M and Roach C M (the MAST Team) 2008 *Plasma Phys. Control. Fusion* **50** 115002
[240] Joiner N and Hirose A 2007 *Phys. Plasmas* **14** 112111
[241] Joiner N, Hirose A and Dorland W 2010 *Phys. Plasmas* **17** 072104
[242] Berk H L and Dominguez R R 1977 *J. Plasma Phys.* **18** 31
[243] Ren Y *et al* 2012 *Phys. Plasmas* **19** 056125
[244] Colyer G J *et al* 2017 *Plasma Phys. Control. Fusion* **59** 055002
[245] Horton W *et al* 2004 *Phys. Plasmas* **11** 2600
[246] Joiner N *et al* 2006 *Plasma Phys. Control. Fusion* **48** 685
[247] Joiner N J 2005 Microinstabilities in spherical tokamaks *PhD Thesis* Imperial College London
[248] Guttenfelder W and Candy J 2011 *Phys. Plasmas* **18** 022506
[249] Ren Y *et al* 2015 *Phys. Plasmas* **22** 110701
[250] Parisi J F *et al* 2020 *Nucl. Fusion* **60** 126045
[251] Mazzucato E *et al* 2008 *Phys. Rev. Lett.* **101** 075001
[252] Mazzucato E *et al* 2009 *Nucl. Fusion* **49** 055001
[253] Smith D R *et al* 2009 *Phys. Rev. Lett.* **102** 225005
[254] Ren Y *et al* 2011 *Phys. Rev. Lett.* **106** 165005
[255] Ruiz Ruiz J *et al* 2015 *Phys. Plasmas* **22** 122501
[256] Hillesheim J C *et al* 2015 *Nucl. Fusion* **55** 073024
[257] Barnes M, Parra F I and Schekochihin A A 2011 *Phys. Rev. Lett.* **107** 115003
[258] Ruiz Ruiz J *et al* 2019 *Plasma Phys. Control. Fusion* **61** 115015
[259] Dickinson D *et al* 2011 *Plasma Phys. Control. Fusion* **53** 115010
[260] Coury M *et al* 2016 *Phys. Plasmas* **23** 062520
[261] Roach C M *et al* 2012 Gyrokinetic instabilities near an evolving tokamak h-mode pedestal *Proc. 24th IAEA Fusion Conf. (San Diego, USA)* p TH/5-1
[262] Frassinetti L *et al* 2019 *Nucl. Fusion* **59** 076038
[263] Guttenfelder W *et al* 2021 *Nucl. Fusion* **61** 056005
[264] Gorelenkov N N *et al* 2010 *Nucl. Fusion* **50** 084012
[265] Kolesnichenko Y I, Yakovenko Y and Lutsenko V V 2010 *Phys. Rev. Lett.* **104** 075001
[266] Belova E V *et al* 2017 *Phys. Plasmas* **24** 042505
[267] Crocker N A *et al* 2017 *Nucl. Fusion* **58** 016051
[268] Fredrickson E D *et al* 2018 *Nucl. Fusion* **58** 082022
[269] Belova E V *et al* 2019 *Phys. Plasmas* **26** 092507
[270] Roach C M 1996 *Plasma Phys. Control. Fusion* **38** 2187
[271] Chang C S and Hinton F L 1982 *Phys. Fluids* **25** 1493
[272] Chang C S and Hinton F L 1986 *Phys. Fluids* **29** 3314
[273] Rebut P H, Lallia P P and Watkins M L 1988 The critical temperature gradient model of plasma transport: applications to JET and future tokamaks *Proc. 12th IAEA Fusion Conf., Nice* vol 2 p 191
[274] Lackner K and Gottardi N O 1990 *Nucl. Fusion* **30** 767
[275] Merezhkin V G, Mukhovatov V S and Polevoi A R 1988 *Sov. J. Plasma Phys.* **14** 69
[276] Taroni A *et al* 1994 *Plasma Phys. Control. Fusion* **36** 1629
[277] Dnestrovskii Y *et al* 2007 *Plasma Phys. Control. Fusion* **49** 1477
[278] Dnestrovskii Y *et al* 2010 *Plasma Phys. Reports* **36** 645
[279] Dnestrovskii Y *et al* 2011 *Plasma Phys. Control. Fusion* **53** 085025
[280] Wong K L *et al* 2008 *Phys. Plasmas* **15** 056108
[281] Kaye S M *et al* 2014 *Phys. Plasmas* **21** 082510
[282] Rafiq T *et al* 2021 *Phys. Plasmas* **28** 022504
[283] Staebler G M, Kinsey J E and Waltz R E 2007 *Phys. Plasmas* **14** 055909
[284] Roach C M *et al* 2008 *Nucl. Fusion* **28** 125001
[285] Waltz R E *et al* 1997 *Phys. Plasmas* **4** 2482
[286] Staebler G M *et al* 2016 *Phys. Plasmas* **23** 062518
[287] Kaye S M *et al* 2019 *Nucl. Fusion* **59** 112007
[288] Maeyama S, Watanabe T-H and Ishizawa A 2017 *Phys. Rev. Lett.* **119** 195002
[289] Dnestrovskii A 2019 *Plasma Phys. Control. Fusion* **61** 055009